Monte Carlo Studies of the Symmetries of the Spatial Microstructure of Quantum Rare Gas Crystals

A thesis submitted to The University of Manchester for the degree of

Doctor of Philosophy

in the Faculty of Engineering and Physical Sciences

2007

Matthew J Harrison

School of Physics and Astronomy

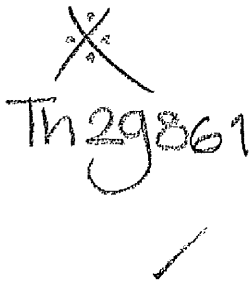

Contents

List of Tables

List of Figures

Abstract

We have undertaken a complete theoretical analysis of the symmetries in the local one- and two-body densities of Face-Centred Cubic (FCC) crystals. Using both Fourier Path Integral Monte Carlo (FPIMC) and Classical Monte Carlo simulations we have performed a through numerical investigation of the symmetries in the one- and two-body densities. Simulations have been undertaken for a range of rare gas solids. The results of these simulations are found to be in exact agreement with the formal theoretical calculations.

Calculations of the quantum kinetic energy of rare gas elements have been performed using FPIMC techniques. By taking the semiclassical limit of the quantum kinetic energy we have derived a quantum correction to the classical Boltzmann kinetic energy to be used in classical Monte Carlo simulations. Comparisons of the kinetic energy calculated using the two approaches have been performed for a range of rare gases at differing thermodynamic states.

Declaration

No portion of the work referred to in the thesis has been submitted in support of an application for another degree or qualification of this or any other university or other institute of learning.

Copyright Statement

Acknowledgement

Thanks are due to my supervisor, Dr. Klaus Gernoth, for his guidance and encouragement. I am also grateful for the contributions of all those with whom I have had discussions over the years, most notably Prof. Niels Walet who has been of great help with many of the computational aspects of this thesis.

My studies would not have been possible without the PhD studentship I received from the Engineering and Physical Sciences Research Council (EPSRC) of Great Britain.

Finally but by no means least, I would like to thank my family for all their love and support.

This thesis is dedicated to my wife, Jenny, without whose support this thesis would not have been possible.

The Author

The author studied Physics with Theoretical Physics at the University of Manchester Institute of Science and Technology (UMIST) graduating in 2004 with a MPhys (Hons) degree. He commenced his PhD studies with Dr. Klaus Gernoth in September of the same year.

The author has attended two international conferences on recent progress in many body physics (RPMBT13 and RPMBT14) where he has presented posters of work undertaken for this thesis. The contents of both posters formed the basis of articles included in the conference proceedings.

Chapter 1

Introduction

Since the discovery of the rare gas solids in the late nineteenth and early twentieth centuries [23] they have been the focus of continued experimental and theoretical analysis. This interest in the rare gas solids is fuelled in part because the differing rare gas elements are all chemically identical [32]. Despite the volume of work produced [11, 19, 30, 35] rare gas solids remain an area of active interest especially where more extreme physical conditions exist [13, 14, 21, 25].

As with many areas of physics there is a close interplay between experimental observations and computational simulations. Experimental studies of rare gas solids have traditionally been concerned with the phase diagram and the Equation of State. The energetic closeness of differing crystalline phases of high-pressure ^{4}He has driven the need for accurate experimental and theoretical tools with which to analyse these systems. The experimental work of Mao *et. al.* [27] uses

single-crystal X-ray diffraction techniques to determine the crystal structure of a sample. There are a number of experimental challenges to performing accurate diffraction experiments. A highly pure sample is required to avoid the possible stabilisation of meta-stable states by impurities [27]. Additionally, because of the physical constraints of the setup it is not possible to probe all orientations of the crystal.

The paper of Mao *et al.* [27] shows that ^{4}He exists as a Hexagonal Close-Packed (HCP) crystal at high-pressures in contrast to the predicted Body-Centred Cubic or Face-Centred Cubic crystals. Theoretical calculations are now in full agreement with these experimental findings [20, 18]. The work of Herrero [20] is particularly important as it shows the importance of the choice of potential chosen for performing Monte Carlo simulations. The simulations performed in these papers are carried out by means of path integral Monte Carlo methods. The approach is based on the path integrals of Feynman and Hibbs [15]. A detailed review of the applications of path integrals to the studies of Helium by Monte Carlo methods is presented by Ceperley [8]. The review by Ceperley highlights the mapping of a quantum system of particles to that of a system of classical ring polymers. In this mapping each quantum particle is mapped to a ring polymer. The polymers are made up of particles at different imaginary times. Interactions between these ring polymers only occur for particles that are at the same imaginary time. Additionally, particles may interact with particles

that form part of the same ring. As Ceperley states the benefits of this mapping are two-fold. Firstly we have a pictorial description of the underlying process, but more importantly we have an approach that leads directly to a computational method for calculating properties of a system of interacting quantum particles.

Much of the work concerning quantum rare gas solids is concerned with Helium. This is due to it being considered the archetypical quantum solid [20]. However, experimental studies of other rare gas solids have been performed [13, 14, 33, 36]. Of particular interest is the work of Timms *et al.* [33] in which the kinetic energies of solid Neon are directly measured. The work of Timms *et al.* used neutrons of higher energy then had previously been used to probe the Neon sample. This led to less uncertainty in the final results. The experimental results were found to be in close agreement with results from path integral Monte Carlo simulations [33] when the HFD-C2 potential was used. Simulations were also performed using the Lennard-Jones potential [33] but were found not to be in as good agreement with the HFD-C2 simulations and experimental data. It was noted that this discrepancy could be due to slow convergence of the Monte Carlo algorithm.

In Section 1.1 we present the motivation for our work. Whilst in Section 1.2 we aim to give a brief historical introduction to the Monte Carlo method that forms the basis of the simulations performed in this work. The rest of this work is split into three chapters. Chapter 2 covers all of the theoretical details of the

work. Results of our simulations are presented in Chapter 3 whilst in Chapter 4 we discuss other areas where our work may be applied.

1.1 Motivation

Much of the motivation for this work stems from wishing to extend the work of Gernoth [16, 17, 18]. The papers of Gernoth set out a formalism by which the space and point group symmetries of a known crystal structure can be utilised to efficiently calculate the one- and two-body densities. Gernoth has performed a rigorous theoretical analysis of the space and point groups of Hexagonal Close-Packed (HCP) structures. The findings of these calculations have been verified by performing Fourier Path Integral Monte Carlo simulations (FPIMC) [16].

Within this work we aim to extend the formal calculations of Gernoth to Face-Centred Cubic structures. Gernoth states that the advantages of employing the space and point group symmetries of a known crystal are two-fold. Firstly one is able to form a set of rules which the respective densities should conform to. Deviations from the expected symmetries of the densities would indicate a transition to another crystal structure type or alternatively another kind of phase transition, for example when a solid melts to form a liquid. Furthermore a symmetrized approach to calculation of the densities using FPIMC and classical Monte Carlo simulations results in largely reduced demands upon the CPU, RAM and hard disk. This allows one to either reduce the run time of a simulation for a fixed

simulation size or increase the simulation size without adversely affecting the run time as compared to simulations using the unsymmetrized density calculations. The one- and two-body densities may be obtained experimentally using x-ray and neutron scattering techniques.

Fourier Path Integral Monte Carlo simulations allow the calculation of a range of microscopic and macroscopic quantities. Of particular interest to us is the kinetic energy per particle for a quantum particle which can be calculated exactly using FPIMC methods. This work is aided by deep inelastic neutron scattering experiments [22] which give experimental values for the kinetic energy per particle with which to compare our results. The work on the kinetic energy is expanded to include a quantum kinetic energy correction for classical Monte Carlo simulations. This correction allows one to calculate the quantum kinetic energy, for a system with limited quantum effects, without the need to perform a full quantum path integral simulation. This has the advantage of greatly reducing the computational demands required to perform a simulation.

1.2 Monte Carlo Simulations

1.2.1 History

The origins of modern Monte Carlo (MC) methods can be traced to the pioneering work of Metropolis, Ulam and von Neumann [1]. The term Monte Carlo arises

from the use of random numbers to perform a calculation and is a reference to the casinos of Monte Carlo. The use of sampling experiments involving random numbers was a technique that had been around for a long time prior to this early work. Allen and Tildesley [1] point out that it was the insight of von Neumann in turning deterministic problems into problems of probability that could be solved by a sampling approach that enabled this powerful technique to be applied to a much greater range of problems.

One of the simplest examples of a Monte Carlo approach is the work of Lazzerini in calculating π according to a theorem set out by Buffon [1]. The theorem states that the probability of a needle crossing a line when it is randomly thrown onto a set of parallel lines is

$$P = \frac{2l}{\pi d}, \tag{1.1}$$

where l is the length of the needle and d is the spacing of the lines with $d > l$ [1]. Lazzerini conducted an experiment [1] where he threw a needle 3407 times. Counting the number of times it crossed the lines gave a value for the probability in Eq. 1.1 and thus an estimate of the value of π.

Allen and Tildesley [1] describe an analogous experiment to calculate π, in which they consider a circle of unit radius enclosed in a square of sides 2 units (cf. Fig. 1.1).

It is possible to calculate π by considering the ratio of the area of the circle to

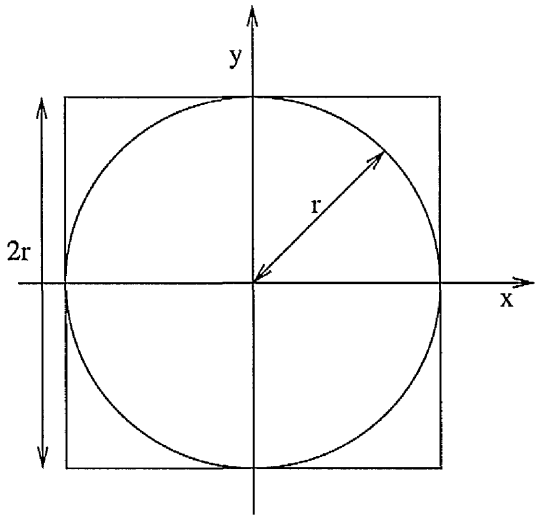

Figure 1.1: Circle enclosed by square.

that of the square

$$\frac{\text{area of circle}}{\text{area of square}} = \frac{\pi r^2}{(2r)^2} = \frac{\pi}{4}. \tag{1.2}$$

Thus if two random numbers x, y representing x and y coordinates are drawn from a uniform distribution between 0 and 1 a test can be performed to see whether the point lies within the circle. The random numbers need only be drawn from 0:1 and not -1:1 as considering the positive quadrant only does not affect the ratio, and it is common for computer-generated random numbers to be in the range 0:1. Repeating this procedure for many independent sets of random numbers, an estimate for π can be calculated via the following relation

$$\pi \approx \frac{4 \times \text{number of sets within circle}}{\text{total number of sets}}. \tag{1.3}$$

The above approach is simple to program as it can be broken into three repeated blocks. Firstly two random numbers are generated. Secondly a test is applied to

those random numbers. Thirdly counters for the number of sets within the circle and the total number of sets are updated. After repeating these steps a number of times a final step is needed to calculate an estimate of π according to Eq. 1.3.

The application of the above approach to enable calculations of the properties of a system of interacting molecules was outlined by Metropolis *et al* [28] and is known as the Metropolis algorithm. A brief outline of the Metropolis algorithm is given below. Complete explanations of the implementations used in this work are given in Sections 2.3-2.6.

1.2.2 Metropolis Algorithm

The Metropolis algorithm considers a finite system of N particles, placed in a square[1]. The system is deemed to be periodic, so that the square of N particles is surrounded on all sides by identical squares of N particles. When calculating distances between two particles i and j, particle i is in the original square and particle j is chosen from any of the squares such that the distance is a minimum. Using this nearest-neighbour approach is valid so long as the potential at large r is small so that any contributions for large r can be neglected.

The potential energy of the system outlined above can be calculated using

$$E_{\text{pot}} = \sum_{i<j}^{N} v(r_{ij}), \tag{1.4}$$

where r_{ij} is the distance as outlined above, and $v(r)$ is a pair potential that

[1]Early work was performed in two dimensions, expansion to three dimensions is trivial

accurately describes the system of interest.

The goal of any Monte Carlo simulation is not to calculate the instantaneous value of a property F of the system but its equilibrium value $\bar{F}$. The equilibrium value in the classical canonical ensemble is given by [28]

$$\bar{F} = \frac{\int F \exp(-E_{\text{pot}}/kT) d\mathbf{R}}{\int \exp(-E_{\text{pot}}/kT) d\mathbf{R}}, \tag{1.5}$$

with k the Boltzmann constant. The integrals are carried out over all of the $3N$-dimensional configurational space. Since the potential is independent of the velocity, there is no need to include additional integration over momentum space.

To calculate the average $\bar{F}$ in Eq. 1.5 by employing the same approach as used for calculating π a configuration would have to be generated at random using $3N$ random numbers. The property of interest F would be calculated for this configuration and weighted with $\exp(-E_{\text{pot}}/kT)$. A subsequent configuration would then be generated from a new set of $3N$ random numbers. Metropolis *et al* note that this would be an ineffective method to adopt as with any closed-packed structure it is likely that the configuration chosen would have very low weight associated with it. This is simpler to visualise in the case of hard spheres where if two spheres overlap the potential will be infinite and the weight zero.

The solution to this low-weight problem was to choose new configurations with probability $\exp(-E_{\text{pot}}/kT)$ and weight them evenly [28]. To achieve this Metropolis *et al* proposed that the particles should be placed initially at fixed lattice points and the potential calculated using Eq. 1.4. A particle i would then

be subjected to a random move of the form

$$\begin{aligned} X_i &\rightarrow X_i + \delta\epsilon_1 \\ Y_i &\rightarrow Y_i + \delta\epsilon_2 \\ Z_i &\rightarrow Z_i + \delta\epsilon_3, \end{aligned} \tag{1.6}$$

where δ is a fixed distance and ϵ_1, ϵ_2 and ϵ_3 are random numbers between -1 and 1. The change in the potential energy ΔE_{pot} of the system as a result of this move is then calculated. If $\Delta E_{\text{pot}} < 0$ then the move is accepted. Otherwise the move is accepted only if $q < \exp(-\Delta E_{\text{pot}}/kT)$ where q is a random number between 0 and 1. The averages are then computed using

$$\bar{F} = \frac{1}{M}\sum_{k=1}^{M} F_k \tag{1.7}$$

where k runs over all accepted moves and F_k is the value of F after a move has been accepted. After an attempt to move a particle the process is repeated for all other particles in turn.

Chapter 2

Theory

In this chapter we aim to present all the relevant theory behind performing both a Fourier Path Integral Monte Carlo (FPIMC) simulation and a classical Monte Carlo simulation. We shall also detail the formal calculations required to compute the local one- and two-body densities. Our calculations take advantage of the symmetries of the space group of the crystal and are herein applied to the face-centred cubic (FCC) crystal structure.

2.1 Hamiltonian and Estimators for FPIMC

In quantum-mechanical calculations it is prudent to begin with the Hamiltonian of the system. For the case of N identical spin-less particles the Hamiltonian can be written as

$$\hat{H} = \hat{T} + \hat{V} = -\frac{\hbar^2}{2m}\sum_{i=1}^{N}\nabla_i^2 + V(\boldsymbol{R}), \tag{2.1}$$

where $\hat{T}$ and $\hat{V}$ are the kinetic and potential energy operators, $\hbar$ is Plank's constant and m is the mass of a particle. The variable $\boldsymbol{R}$ in the potential energy represents the $3N$ co-ordinates of the N particles. The potential energy operator may be written as a sum of all pair, triplet and higher-order interactions up to N-body interactions,

$$\hat{V} = V(\boldsymbol{R}) = \sum_{i<j=1}^{N} v_2(\boldsymbol{r}_i, \boldsymbol{r}_j) + \sum_{i<j<k=1}^{N} v_3(\boldsymbol{r}_i, \boldsymbol{r}_j, \boldsymbol{r}_k) + \cdots v_N(\boldsymbol{r}_1, \boldsymbol{r}_2, \cdots, \boldsymbol{r}_N). \quad (2.2)$$

The form of Eq. 2.2 is very cumbersome for calculating potentials. It is customary and completely sufficient for our purposes to truncate it at the two-body term. This truncation is standard for rare-gas solids as higher-order terms are known to be negligible for many purposes. In this work we use a potential of the form

$$V(\boldsymbol{R}) = \sum_{i<j=1}^{N} v(r_{ij}), \quad (2.3)$$

where $r_{ij} = |\boldsymbol{r}_i - \boldsymbol{r}_j|$ is the separation of particles i and j. In our work we employ a range of pair potentials that are accurate for the differing systems we study. Further details can be found in Section 2.8 and Appendix F.

Whilst the Hamiltonian is sufficient to fully describe the system it is from the canonical density operator that we are able to calculate the quantities of interest [16]. The canonical density operator is given by

$$\hat{W}(\beta) = Z^{-1}(\beta) e^{-\beta \hat{H}}, \quad (2.4)$$

where the normalisation

$$Z(\beta) = \mathrm{Tr}\{e^{-\beta \hat{H}}\} \quad (2.5)$$

ensures that the canonical density operator is unit-normalised, i.e. $Tr\{\hat{W}(\beta)\}$ = 1. In Eqs. 2.4 and 2.5 we have $\beta = 1/k_B T$, where k_B is the Boltzmann constant. At a given temperature T, we can calculate a thermodynamic property P described by the operator $\hat{P}$ by taking the trace of the product of the operator with the canonical density operator,

$$P = \mathrm{Tr}\{\hat{P}\hat{W}(\beta)\}. \tag{2.6}$$

In order to make use of Eq. 2.6 it is useful to redefine the canonical density operator in co-ordinate space representation

$$W(\boldsymbol{R}, \boldsymbol{R}'; \beta) = Z^{-1}(\beta) \sum_{\lambda} e^{-\beta E_\lambda} \Psi_\lambda(\boldsymbol{R}) \Psi_\lambda^\star(\boldsymbol{R}'), \tag{2.7}$$

where $\Psi_\lambda(\boldsymbol{R})$ and its complex conjugate $\Psi_\lambda^\star(\boldsymbol{R}')$ are N-body wave functions that form a complete orthonormalized set of eigenfunctions of the Hamiltonian $\hat{H}$ with energy eigenvalues E_λ. Using Eqs. 2.6 and 2.7 along with the definitions of the potential and kinetic energy operators from Eqs. 2.1 and 2.3 we can write the potential and kinetic energies as

$$\begin{aligned} E_{\mathrm{pot}} &= \mathrm{Tr}\{\hat{V}\hat{W}(\beta)\} = \mathrm{Tr}\{V(\boldsymbol{R})\hat{W}(\beta)\} = \int V(\boldsymbol{R}) W(\boldsymbol{R}, \boldsymbol{R}; \beta) d\boldsymbol{R} \\ &= \sum_{i<j=1}^{N} \int v(r_{ij}) W(\boldsymbol{R}, \boldsymbol{R}; \beta) d\boldsymbol{R}, \end{aligned} \tag{2.8}$$

$$\begin{aligned} E_{\mathrm{kin}} &= \mathrm{Tr}\{\hat{T}\hat{W}(\beta)\} = -\frac{\hbar^2}{2m} \sum_{i=1}^{N} \mathrm{Tr}\{\nabla_i^2 \hat{W}(\beta)\} \\ &= -\frac{\hbar^2}{2m} \sum_{i=1}^{N} \int [\nabla_i'^2 W(\boldsymbol{R}, \boldsymbol{R}'; \beta)](\boldsymbol{R}' = \boldsymbol{R}) d\boldsymbol{R}. \end{aligned} \tag{2.9}$$

In Eq. 2.9 we first apply $\nabla_i'^2$ to $W(\boldsymbol{R}, \boldsymbol{R}'; \beta)$ before setting $\boldsymbol{R}' = \boldsymbol{R}$.

Two other quantities of interest are the local one- and two-body densities, $\varrho(\boldsymbol{x})$ and $\rho_2(\boldsymbol{x}_1, \boldsymbol{x}_2)$. The one-body density is the probability density of a particle being at position $\boldsymbol{x}$, whilst the two-body density is the joint probability density of a particle being at $\boldsymbol{x}_1$ when another is at $\boldsymbol{x}_2$. The respective operators are

$$\hat{\varrho}(\boldsymbol{x}) = \sum_{i=1}^{N} \delta(\boldsymbol{x} - \boldsymbol{r}_i) \tag{2.10}$$

$$\hat{\rho}_2(\boldsymbol{x}_1, \boldsymbol{x}_2) = \sum_{i \neq j=1}^{N} \delta(\boldsymbol{x}_1 - \boldsymbol{r}_i)\delta(\boldsymbol{x}_2 - \boldsymbol{r}_j). \tag{2.11}$$

Thus we are able to write the one- and two-body densities as

$$\begin{aligned} \varrho(\boldsymbol{x}) &= \mathrm{Tr}\{\hat{\varrho}(\boldsymbol{x})\hat{W}(\beta)\} = \sum_{i=1}^{N} \mathrm{Tr}\{\delta(\boldsymbol{x} - \boldsymbol{r}_i)\hat{W}(\beta)\} \\ &= N \int W(\boldsymbol{x}, \boldsymbol{r}_2, \cdots, \boldsymbol{r}_N, \boldsymbol{x}, \boldsymbol{r}_2, \cdots, \boldsymbol{r}_N; \beta) d\boldsymbol{r}_2 \cdots d\boldsymbol{r}_N \end{aligned} \tag{2.12}$$

and

$$\begin{aligned} \rho_2(\boldsymbol{x}_1, \boldsymbol{x}_2) =& \mathrm{Tr}\{\hat{\rho}_2(\boldsymbol{x}_1, \boldsymbol{x}_2)\hat{W}(\beta)\} = \sum_{i \neq j=1}^{N} \mathrm{Tr}\{\delta(\boldsymbol{x}_1 - \boldsymbol{r}_i)\delta(\boldsymbol{x}_2 - \boldsymbol{r}_j)\hat{W}(\beta)\} \\ =& N(N-1) \\ & \times \int W(\boldsymbol{x}_1, \boldsymbol{x}_2, \boldsymbol{r}_3, \cdots, \boldsymbol{r}_N, \boldsymbol{x}_1, \boldsymbol{x}_2, \boldsymbol{r}_3, \cdots, \boldsymbol{r}_N; \beta) d\boldsymbol{r}_3 \cdots d\boldsymbol{r}_N \end{aligned} \tag{2.13}$$

Eqs. 2.12 and 2.13 make use of the symmetry property of the density matrix under exchange of particles.

2.2 Symmetrized Representations of the One- and Two-Body Densities

In this section we will provide a rigorous description of the symmetries in the one- and two-body densities for an FCC solid. In particular we will discuss the Fourier transforms of the respective densities.

2.2.1 Symmetry Operators

A rotation of a position vector $\boldsymbol{r} = (x, y, z)$ by a general (proper or improper) rotation R leads to a position vector $\boldsymbol{r}' = (x', y', z')$. Expressed mathematically we have

$$\begin{bmatrix} x' \\ y' \\ z' \end{bmatrix} = \begin{bmatrix} a_{11} & a_{12} & a_{13} \\ a_{21} & a_{22} & a_{23} \\ a_{31} & a_{32} & a_{33} \end{bmatrix} \begin{bmatrix} x \\ y \\ z \end{bmatrix} \tag{2.14}$$

or more simply

$$\boldsymbol{r}' = R\boldsymbol{r}, \tag{2.15}$$

where R is the rotation matrix and $\boldsymbol{r}$ and $\boldsymbol{r}'$ are position vectors. The term rotation is used to imply both proper and improper rotations. A proper rotation is a rotation by some angle about an axis, whereas an improper rotation involves a proper rotation followed by either an inversion or reflection [7].

The most important of all symmetry operations is the identity. The identity is given the symbol E in Schoenflies notation and is the operation of mapping

the object onto itself. The rotation matrix for the identity operation is the three-dimensional identity matrix

$$R_E = \begin{bmatrix} 1 & 0 & 0 \\ 0 & 1 & 0 \\ 0 & 0 & 1 \end{bmatrix}. \tag{2.16}$$

Closely related to the identity operation is the inversion through the origin, by which a position (x, y, z) becomes $(-x, -y, -z)$. The inversion operation is given the symbol I and its rotation matrix is given by

$$R_I = \begin{bmatrix} -1 & 0 & 0 \\ 0 & -1 & 0 \\ 0 & 0 & -1 \end{bmatrix}. \tag{2.17}$$

The notation for proper rotations needs to specify both the angle of rotation and the axis about which the rotation occurs. In this work the angle of a rotation is given by $2\pi/n$, where n is the order of rotation. We shall show in later discussions that for crystallographic systems $n = 1, 2, 3, 4, 6$ only. Proper rotations are given the symbol C. One thus represents a rotation of 180° about the z-axis as C_{2z}.

A reflection across a mirror plane is denoted by the symbol σ in the Schoenflies notation. The orientation of the plane is denoted by a subscript which is perpendicular to the mirror plane. Thus the operation σ_z is a reflection across the xy-plane.

The final type of symmetry operator is that of a combination of a proper rotation with the inversion. It can be considered as a compound operation of a proper rotation, C_n, followed by an inversion, I. These operators are given the symbol S in the Schoenflies notation with a subscript of the same form as a proper rotation.

2.2.2 Lattice, Point and Space Group Theory

A Bravais lattice can be defined as an infinite array of points that appear identically distributed regardless of the point of reference [7]. Furthermore by using the principle of translational invariance [7] it is possible to define a Bravais lattice in terms of primitive translation vectors

$$\boldsymbol{t} = n_1\boldsymbol{a} + n_2\boldsymbol{b} + n_3\boldsymbol{c}, \tag{2.18}$$

where $\boldsymbol{a}$ and $\boldsymbol{b}$ are not collinear and $\boldsymbol{c}$ is not coplanar with plane $\boldsymbol{ab}$. No other conditions are imposed on the vectors. The FCC structure is formed by placing an atom either at each Bravais lattice point or some identical position from each Bravais lattice point. By taking the three vectors $\boldsymbol{a}$, $\boldsymbol{b}$ and $\boldsymbol{c}$ from a common origin we can define a primitive unit cell of the FCC structure that, by definition, contains only one atom.

Burns and Glazer [7] show that by considering increasing orders of the symmetry operators, outlined in Section 2.2.1, that seven basic crystal structures are formed. The seven crystal types are Triclinic (only E and I), Monoclinic (one

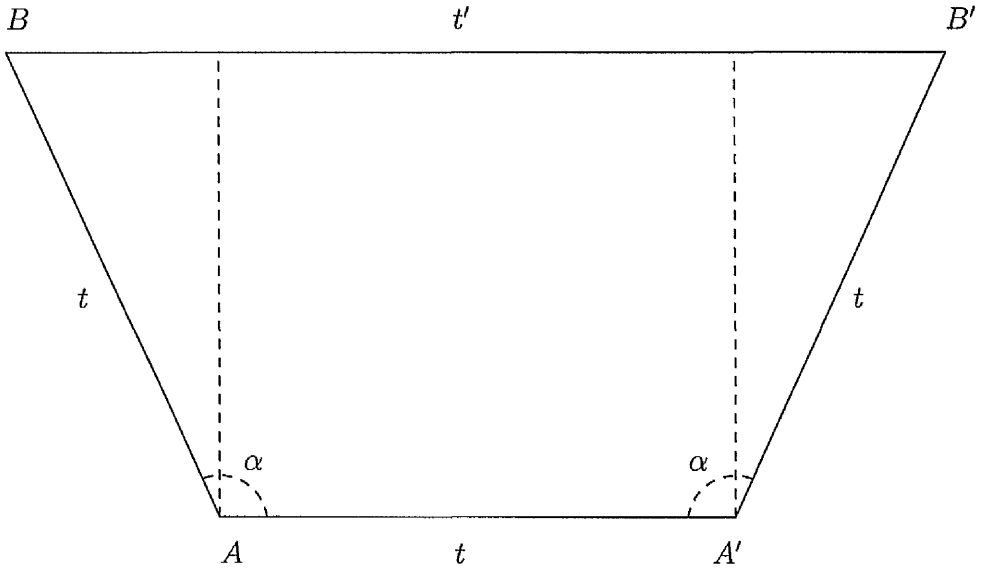

Figure 2.1: General lattice configuration.

C_2), Orthorhombic (two C_2), Tetragonal (one C_4), Cubic (four C_3), Trigonal (one C_3) and Hexagonal (one C_6), of which we are concerned only with cubic structures in this work. The methods outlined here in our work are valid for all symmorphic space groups the meaning of which will become clear later. Burns and Glazer [7] also present a rigorous proof that the only allowed orders for the symmetry operations are $1, 2, 3, 4$ and 6. The proof is outlined here for completeness.

In Figure 2.1 (taken from Ref.[7]) we consider two lattice points A and A' that are separated by a lattice spacing t. A rotation of the vector AA' about A by a symmetry operation R leads to a new point B, similarly a rotation of the vector $A'A$ about A' by the inverse operation R^{-1} leads to a new point B'. We

find from basic geometric relations that the spacing between B and B' is

$$t' = -2t\cos(\alpha) + t. \tag{2.19}$$

It is a requirement of a lattice that the spacing t' is an integer multiple of the lattice spacing t. We therefore have the condition

$$t' = mt, \tag{2.20}$$

where m is an integer. These two equations lead to

$$\cos(\alpha) = (1 - m)/2. \tag{2.21}$$

A further requirement is that $0 \leq \alpha \leq \pi$ [7]. This leads to

$$|(1 - m)/2| = |\cos(\alpha)| \leq 1, \tag{2.22}$$

and

$$|1 - m| = |M| \leq 2, \tag{2.23}$$

where M must also be an integer. We therefore have

$$M = -2, -1, 0, 1, 2, \tag{2.24}$$

leading to

$$\alpha = \pi, 2\pi/3, \pi/2, \pi/3, 0 \tag{2.25}$$

or put in terms of 2π

$$\alpha = 2\pi/2, 2\pi/3, 2\pi/4, 2\pi 6, 2\pi/1. \tag{2.26}$$

The 32 point groups arise from considering combinations of symmetry operations. All symmetry operations in a point group must have one point in common. A point group is a group in the mathematical sense. The members of a set must obey the the following rules for the set to form a group [7].

1. The product of two operations is also a member of the set.

2. The set includes the identity.

3. Each operation has an inverse.

4. Multiplication is associative.

For cubic lattice structures there are 5 point groups of which the highest-order group has 48 symmetry operations and is given the symbol O_h in Schoenflies notation. These symmetry operations are listed in Appendix D. The point group O_h is centrosymmetric.

Finally we come to the concept of a space group, where the various point groups are tied to specific lattice types. Space group operators are described by the Seitz operator

$$\{R, \boldsymbol{t}\}\boldsymbol{r} = R\boldsymbol{r} + \boldsymbol{t}, \tag{2.27}$$

where R is a point group rotation and $\boldsymbol{t}$ a translation vector. A group is deemed symmorphic if the only allowed translation vectors, $\boldsymbol{t}$, are primitive translation vectors. For simple cubic, FCC and BCC crystals this is the case. In a non-symmorphic space group certain rotations occur only in conjunction with certain

non-primitive translations. Multiplication of two space group operators $\{R_1, \boldsymbol{t}_1\}$ and $\{R_2, \boldsymbol{t}_2\}$, where R_1 and R_2 are from the same point group, is defined as [16]

$$\{R_1, \boldsymbol{t}_1\}\{R_2, \boldsymbol{t}_2\} = \{R_1 R_2, R_1 \boldsymbol{t}_2 + \boldsymbol{t}_1\}. \tag{2.28}$$

The inverse element $\{R, \boldsymbol{t}\}^{-1}$ can be derived from Eq. 2.28, yielding

$$\{R, \boldsymbol{t}\}^{-1} = \{R^{-1}, -R^{-1}\boldsymbol{t}\}, \tag{2.29}$$

where R^{-1} is the inverse of the rotation matrix R and in a Cartesian reference frame $R^{-1} = R^T$ [16].

Transforming a point $\boldsymbol{r}$ by all rotations M of the point group will result in L unique points being generated, where $L \leq M$. The case of $L < M$ is easiest to imagine for all rotations applied to the origin, $(0, 0, 0)$, since for any rotation we will always reproduce the origin.

2.2.3 The One-Body Density

Our aim in this section is to exploit the symmetries of the crystalline structure in calculating the one-body density. To achieve this it is necessary to expand the concept of a vector transformation, as used in space groups, to the transformation of a scalar function [16]. We outline here the arguments presented by Cornwell [10]. The value of a scalar field at a point $\boldsymbol{r}$ is given by the function $f(\boldsymbol{r})$ in a given coordinate system $\boldsymbol{r} = (x, y, z)$. By choosing a different coordinate system (x', y', z') the value for the same point is now given by the function $f'(\boldsymbol{r}')$, leading

to

$$f'(\boldsymbol{r}') = f(\boldsymbol{r}). \tag{2.30}$$

If the primed coordinate system is a rotation of the unprimed coordinate system, $\boldsymbol{r}' = \{R, \boldsymbol{t}\}\boldsymbol{r}$, then Eq. 2.30 becomes

$$f'(\boldsymbol{r}') = f\left(\{R, \boldsymbol{t}\}^{-1}\boldsymbol{r}'\right). \tag{2.31}$$

For a given rotation $\{R, \boldsymbol{t}\}$ there is a one-to-one correspondence between $f'(\boldsymbol{r})$ and $f(\boldsymbol{r})$, allowing us to consider f' as being the result of an operator $P\left(\{R, \boldsymbol{t}\}\right)$ acting on f,

$$\left[P\left(\{R, \boldsymbol{t}\}\right) f\right](\boldsymbol{r}) = f\left(\{R, \boldsymbol{t}\}^{-1}\boldsymbol{r}\right). \tag{2.32}$$

An important property of the scalar transformation operator P is the result of multiplication with another scalar transformation operator. We consider two operators P_1, P_2 acting successively on a function $f(\boldsymbol{r})$.

$$P(\{R_1, \boldsymbol{t}_1\})P(\{R_2, \boldsymbol{t}_2\})f(\boldsymbol{r}) = P(\{R_1, \boldsymbol{t}_1\})g(\boldsymbol{r}) = g(\{R_1, \boldsymbol{t}_1\}^{-1}\boldsymbol{r}), \tag{2.33}$$

where

$$g(\boldsymbol{r}) = P(\{R_2, \boldsymbol{t}_2\})f(\boldsymbol{r}) = f(\{R_2, \boldsymbol{t}_2\}^{-1}\boldsymbol{r}) \tag{2.34}$$

leading to

$$g(\{R_1, \boldsymbol{t}_1\}^{-1}\boldsymbol{r}) = f(\{R_2, \boldsymbol{t}_2\}^{-1}\{R_1, \boldsymbol{t}_1\}^{-1}\boldsymbol{r}). \tag{2.35}$$

Using Eqs 2.28 and 2.29 it can be shown that

$$\{R_2, \boldsymbol{t}_2\}^{-1}\{R_1, \boldsymbol{t}_1\}^{-1} = \left[\{R_1, \boldsymbol{t}_1\}\{R_2, \boldsymbol{t}_2\}\right]^{-1}, \tag{2.36}$$

leading to

$$P(\{R_1, \boldsymbol{t}_1\})P(\{R_2, \boldsymbol{t}_2\})f(\boldsymbol{r}) = P\left(\{R_1, \boldsymbol{t}_1\}\{R_2, \boldsymbol{t}_2\}\right) f(\boldsymbol{r}). \tag{2.37}$$

Equation 2.37 is useful as it shows that the scalar transformation operators $P(\{R, \boldsymbol{t}\})$ obey the same multiplication rules as the vector transformation operators $\{R, \boldsymbol{t}\}$. Where a set of scalar transformation operators involves only transformations of a group $\mathcal{G}$, the set is said to be isomorphic to the crystallographic space group $\mathcal{G}$ [16].

Applying a scalar transformation to the one-body density we see that

$$P(\{R, \boldsymbol{t}\})\varrho(\boldsymbol{x}) = \varrho(\boldsymbol{x}) \quad \forall\{R, \boldsymbol{t}\} \in \mathcal{G}, \tag{2.38}$$

which states that $\rho(\boldsymbol{x})$ is invariant for the space group $\mathcal{G}$, where $\mathcal{G}$ is the space group of the crystal [16]. The invariance property of Eq. 2.38 implies that the one-body density also has the symmetries of the underlying Bravais lattice and allows us to express $\varrho(\boldsymbol{x})$ as a lattice Fourier series [16]

$$\varrho(\boldsymbol{x}) = \sum_{\boldsymbol{K}} \rho(\boldsymbol{K}) e^{i\boldsymbol{K}\boldsymbol{x}}, \tag{2.39}$$

where the summation is over all reciprocal lattice vectors. The lattice Fourier coefficients are given by [16]

$$\rho(\boldsymbol{K}) = \frac{1}{\Omega} \int_{\Omega} \varrho(\boldsymbol{x}) e^{-i\boldsymbol{K}\boldsymbol{x}} d\boldsymbol{x}, \tag{2.40}$$

where the integral is over the volume Ω of a primitive unit cell. The so-called time-reversal symmetry, $\rho(-\boldsymbol{K}) = \rho^*(\boldsymbol{K})$, is a direct result of the reality of $\varrho(\boldsymbol{x})$,

where $\rho^*(\boldsymbol{K})$ is the complex conjugate. The point group of the reciprocal lattice is the same as that of the Bravais lattice [10].

The unitarity property [10] states that for two functions f_1 and f_2 their scalar product is invariant under a scalar transformation operator, expressed mathematically as

$$\begin{aligned}\langle f_1|f_2\rangle &= \frac{1}{\Omega}\int_\Omega f_1^*(\boldsymbol{x})f_2(\boldsymbol{x})d\boldsymbol{x} \\ &= \frac{1}{\Omega}\int_\Omega [P(\{R,\boldsymbol{x}_0\})f_1]^*(\boldsymbol{x})[P(\{R,\boldsymbol{x}_0\})f_2](\boldsymbol{x})d\boldsymbol{x} \\ &= \sum_{\boldsymbol{K}} \tilde{f}_1^*(\boldsymbol{K})\tilde{f}_2(\boldsymbol{K}),\end{aligned} \tag{2.41}$$

where $\tilde{f}$ represents the lattice Fourier transform. Replacing f_1 with $e^{i\boldsymbol{K}\boldsymbol{x}}$, f_2 with $\varrho(\boldsymbol{x})$ and $\{R,\boldsymbol{x}_0\}$ with $\{R,\boldsymbol{t}\}$ we find,

$$\begin{aligned}\rho(\boldsymbol{K}) &= \frac{1}{\Omega}\int_\Omega \varrho(\boldsymbol{x})e^{i\boldsymbol{K}\boldsymbol{x}}d\boldsymbol{x} \\ &= \frac{1}{\Omega}\int_\Omega P(\{R,\boldsymbol{t}\})\varrho(\boldsymbol{x})e^{i\boldsymbol{K}(R^{-1}\boldsymbol{x}-R^{-1}\boldsymbol{t})}d\boldsymbol{x} \\ &= \rho(R\boldsymbol{K}),\end{aligned} \tag{2.42}$$

where we have have made use of the invariance property as given in Eq. 2.38. Equation 2.42 permits us to restrict the calculation of Fourier coefficients to $\boldsymbol{K}$-vectors only out of an asymmetric unit. The one-body density may therefore be computed via

$$\varrho(\boldsymbol{x}) = \sum_{\boldsymbol{K}\in \mathrm{AS}} \frac{\rho(\boldsymbol{K})}{g_0(\boldsymbol{K})}\sum_{j=1}^{g_0} e^{i\boldsymbol{K}(j)\boldsymbol{x}}, \tag{2.43}$$

where $\boldsymbol{K}(j) = R_j\boldsymbol{K}$ with j enumerating the rotation operations of the point group, $g_0(\boldsymbol{K})$ is the number of rotations that send $\boldsymbol{K}$ into itself and g_0 is the total

number of rotations in the point group $\mathcal{G}_0$. The derivation of the representation of the asymmetric unit is given in Section 2.7.2. A useful result is the Fourier component for $\boldsymbol{K} = 0$. Looking at Eq. 2.40 we obtain

$$\rho(\boldsymbol{K} = 0) = \frac{1}{\Omega} \int_{\Omega} \varrho(\boldsymbol{x}) d\boldsymbol{x} = \rho_0, \tag{2.44}$$

which is the number of particles in the primitive unit cell divided by the volume of the primitive unit cell, i.e. simply the bulk particle density ρ_0.

2.2.4 The Two-Body Density

The symmetries of the two-body density can be considered in a analogous manner to the one-body density. As in Eq. 2.32 we define a scalar transformation operator [16]

$$[P_2(\{R, \boldsymbol{t}\})h_2](\boldsymbol{x}_1, \boldsymbol{x}_2) = h_2(\{R, \boldsymbol{t}\}^{-1}\boldsymbol{x}_1, \{R, \boldsymbol{t}\}^{-1}\boldsymbol{x}_2). \tag{2.45}$$

We employ a change of variables,

$$\boldsymbol{S} = \tfrac{1}{2}(\boldsymbol{x}_1 + \boldsymbol{x}_2) \quad \text{and} \quad \boldsymbol{r} = \boldsymbol{x}_1 - \boldsymbol{x}_2 \tag{2.46}$$

thus allowing the scalar function to be expressed as

$$h(\boldsymbol{S}, \boldsymbol{r}) = h_2\left(\boldsymbol{S} + \tfrac{1}{2}\boldsymbol{r}, \boldsymbol{S} - \tfrac{1}{2}\boldsymbol{r}\right), \tag{2.47}$$

$\boldsymbol{S}$ being the centre of mass of the particles and $\boldsymbol{r}$ the relative position vector between the two particles. The function space operator from Eq. 2.45 is now

represented as the multiplication of two operators [16]

$$\begin{aligned}[P_2(\{R,\boldsymbol{t}\})h_2](\boldsymbol{x}_1,\boldsymbol{x}_2) &= [P_{\boldsymbol{S}}(\{R,\boldsymbol{t}\})P_r(R)h](\boldsymbol{S},\boldsymbol{r}) \\ &= h(\{R,\boldsymbol{t}\}^{-1}\boldsymbol{S},R^{-1}\boldsymbol{r}),\end{aligned} \tag{2.48}$$

where $P_{\boldsymbol{S}}$ acts on the centre of mass $\boldsymbol{S}$ and P_r acts on the relative coordinate $\boldsymbol{r}$. The application to the two-body density $\rho_2(\boldsymbol{x}_1,\boldsymbol{x}_2)$ is achieved by setting $h_2=\rho_2$ and $h=\varrho_2$. As with the one-body density for a transformation $\{R,\boldsymbol{t}\}$ of a space group $\mathcal{G}$ we see that the invariance property of the two-body density may be expressed as

$$P_{\boldsymbol{S}}(\{R,\boldsymbol{t}\})P_r(R)\varrho_2(\boldsymbol{S},\boldsymbol{r})=\varrho_2(\{R,\boldsymbol{t}\}^{-1}\boldsymbol{S},R^{-1}\boldsymbol{r})=\varrho_2(\boldsymbol{S},\boldsymbol{r}). \tag{2.49}$$

A result of Eq. 2.49 is that $\varrho_2(\boldsymbol{S},\boldsymbol{r})$ may be expressed as a lattice Fourier transform

$$\varrho_2(\boldsymbol{S},\boldsymbol{r})=\sum_{\boldsymbol{K}}u(\boldsymbol{r};\boldsymbol{K})e^{i\boldsymbol{K}\boldsymbol{S}}. \tag{2.50}$$

The Fourier coefficients $u(\boldsymbol{r};\boldsymbol{K})$ are given by

$$u(\boldsymbol{r};\boldsymbol{K})=\frac{1}{\Omega}\int_{\Omega}\varrho_2(\boldsymbol{S},\boldsymbol{r})e^{-i\boldsymbol{K}\boldsymbol{S}}d\boldsymbol{S}, \tag{2.51}$$

where as before the integral extends over a primitive unit cell of volume Ω.

The two fundamental symmetries of the two-body density are the reality of $\varrho_2(\boldsymbol{x}_1,\boldsymbol{x}_2)$ and the symmetry under exchange of particles $\boldsymbol{x}_1$ and $\boldsymbol{x}_2$. Furthermore since we are dealing with an FCC crystal structure the two-body density is centro-symmetric as this is a property of the FCC space group. These three symmetries

can be expressed in terms of the Fourier coefficients $u(\boldsymbol{r};\boldsymbol{K})$ as

$$u(\boldsymbol{r};\boldsymbol{K}) = u^*(\boldsymbol{r};-\boldsymbol{K}) \qquad \text{reality,} \tag{2.52a}$$

$$u(\boldsymbol{r};\boldsymbol{K}) = u(-\boldsymbol{r};\boldsymbol{K}) \qquad \text{exchange,} \tag{2.52b}$$

$$u(\boldsymbol{r};\boldsymbol{K}) = u(-\boldsymbol{r};-\boldsymbol{K}) \qquad \text{centrosymmetry.} \tag{2.52c}$$

The effect of $P_{\boldsymbol{r}}(R)$ on the Fourier coefficients, with R a general rotation, is

$$\begin{aligned} P_{\boldsymbol{r}}(R)u(\boldsymbol{r};\boldsymbol{K}) &= u(R^{-1}\boldsymbol{r};\boldsymbol{K}) \\ &= e^{i(R\boldsymbol{K})\boldsymbol{S}_0}\left\{\frac{1}{\Omega}\int_{\Omega} P_{\boldsymbol{S}}(\{R,\boldsymbol{S}_0\})P_{\boldsymbol{r}}(R)\varrho_2(\boldsymbol{S},\boldsymbol{r})e^{-i(R\boldsymbol{K})\boldsymbol{S}}d\boldsymbol{S}\right\}. \end{aligned} \tag{2.53}$$

Setting $\boldsymbol{S}_0 = \boldsymbol{t}$, with $\boldsymbol{t}$ being a primitive translation vector, and taking R from the point group we find

$$P_{\boldsymbol{r}}(R)u(\boldsymbol{r};\boldsymbol{K}) = u(\boldsymbol{r};R\boldsymbol{K}). \tag{2.54}$$

We find in an analogous way to Eq. 2.42 for the one-body density, that we can now express the two-body density in the symmetrized form

$$\varrho_2(\boldsymbol{S},\boldsymbol{r}) = \sum_{\boldsymbol{K}\in \mathrm{AS}} \sum_{j=1}^{M(\boldsymbol{K})} [P_{\boldsymbol{r}}(R_j)u(\boldsymbol{r};\boldsymbol{K})]e^{i(R_j\boldsymbol{K})\boldsymbol{S}}, \tag{2.55}$$

where we need only consider those $\boldsymbol{K}$-vectors that are within the asymmetric unit. The form of the second sum in Eq. 2.55 ensures that all vectors, $R_j\boldsymbol{K}$, generated are unique. For every $\boldsymbol{K} \in$ AS the $M(\boldsymbol{K})$ vectors $R_j\boldsymbol{K}$ with $1 \le j \le M(\boldsymbol{K}) = \frac{g_0}{g_0(\boldsymbol{K})}$ are the $M(\boldsymbol{K})$ distinct mutually symmetry-equivalent $\boldsymbol{K}$-vectors generated from that $\boldsymbol{K} \in$ AS by applying all $R \in \mathcal{G}_0$ to $\boldsymbol{K}$. Here $g_0(\boldsymbol{K})$ is the order of

the subgroup $\mathcal{G}_0(\boldsymbol{K}) \subseteq \mathcal{G}_0$ of rotations that send $\boldsymbol{K}$ into itself. The rotations R_j producing the set $\{R_j\boldsymbol{K}|1 \leq j \leq M(\boldsymbol{K})\}$ of distinct symmetry-equivalent $\boldsymbol{K}$-vectors are in general not unique, however the $M(\boldsymbol{K})$ distinct symmetry-equivalent $\boldsymbol{K}$-vectors $R_j\boldsymbol{K}$ are.

The two-body density as given in Eq. 2.55 can be considered as a sum of $\boldsymbol{K}$-component functions

$$\varrho_2(\boldsymbol{S}, \boldsymbol{r}) = \sum_{\boldsymbol{K}\in\mathrm{AS}} t_2(\boldsymbol{S}, \boldsymbol{r}; \boldsymbol{K}), \tag{2.56}$$

where

$$t_2(\boldsymbol{S}, \boldsymbol{r}; \boldsymbol{K}) = \sum_{j=1}^{M(\boldsymbol{K})} [P_r(R_j)u(\boldsymbol{r}; \boldsymbol{K})]e^{i(R_j\boldsymbol{K})\boldsymbol{S}}. \tag{2.57}$$

In addition to taking $\boldsymbol{K}$-vectors only from the asymmetric unit, further symmetries can be found in the expansion of the Fourier components $u(\boldsymbol{r}; \boldsymbol{K})$. To aid with the identification of symmetries it is necessary to rotate the coordinate frame such that the $\boldsymbol{K}$-vector points along the new z-axis [17]. The rotation is achieved by multiplication with a matrix $R_0(\boldsymbol{K})$ where the rotation matrix $R_0(\boldsymbol{K})$ is the product of two rotations. Firstly a counter-clockwise rotation about the x-axis through an angle γ is performed, where the angle γ is the angle that $\boldsymbol{K}$ encloses with the z-axis. A second rotation is then applied about the z-axis, through an angle β which is the angle between the $-y$-axis and the projection of $\boldsymbol{K}$ onto the

xy-plane. The rotation matrix obtained from the above rotations is

$$R_0(\boldsymbol{K}) = \begin{pmatrix} \cos(\beta) & -\sin(\beta)\cos(\gamma) & \sin(\beta)\sin(\gamma) \\ \sin(\beta) & \cos(\beta)\cos(\gamma) & -\cos(\beta)\sin(\gamma) \\ 0 & \sin(\gamma) & \cos(\gamma) \end{pmatrix}, \tag{2.58}$$

where

$$\cos(\gamma) = \frac{K_z}{|\boldsymbol{K}|}, \tag{2.59}$$

and

$$\cos(\beta) = -\frac{K_y}{\sqrt{K_x^2 + K_y^2}}. \tag{2.60}$$

The function $u(\boldsymbol{r};\boldsymbol{K})$ in the fixed frame is related to $u_{\rm rot}(\boldsymbol{r}';\boldsymbol{K})$ in the rotated frame via [17]

$$u_{\rm rot}(\boldsymbol{r}';\boldsymbol{K}) = u(\boldsymbol{r};\boldsymbol{K}), \tag{2.61}$$

where $\boldsymbol{r}' = R_0^T(\boldsymbol{K})\boldsymbol{r}$. The rotated function $u_{\rm rot}(\boldsymbol{r}';\boldsymbol{K})$ can be expressed as a series [17]

$$u_{\rm rot}(\boldsymbol{r}';\boldsymbol{K}) = \sum_{\gamma=-\infty}^{\infty} h_\gamma^{(\rm rot)}(r,\Theta;\boldsymbol{K})e^{i\gamma\phi}, \tag{2.62}$$

where Θ and ϕ are the polar and azimuthal angles in the rotated frame and $r = |\boldsymbol{r}| = |\boldsymbol{r}'|$ is the relative distance. The functions $h_\gamma^{(\rm rot)}(r,\Theta;\boldsymbol{K})$ are given by [17]

$$h_\gamma^{(\rm rot)}(r,\Theta;\boldsymbol{K}) = \frac{1}{2\pi}\int_0^{2\pi} u_{\rm rot}(\boldsymbol{r}';\boldsymbol{K})e^{-i\gamma\phi}d\phi, \tag{2.63a}$$

$$= \frac{1}{2\pi}\int_0^{2\pi} u(\boldsymbol{r};\boldsymbol{K})e^{-i\gamma\phi}d\phi, \tag{2.63b}$$

$$= \frac{1}{2\pi V}\int_V\int_0^{2\pi} \varrho_2(\boldsymbol{S}, R_0(\boldsymbol{K})\boldsymbol{r}')e^{-i\boldsymbol{K}\boldsymbol{S}}e^{-i\gamma\phi}d\boldsymbol{S}d\phi. \tag{2.63c}$$

When the symmetries of the space group are applied to the functions $h_\gamma^{(\mathrm{rot})}(r,\Theta;\boldsymbol{K})$ we find that only a subset of the infinite series, Eq. 2.62, contributes to $u_{\mathrm{rot}}(\boldsymbol{r}';\boldsymbol{K})$. These subsets vary depending on the $\boldsymbol{K}$-vector.

Before we consider the subset of rotations for a given $\boldsymbol{K}$-vector we shall first look at the effect of the fundamental symmetries of the two-body density. The exchange of two particles has the same effect on $u(\boldsymbol{r};\boldsymbol{K})$ as that of an inversion, I. We have shown that the Fourier component functions, $u_{\mathrm{rot}}(\boldsymbol{r}';\boldsymbol{K})$, are unaffected by such exchanges (Eq. 2.52b). The polar, Θ, and azimuthal, ϕ, angles of $\boldsymbol{r}'$ do change under inversion such that

$$\Theta \rightarrow \pi - \Theta, \tag{2.64a}$$

$$\phi \rightarrow \phi + \pi. \tag{2.64b}$$

Thus we find that

$$\begin{aligned} u_{\mathrm{rot}}(-\boldsymbol{r}';\boldsymbol{K}) &= \sum_{\gamma=-\infty}^{\infty} h_\gamma^{(\mathrm{rot})}(r,\pi-\Theta;\boldsymbol{K}) e^{i\gamma(\phi+\pi)} \\ &= \sum_{\gamma=-\infty}^{\infty} h_\gamma^{(\mathrm{rot})}(r,\pi-\Theta;\boldsymbol{K})(-1)^\gamma e^{i\gamma\phi} \\ &= u_{\mathrm{rot}}(\boldsymbol{r}';\boldsymbol{K}) \\ &= \sum_{\gamma=-\infty}^{\infty} h_\gamma^{(\mathrm{rot})}(r,\Theta;\boldsymbol{K}) e^{i\gamma\phi} \end{aligned} \tag{2.65}$$

from which we find that

$$h_\gamma^{(\mathrm{rot})}(r,\pi-\Theta;\boldsymbol{K}) = (-1)^\gamma h_\gamma^{(\mathrm{rot})}(r,\Theta;\boldsymbol{K}). \tag{2.66}$$

The other fundamental symmetry of the two-body density is its reality (Eq. 2.52a),

$$\begin{aligned} u^*_{\rm rot}(\boldsymbol{r}';\boldsymbol{K}) &= u_{\rm rot}(\boldsymbol{r}';\boldsymbol{K}) \\ &= \sum_{\gamma=-\infty}^{\infty} h^{*({\rm rot})}_{\gamma}(r,\Theta;\boldsymbol{K})e^{-i\gamma\phi} \\ &= \sum_{\gamma=-\infty}^{\infty} h^{*({\rm rot})}_{-\gamma}(r,\Theta;\boldsymbol{K})e^{i\gamma\phi} \\ &= \sum_{\gamma=-\infty}^{\infty} h^{({\rm rot})}_{\gamma}(r,\Theta;\boldsymbol{K})e^{i\gamma\phi}, \end{aligned} \tag{2.67}$$

which yields the following two relations

$$h^{({\rm rot})}_{-\gamma}(r,\Theta;\boldsymbol{K}) = h^{*({\rm rot})}_{\gamma}(r,\Theta;\boldsymbol{K}), \tag{2.68a}$$

$$h^{({\rm rot})}_{0}(r,\Theta;\boldsymbol{K}) = h^{*({\rm rot})}_{0}(r,\Theta;\boldsymbol{K}) = h^{({\rm rot})}_{0}(r,\pi-\Theta;\boldsymbol{K}). \tag{2.68b}$$

Equation 2.68b states that for $\gamma = 0$ the function $h^{({\rm rot})}_0$ is real. This holds for all structures including liquids, as it is derived from the exchange symmetry of the two-body density and not from the crystal symmetries. Equally important is Eq. 2.68a, as this allows us to consider only positive and zero values of γ, again this is due to the symmetries of the two-body density not those of the crystal.

Using these fundamental symmetries of the two-body density we can write,

for a general $\boldsymbol{K}$-vector, the Fourier component function as

$$u_{\mathrm{rot}}(\boldsymbol{r}';\boldsymbol{K}) = h_0^{(\mathrm{rot})}(r,\Theta;\boldsymbol{K}) + \sum_{n=1}^{\infty}(h_n^{(\mathrm{rot})}(r,\Theta;\boldsymbol{K})e^{in\phi} + h_n^{*(\mathrm{rot})}(r,\Theta;\boldsymbol{K})e^{-in\phi}) \tag{2.69a}$$

$$= h_0^{(\mathrm{rot})}(r,\Theta;\boldsymbol{K}) + \sum_{n=1}^{\infty}\left\{h_n^{(\mathrm{rot})}(r,\Theta;\boldsymbol{K}) + h_n^{*(\mathrm{rot})}(r,\Theta;\boldsymbol{K})\right\}\cos(n\phi)$$
$$+ i\sum_{n=1}^{\infty}\left\{h_n^{(\mathrm{rot})}(r,\Theta;\boldsymbol{K}) - h_n^{*(\mathrm{rot})}(r,\Theta;\boldsymbol{K})\right\}\sin(n\phi) \tag{2.69b}$$

$$= \mathrm{Re}\left\{h_0^{(\mathrm{rot})}(r,\Theta;\boldsymbol{K})\right\} + 2\sum_{n=1}^{\infty}\mathrm{Re}\left\{h_n^{(\mathrm{rot})}(r,\Theta;\boldsymbol{K})\right\}\cos(n\phi)$$
$$- 2\sum_{n=1}^{\infty}\mathrm{Im}\left\{h_n^{(\mathrm{rot})}(r,\Theta;\boldsymbol{K})\right\}\sin(n\phi). \tag{2.69c}$$

There are six high-symmetry $\boldsymbol{K}$-vectors associated with the asymmetric unit. These are described along with the asymmetric unit in Section 2.7.2. The high-symmetry vectors have a degeneracy, $g_0(\boldsymbol{K})$, greater than 1. The degeneracies are given in Appendix D along with lists of symmetry-equivalent rotation matrices for each high-symmetry vector. For a given $\boldsymbol{K}$-vector symmetry-equivalent rotations yield the same vector, when applied to $\boldsymbol{K}$. It is a result of these symmetry-equivalent rotations that further restrictions can be placed on the series expansion of the Fourier coefficients.

Considering vectors of the type $\boldsymbol{K}_1$ we see from Table D.2 that $u_{\mathrm{rot}}(\boldsymbol{r}';\boldsymbol{K}_1)$ must be invariant under the rotations $\{1,16,21,28\} = \{E,\sigma_z,C'_{2b},\sigma_{d1}\}$ and $\{2,15,22,27\} = \{I,C_{2z},\sigma_{d2},C'_{2a}\}$. The first set of rotations are the symmetry-equivalent rotations for the identity, and the second are those that are equivalent to the inversion, which must be included because of the fundamental exchange

(x, y, z) frame	(x', y', z') frame
E	E
σ_z	$\sigma_{y'}$
C'_{2b}	$C_{2z'}$
σ_{d1}	$\sigma_{x'}$
I	I
C_{2z}	$C_{2y'}$
σ_{d2}	$\sigma_{z'}$
C'_{2a}	$C_{2x'}$

Table 2.1: Laue class for $\boldsymbol{K}_1$ vectors in both primed and unprimed frames.

symmetry of the two-body density. The two sets together define the Laue class for the vectors of type $\boldsymbol{K}_1$. The rotations listed are for the unrotated frame, so they must be rotated to the rotated frame before applying them to the component functions $h^{(\mathrm{rot})}$. The direction of the group rotations in the rotated (primed) frame is given by

$$\boldsymbol{n}' = R_0^T(\boldsymbol{K}_1)\boldsymbol{n}, \tag{2.70}$$

where $R_0(\boldsymbol{K}_1)$ is the matrix given in Eq. 2.58. The result of applying this rotation to the Laue class is given in Table 2.1. Applying these rotations to the component

functions $h^{(\mathrm{rot})}$ of $u_{\mathrm{rot}}(\boldsymbol{r}';\boldsymbol{K}_1)$ we find

$$P_\theta(E)P_\phi(E)\left[h_\gamma^{(\mathrm{rot})}(r,\Theta;\boldsymbol{K}_1)e^{i\gamma\phi}\right]=h_\gamma^{(\mathrm{rot})}(r,\Theta;\boldsymbol{K}_1)e^{i\gamma\phi} \tag{2.71a}$$

$$P_\theta(\sigma_{y'})P_\phi(\sigma_{y'})\left[h_\gamma^{(\mathrm{rot})}(r,\Theta;\boldsymbol{K}_1)e^{i\gamma\phi}\right]=h_\gamma^{(\mathrm{rot})}(r,\Theta;\boldsymbol{K}_1)e^{-i\gamma\phi} \tag{2.71b}$$

$$P_\theta(C_{2z'})P_\phi(C_{2z'})\left[h_\gamma^{(\mathrm{rot})}(r,\Theta;\boldsymbol{K}_1)e^{i\gamma\phi}\right]=(-1)^\gamma h_\gamma^{(\mathrm{rot})}(r,\Theta;\boldsymbol{K}_1)e^{i\gamma\phi} \tag{2.71c}$$

$$P_\theta(\sigma_{x'})P_\phi(\sigma_{x'})\left[h_\gamma^{(\mathrm{rot})}(r,\Theta;\boldsymbol{K}_1)e^{i\gamma\phi}\right]=(-1)^\gamma h_\gamma^{(\mathrm{rot})}(r,\Theta;\boldsymbol{K}_1)e^{-i\gamma\phi} \tag{2.71d}$$

$$P_\theta(I)P_\phi(I)\left[h_\gamma^{(\mathrm{rot})}(r,\Theta;\boldsymbol{K}_1)e^{i\gamma\phi}\right]=h_\gamma^{(\mathrm{rot})}(r,\Theta;\boldsymbol{K}_1)e^{i\gamma\phi} \tag{2.71e}$$

$$P_\theta(C_{2y'})P_\phi(C_{2y'})\left[h_\gamma^{(\mathrm{rot})}(r,\Theta;\boldsymbol{K}_1)e^{i\gamma\phi}\right]=h_\gamma^{(\mathrm{rot})}(r,\Theta;\boldsymbol{K}_1)e^{-i\gamma\phi} \tag{2.71f}$$

$$P_\theta(\sigma_{z'})P_\phi(\sigma_{z'})\left[h_\gamma^{(\mathrm{rot})}(r,\Theta;\boldsymbol{K}_1)e^{i\gamma\phi}\right]=(-1)^\gamma h_\gamma^{(\mathrm{rot})}(r,\Theta;\boldsymbol{K}_1)e^{i\gamma\phi} \tag{2.71g}$$

$$P_\theta(C_{2x'})P_\phi(C_{2x'})\left[h_\gamma^{(\mathrm{rot})}(r,\Theta;\boldsymbol{K}_1)e^{i\gamma\phi}\right]=(-1)^\gamma h_\gamma^{(\mathrm{rot})}(r,\Theta;\boldsymbol{K}_1)e^{-i\gamma\phi}. \tag{2.71h}$$

Adding up all the rotations as represented by the projection operator $\mathcal{P}^{(rot)}$ we find

$$\begin{aligned}\mathcal{P}^{(\mathrm{rot})}\left[h_\gamma^{(\mathrm{rot})}(r,\Theta;\boldsymbol{K}_1)e^{i\gamma\phi}\right]=&\frac{1}{8}\left\{2h_\gamma^{(\mathrm{rot})}(r,\Theta;\boldsymbol{K}_1)e^{i\gamma\phi}\left[1+(-1)^\gamma\right]\right.\\&\left.+\,2h_\gamma^{(\mathrm{rot})}(r,\Theta;\boldsymbol{K}_1)e^{-i\gamma\phi}\left[1+(-1)^\gamma\right]\right\}\\=&\frac{1+(-1)^\gamma}{2}h_\gamma^{(\mathrm{rot})}(r,\Theta;\boldsymbol{K}_1)\cos(\gamma\phi),\end{aligned} \tag{2.72}$$

and the Fourier component function can be expressed as

$$\begin{aligned}u_{\mathrm{rot}}(\boldsymbol{r}';\boldsymbol{K}_1)=&h_0^{(\mathrm{rot})}(r,\Theta;\boldsymbol{K}_1)\\&+\sum_{\gamma=1}^{\infty}\frac{1+(-1)^\gamma}{2}\left[h_\gamma^{(\mathrm{rot})}(r,\Theta;\boldsymbol{K}_1)+h_{-\gamma}^{(\mathrm{rot})}(r,\Theta;\boldsymbol{K}_1)\right]\cos(\gamma\phi)\\=&h_0^{(\mathrm{rot})}(r,\Theta;\boldsymbol{K}_1)+2\sum_{n=1}^{\infty}\Re\left\{h_{2n}^{(\mathrm{rot})}(r,\Theta;\boldsymbol{K}_1)\right\}\cos(2n\phi).\end{aligned} \tag{2.73}$$

$\boldsymbol{K}$-vector Type	Allowed components of h_γ
$\boldsymbol{K}_1$	Real $\{0, 2n\}$
$\boldsymbol{K}_2$	Real $\{0, 6n\}$, Imag$\{6n-3\}$
$\boldsymbol{K}_3$	Real $\{0, 4n\}$
$\boldsymbol{K}_4$	Real $\{0, 2n\}$, Imag $\{2n-1\}$
$\boldsymbol{K}_5$	Real $\{0, n\}$
$\boldsymbol{K}_6$	Real $\{0, 2n\}$, Imag $\{2n-1\}$
$n \in \mathbb{N}$	

Table 2.2: Selection rules for h_γ.

Equation 2.73 shows that the only contributions to the Fourier functions come from the real parts of $h^{(\mathrm{rot})}$ with γ being any zero or positive even value.

The workings for vectors of type $\boldsymbol{K}_2$ - $\boldsymbol{K}_5$ follow the same approach and are presented in Appendix E, the results of which are presented in Table 2.2. The symmetries of the two-body density are expressed by $h_\gamma^{(\mathrm{rot})}$ having zero real or imaginary parts for different γ. This only occurs because the relevant symmetry operators point along rotated axes, x', y' or z'. Vectors of type $\boldsymbol{K}_6$ are different in that the symmetry operators do not point along rotated axes, the result of which is that all values of γ have both real and imaginary parts, with the exception of $\gamma = 0$ where the symmetry of the two-body density prohibits any imaginary part. It is possible to perform a second rotation such that the symmetry operators do

now point along (doubly) rotated axes. To achieve this we must first establish the orientation of the symmetry rotations in the primed frame given by Eq 2.70. The symmetries of interest are $\{1, 2, 29, 30\}$ or $\{E, I, C'_{2d}, \sigma_{d4}\}$, with C'_{2d} and σ_{d5} having direction $(0, 1, 1)$. Employing Eq. 2.70 we find

$$\boldsymbol{n}' = \begin{pmatrix} \cos(\beta) & \sin(\beta) & 0 \\ -\sin(\beta)\cos(\gamma) & \cos(\beta)\cos(\gamma) & \sin(\gamma) \\ \sin(\beta)\sin(\gamma) & -\cos(\beta)\sin(\gamma) & \cos(\gamma) \end{pmatrix} \cdot \begin{pmatrix} 0 \\ 1 \\ 1 \end{pmatrix} \tag{2.74}$$

$$= \begin{pmatrix} \sin\beta \\ \cos(\beta)\cos(\gamma) + \sin(\gamma) \\ -cos(\beta)\sin(\gamma) + \cos(\gamma) \end{pmatrix}, \tag{2.75}$$

where for a vector of type $\boldsymbol{K}_6 = (j, k, -k)$, $-j < k < 0$, we have

$$\cos(\beta) = \frac{-k}{\sqrt{j^2 + k^2}} \qquad \sin(\beta) = \frac{j}{\sqrt{j^2 + k^2}} \tag{2.76}$$

$$\cos(\gamma) = \frac{-k}{\sqrt{j^2 + 2k^2}} \qquad \sin(\gamma) = \frac{\sqrt{j^2 + k^2}}{\sqrt{j^2 + 2k^2}} \tag{2.77}$$

leading to

$$\boldsymbol{n}' = \begin{pmatrix} \frac{j}{\sqrt{j^2+k^2}} \\ \frac{k^2}{\sqrt{(j^2+k^2)(j^2+2k^2)}} + \frac{\sqrt{j^2+k^2}}{\sqrt{j^2+2k^2}} \\ 0 \end{pmatrix}. \tag{2.78}$$

It is clear from Eq. 2.78 that the direction of the symmetry rotations is within the $x'y'$-plane and as such a rotation about the z'-axis will align $\boldsymbol{n}'$ with an axis. We define a new rotation matrix R' such that we rotate $\boldsymbol{n}'$ to point along the

doubly rotated axis x'' where

$$R' = \begin{pmatrix} \cos(\alpha) & -\sin(\alpha) & 0 \\ \sin(\alpha) & \cos(\alpha) & 0 \\ 0 & 0 & 1 \end{pmatrix} \tag{2.79}$$

with

$$\cos(\alpha) = \frac{-n'_x}{\sqrt{n'^2_x + n'^2_y}}, \qquad \sin(\alpha) = \frac{n'_y}{\sqrt{n'^2_x + n'^2_y}}. \tag{2.80}$$

The final direction of the rotations is therefore

$$\boldsymbol{n}'' = (R'R_0(\boldsymbol{K}_6))^T \boldsymbol{n} = R'R_0(\boldsymbol{K}_6)^T \boldsymbol{n} = R'\boldsymbol{n}' = \begin{pmatrix} -\sqrt{n'^2_x + n'^2_y} \\ 0 \\ 0 \end{pmatrix}, \tag{2.81}$$

and the symmetry operators in the new double primed frame are $\{E, I, C_{2x''}, \sigma_{x''}\}$. The orientation of the symmetry operators is the same as those for vectors of type $\boldsymbol{K}_4$ and thus vectors of type $\boldsymbol{K}_6$ will, in their respective double primed frames of reference, follow the same rules as type $\boldsymbol{K}_4$.

2.3 Path Integral Formulation

The foundation of path integral Monte Carlo (PIMC) methods is the convolution property of the unnormalised density matrix $\mathcal{W}(\boldsymbol{R}, \boldsymbol{R}'; \beta) = Z(\beta)W(\boldsymbol{R}, \boldsymbol{R}'; \beta)$

$$\mathcal{W}(\boldsymbol{R}, \boldsymbol{R}'; \beta) = \int \mathcal{W}(\boldsymbol{R}, \boldsymbol{R}_1; (1-q)\beta)\mathcal{W}(\boldsymbol{R}_1, \boldsymbol{R}'; q\beta)d\boldsymbol{R}_1 \tag{2.82}$$

with $0 < q < 1$. By applying the property M_W times it is possible to obtain the unnormalised density matrix for a temperature T at a higher temperature $(M_W + 1)T$ at the expense of a $3NM_W$-dimensional integral,

$$\mathcal{W}(\boldsymbol{R}, \boldsymbol{R}'; \beta) = \int \prod_{v=0}^{M_W} \mathcal{W}\left(\boldsymbol{R}_v, \boldsymbol{R}_{v+1}; \frac{\beta}{M_W + 1}\right) d\boldsymbol{R}_1 \ldots d\boldsymbol{R}_{M_W}. \tag{2.83}$$

The key to continuous imaginary time PIMC methods is to increase the effective temperature $(M_W + 1)T$ to one where the exact analytical form of the matrix elements in the high-temperature limit can be used. The unnormalised density matrix in the high-temperature limit is given by [16]

$$\begin{aligned}\mathcal{W}\left(\boldsymbol{R}_v, \boldsymbol{R}_{v+1}; \frac{\beta}{M_W + 1}\right) = \\ \left(\frac{m(M_W + 1)}{2\pi\beta\hbar^2}\right)^{3N/2} \exp\left\{-\frac{m(M_W + 1)}{2\beta\hbar^2}(\boldsymbol{R}_{v+1} - \boldsymbol{R}_v)^2\right. \\ \left. -\frac{\beta}{2(M_W + 1)}\left[V(\boldsymbol{R}_v) + V(\boldsymbol{R}_{v+1})\right]\right\}.\end{aligned} \tag{2.84}$$

Inserting Eq. 2.84 into Eq. 2.83 leads to

$$\begin{aligned}W(\boldsymbol{R}, \boldsymbol{R}'; \beta) &= \frac{1}{\mathcal{I}(\beta)} \int \prod_{v=1}^{M_W} d\boldsymbol{R}_v \exp\left\{-\frac{m}{2\beta\hbar^2}\left[\Delta_W \sum_{v=0}^{M_W}\left(\frac{\boldsymbol{R}_{v+1} - \boldsymbol{R}_v}{\Delta_W}\right)^2\right]\right. \\ &\left. -\beta\Delta_W\left[\frac{1}{2}V(\boldsymbol{R}) + \sum_{v=1}^{M_W} V(\boldsymbol{R}_v) + \frac{1}{2}V(\boldsymbol{R}')\right]\right\},\end{aligned} \tag{2.85}$$

where $\Delta_W = 1/(M_W + 1)$ and $\mathcal{I}(\beta)$ is the normalisation integral. Taking $M_W \to \infty$ the sums in Eq. 2.85 can be rewritten as integrals along the path from $\boldsymbol{R}$ to $\boldsymbol{R}'$

$$\Delta_W \sum_{v=0}^{M_W}\left(\frac{\boldsymbol{R}_{v+1} - \boldsymbol{R}_v}{\Delta_W}\right)^2 \to \int_0^1 \dot{\boldsymbol{R}}_P^2(\eta) d\eta, \tag{2.86}$$

$$\Delta_W\left[\frac{1}{2}V(\boldsymbol{R}) + \sum_{v=1}^{M_W} V(\boldsymbol{R}_v) + \frac{1}{2}V(\boldsymbol{R}')\right] \to \int_0^1 V(\boldsymbol{R}_P(\eta)) d\eta. \tag{2.87}$$

In Eqs 2.86 and 2.87 the continuous imaginary time η assumes all values between zero and one. The end points for the integrals are $\boldsymbol{R}_P(0) = \boldsymbol{R}$ and $\boldsymbol{R}_P(1) = \boldsymbol{R}'$. The notation $\dot{\boldsymbol{R}}_P(\eta)$ in Eq. 2.86 defines the derivative of the $3N$-dimensional path, $\dot{\boldsymbol{R}}_P(\eta) = d\boldsymbol{R}_P(\eta)/d\eta$.

Expressing the paths $\boldsymbol{R}_P(\eta)$ as a Fourier series

$$\boldsymbol{R}_P(\eta; \boldsymbol{A}) = \boldsymbol{R} + (\boldsymbol{R}' - \boldsymbol{R})\eta + \sum_{l=1}^{\infty} \boldsymbol{a}_l \sin(l\pi\eta) \tag{2.88}$$

enables us to perform the integration in Eq. 2.86. In Eq. 2.88 $\boldsymbol{A}$ represents all of the $3N$-dimensional vectors $\boldsymbol{a}_l$. Combining Eqs. 2.85, 2.86, 2.87 and 2.88 we obtain

$$\begin{aligned} W(\boldsymbol{R}, \boldsymbol{R}'; \beta) &= \frac{1}{\mathcal{I}(\beta)} \exp\left\{-\frac{m}{2\beta\hbar^2}(\boldsymbol{R}' - \boldsymbol{R})^2\right\} \\ &\times \int \exp\left\{-\sum_{l=1}^{\infty}\left(\frac{\boldsymbol{a}_l}{\sqrt{2}\sigma_l}\right)^2 - \beta\mathcal{V}(\boldsymbol{R}, \boldsymbol{R}'; \boldsymbol{A})\right\} \prod_{l=1}^{\infty} d\boldsymbol{a}_l, \end{aligned} \tag{2.89}$$

where

$$\mathcal{V}(\boldsymbol{R}, \boldsymbol{R}'; \boldsymbol{A}) = \int_0^1 V(\boldsymbol{R}_P(\eta; \boldsymbol{A}))d\eta \tag{2.90}$$

and

$$\sigma_l = \frac{1}{l\pi}\left(\frac{2\beta\hbar^2}{m}\right)^{1/2}. \tag{2.91}$$

2.4 Numerical Computation of Quantum Thermodynamic Estimators

In Sections 2.1 and 2.3 we outlined the theory behind the calculation, by means of a Fourier Path Integral formalism, of various thermodynamic properties for a system of N identical particles. In this section we aim to discuss the implementation of this approach with regard to our computational simulations.

The most straightforward of our estimators is that of the potential energy. Recalling Eq. 2.8 and inserting the result from Eq. 2.89 we obtain

$$E_{\text{pot}} = \int V(\boldsymbol{R}) W(\boldsymbol{R}, \boldsymbol{R}; \beta) d\boldsymbol{R} = \frac{1}{\mathcal{I}(\beta)} \int V(\boldsymbol{R}) \Xi(\boldsymbol{R}; \boldsymbol{A}_L) \prod_{l=1}^{L} d\boldsymbol{a}_l d\boldsymbol{R} \quad (2.92)$$

where

$$\Xi(\boldsymbol{R}; \boldsymbol{A}_L) = \exp\left\{ -\sum_{l=1}^{L} \left(\frac{\boldsymbol{a}_l}{\sqrt{2}\sigma_l} \right)^2 - \beta \mathcal{V}(\boldsymbol{R}, \boldsymbol{R}; \boldsymbol{A}_L) \right\}, \quad (2.93)$$

and where we have truncated the infinite series at an upper limit L. The totality of the $3N$-dimensional vectors $\boldsymbol{a}_l$ in the truncated expression are denoted by the symbol $\boldsymbol{A}_L$ where $1 \leq l \leq L$. The truncation to L is required to avoid infinite series. A partial averaging approach to take into account the higher Fourier coefficients $l > L$ is discussed in Ref. [16], however such corrections are found to be small for the systems of interest here and can thus be neglected. In addition we add a tail correction to take account of contributions to the total potential energy for $r > r_{\text{limit}}$. In this work r_{limit} is an upper cutoff to the relative distance such that the system remains isotropic under periodic boundary conditions. Further

details can be found in Appendix B. The tail correction takes the form [16]

$$\frac{E_{\text{tail}}}{N} = 2\pi\rho_0 \int_{r_{\text{limit}}}^{\infty} r^2 \upsilon(r) dr. \tag{2.94}$$

The estimator for the kinetic energy is more complicated. Full details are given in Appendix A and the result is given below;

$$\begin{aligned} E_{\text{kin}} &= N\frac{3}{2}k_B T \\ &+\frac{\hbar^2\beta}{2m}\left\{\frac{1}{\mathcal{I}(\beta)}\left\langle\int_0^1 d\eta(1-\eta)^2\sum_{i,j=1}^{N}(1-\delta_{ij})\upsilon_{gg}\left(r_{P,ij}^{[c]}(\eta;\boldsymbol{A}_L)\right)\right\rangle_{\Xi}\right. \\ &-\beta\frac{1}{\mathcal{I}(\beta)}\left\langle\sum_{j=1}^{N}\left[\int_0^1 d\eta(1-\eta)\sum_{i=1}^{N}(1-\delta_{ij})\frac{\boldsymbol{r}_{P,ij}^{[c]}(\eta;\boldsymbol{A}_L)}{r_{P,ij}^{[c]}(\eta;\boldsymbol{A}_L)}\right.\right. \\ &\left.\left.\left.\times\upsilon'\left(r_{P,ij}^{[c]}(\eta;\boldsymbol{A}_L)\right)\right]^2\right\rangle_{\Xi}\right\}, \end{aligned} \tag{2.95}$$

where the use of Dirac brackets $\langle\ldots\rangle_{\Xi}$ is employed to denote the average w.r.t. Ξ. The normalisation integral is given by

$$\mathcal{I}(\beta) = \int \exp\left\{-\beta\mathcal{V}(\boldsymbol{R},\boldsymbol{R};\boldsymbol{A}_L)\right\}\prod_{l=1}^{L}\exp\left\{-\left(\frac{\boldsymbol{a}_l}{\sqrt{2}\sigma_l}\right)^2\right\}d\boldsymbol{a}_l d\boldsymbol{R}, \tag{2.96}$$

where

$$\mathcal{V}(\boldsymbol{R},\boldsymbol{R};\boldsymbol{A}_L) = \int_0^1 V(\boldsymbol{R}_P^{[c]}(\eta;\boldsymbol{A}_L))d\eta \tag{2.97}$$

is the same as in Eq. 2.90 except that we now take the closed path

$$\boldsymbol{R}_P^{[c]}(\eta;\boldsymbol{A}_L) = \boldsymbol{R} + \sum_{l=1}^{L}\boldsymbol{a}_l\sin(l\pi\eta). \tag{2.98}$$

In this present work we split the kinetic energy into three terms,

$$E_{\text{kin}} = E_{\text{free}} + E_2 + E_3, \tag{2.99}$$

where

$$E_{\text{free}} = N\frac{3}{2}k_BT \tag{2.100}$$

$$E_2 = \frac{\hbar^2\beta}{2m}\frac{1}{\mathcal{I}(\beta)}\left\langle \int_0^1 d\eta(1-\eta)^2 \sum_{i,j=1}^{N}(1-\delta_{ij})v_{gg}\left(r_{P,ij}^{[c]}(\eta;\boldsymbol{A}_L)\right)\right\rangle_{\Xi} \tag{2.101}$$

$$E_3 = -\frac{\hbar^2\beta^2}{2m}\frac{1}{\mathcal{I}(\beta)} \times \left\langle \sum_{j=1}^{N}\left[\int_0^1 d\eta(1-\eta)\sum_{i=1}^{N}(1-\delta_{ij})\frac{\boldsymbol{r}_{P,ij}^{[c]}(\eta;\boldsymbol{A}_L)}{r_{P,ij}^{[c]}(\eta;\boldsymbol{A}_L)}v'\left(r_{P,ij}^{[c]}(\eta;\boldsymbol{A}_L)\right)\right]^2\right\rangle_{\Xi}. \tag{2.102}$$

E_{free} is the classical Boltzmann free energy for a system of N particles with three degrees of freedom. E_2 and E_3 are the two- and formally three-body contributions to the kinetic energy. The three-body contributions can be further broken down,

$$E_3 = E_{3a} + E_{3b}, \tag{2.103}$$

where

$$E_{3a} = -\frac{\hbar^2\beta^2}{2m}\frac{1}{\mathcal{I}(\beta)} \times \left\langle \sum_{i,j=1}^{N}(1-\delta_{ij})\left[\int_0^1 d\eta(1-\eta)\frac{\boldsymbol{r}_{P,ij}^{[c]}(\eta;\boldsymbol{A}_L)}{r_{P,ij}^{[c]}(\eta;\boldsymbol{A}_L)}v'\left(r_{P,ij}^{[c]}(\eta;\boldsymbol{A}_L)\right)\right]^2\right\rangle_{\Xi} \tag{2.104}$$

contains the three-body terms which are reducible to two-body terms. Conversely

$$\begin{aligned} E_{3b} = & -\frac{\hbar^2\beta^2}{2m}\frac{1}{\mathcal{I}(\beta)}\left\langle \sum_{i,j,k=1}^{N}(1-\delta_{ij})(1-\delta_{kj})(1-\delta_{ik})\right. \\ & \cdot\left\{\int_0^1 d\eta(1-\eta)\frac{\boldsymbol{r}_{P,ij}^{[c]}(\eta;\boldsymbol{A}_L)}{r_{P,ij}^{[c]}(\eta;\boldsymbol{A}_L)}v'\left(r_{P,ij}^{[c]}(\eta;\boldsymbol{A}_L)\right)\right\} \\ & \left.\cdot\left\{\int_0^1 d\eta(1-\eta)\frac{\boldsymbol{r}_{P,kj}^{[c]}(\eta;\boldsymbol{A}_L)}{r_{P,kj}^{[c]}(\eta;\boldsymbol{A}_L)}v'\left(r_{P,kj}^{[c]}(\eta;\boldsymbol{A}_L)\right)\right\}\right\rangle_{\Xi} \end{aligned} \tag{2.105}$$

contains the irreducible three-body terms.

The averages $\langle \ldots \rangle_\Xi$ represent $\mathrm{Tr}\left\{\hat{Q}\hat{W}(\beta)\right\}$ where Q is a property described by the quantum-mechanical operator $\hat{Q}$. Such averages may be calculated via the Metropolis algorithm by means of

$$\tilde{Q} = \sum_{\text{all configurations}} \left[PQ^{\text{new}} + (1-P)Q^{\text{old}}\right], \tag{2.106}$$

where $P = \min(1, \mathcal{P})$, $\mathcal{P}$ being the associated probability of moving from an old configuration to a new configuration and Q^{new} and Q^{old} are the values of property Q in the new and old configurations respectively. A configuration is determined by both the positions of the particles and the relevant paths. The value $\tilde{Q}$ must be normalised by N_{config}, the number of configurations visited during a simulation, i.e. $Q = \tilde{Q}/N_{\text{config}}$ where Q is the normalised property and $N_{\text{config}} = N_P * N_{\text{steps}} * N_{\text{blocks}}$, with N_P, N_{steps} and N_{blocks} being the total number of particles, steps and blocks respectively. The meaning of the terms step and block is discussed in Section 2.6.1.

In a conventional Monte Carlo simulation a proposed move of a particle, k, and its associated path defined by the Fourier coefficients $\boldsymbol{a}_{l,k}$, would be assigned the probability

$$\mathcal{P} = \frac{\Xi^{\text{new}}}{\Xi^{\text{old}}} = \frac{\exp\left\{-\sum_{l=1}^{L}\left(\frac{a_{l,k}^{\text{new}}}{\sqrt{2}\sigma_l}\right)^2 - \beta\mathcal{V}(\boldsymbol{R}^{\text{new}}, \boldsymbol{R}^{\text{new}}; \boldsymbol{A}_L^{\text{new}})\right\}}{\exp\left\{-\sum_{l=1}^{L}\left(\frac{a_{l,k}^{\text{old}}}{\sqrt{2}\sigma_l}\right)^2 - \beta\mathcal{V}(\boldsymbol{R}^{\text{old}}, \boldsymbol{R}^{\text{old}}; \boldsymbol{A}_L^{\text{old}})\right\}}, \tag{2.107}$$

where $a_{l,k}$ is the l^{th} 3-dimensional Fourier coefficient of particle k. However by

sampling the new paths for a particle k from Gaussians of the form $\exp\left\{-[\boldsymbol{a}_{l,k}^{(\mathrm{new})}/(\sqrt{2}\sigma_l)]^2\right\}$, and by moving particle k such that $\boldsymbol{r}_k^{\mathrm{new}} = \boldsymbol{r}_k^{\mathrm{old}} + (\Delta_x, \Delta_y, \Delta_z)\delta_{\mathrm{MC}}$, where δ_{MC} is the move size, and $\Delta_x, \Delta_y, \Delta_z$ are random numbers drawn from a uniform distribution, $-0.5 \leq \Delta \leq 0.5$, the probability of a move becomes

$$\mathcal{P} = \frac{\exp\left\{-\beta\mathcal{V}(\boldsymbol{R}^{\mathrm{new}}, \boldsymbol{R}^{\mathrm{new}}; \boldsymbol{A}_L^{\mathrm{new}})\right\}}{\exp\left\{-\beta\mathcal{V}(\boldsymbol{R}^{\mathrm{old}}, \boldsymbol{R}^{\mathrm{old}}; \boldsymbol{A}_L^{\mathrm{old}})\right\}}. \tag{2.108}$$

2.5 Classical Monte Carlo Calculations

The derivation of classical estimators for the thermodynamic properties of interest can be achieved either by taking a purely classical approach or by taking the semiclassical limit of the quantum estimators previously derived in Section 2.4. For clarity and rigour we shall take the former approach and subsequently compare our findings with the semiclassical limit of the FPIMC estimators.

The equilibrium value, $\bar{P}$, of a quantity, P, in the classical canonical ensemble is given by [28], [1],

$$\bar{P} = \frac{\int P \exp\left(-V(\boldsymbol{R})/kT\right) d\boldsymbol{R}}{\int \exp\left(-V(\boldsymbol{R})/kT\right) d\boldsymbol{R}}, \tag{2.109}$$

where $V(\boldsymbol{R})$ is the potential energy of the system as given in Eq. 2.3. Replacing P in Eq. 2.109 by the potential energy $V(\boldsymbol{R})$ we obtain

$$E_{\mathrm{pot}} = \frac{\int V(\boldsymbol{R}) \exp\left(-V(\boldsymbol{R})/kT\right) d\boldsymbol{R}}{\int \exp\left(-V(\boldsymbol{R})/kT\right) d\boldsymbol{R}}. \tag{2.110}$$

Comparing Eq. 2.110 with its quantum counterpart 2.92, reproduced below,

$$E_{\text{pot}} = \frac{1}{\mathcal{I}(\beta)} \int V(\boldsymbol{R}) \Xi(\boldsymbol{R}; \boldsymbol{A}_L) \prod_{l=1}^{L} d\boldsymbol{a}_l d\boldsymbol{R}, \tag{2.92}$$

$$\Xi(\boldsymbol{R}; \boldsymbol{A}_L) = \exp\left\{ -\sum_{l=1}^{L} \left(\frac{\boldsymbol{a}_l}{\sqrt{2}\sigma_l} \right)^2 - \beta \mathcal{V}(\boldsymbol{R}, \boldsymbol{R}; \boldsymbol{A}_L) \right\}, \tag{2.93}$$

we see that ignoring the normalisation integrals the quantum result reduces to the classical one for $L = 0$. This result should not surprise us since setting $L = 0$ removes all paths and we return to point particles. As in the quantum case a tail correction of the form

$$\frac{E_{\text{tail}}}{N} = 2\pi\rho_0 \int_{r_{\text{limit}}}^{\infty} r^2 v(r) dr \tag{2.94}$$

is added to the potential energy.

Classically the kinetic energy for N particles simply reads

$$E_{\text{kin}} = \frac{3}{2} N k_B T, \tag{2.111}$$

which is the Boltzmann energy for $3N$ degrees of freedom. Obviously this is very different from the kinetic energy estimator from the quantum case Eq. 2.95

$$\begin{aligned} E_{\text{kin}} =& N\frac{3}{2}k_B T \\ &+ \frac{\hbar^2\beta}{2m} \left\{ \frac{1}{\mathcal{I}(\beta)} \left\langle \int_0^1 d\eta (1-\eta)^2 \sum_{i,j=1}^{N} (1-\delta_{ij}) v_{gg}\left(r_{P,ij}^{[c]}(\eta; \boldsymbol{A}_L) \right) \right\rangle_{\Xi} \right. \\ &- \beta \frac{1}{\mathcal{I}(\beta)} \left\langle \sum_{j=1}^{N} \left[\int_0^1 d\eta (1-\eta) \sum_{i=1}^{N} (1-\delta_{ij}) \frac{\boldsymbol{r}_{P,ij}^{[c]}(\eta; \boldsymbol{A}_L)}{r_{P,ij}^{[c]}(\eta; \boldsymbol{A}_L)} \right. \right. \\ &\left. \left. \times v'\left(r_{P,ij}^{[c]}(\eta; \boldsymbol{A}_L) \right) \right]^2 \right\rangle_{\Xi} \Bigg\}. \end{aligned} \tag{2.112}$$

Taking the semiclassical limit of the quantum estimator by setting $L = 0$ to remove all paths yields

$$E_{\text{kin}} = N\frac{3}{2}k_BT + \frac{\hbar^2\beta}{2m}\left\{\frac{1}{\mathcal{I}(\beta)}\left\langle\int_0^1 d\eta(1-\eta)^2\sum_{i,j=1}^{N}(1-\delta_{ij})v_{gg}(r_{ij})\right\rangle_{\Xi_c}\right.$$
$$\left.-\beta\frac{1}{\mathcal{I}(\beta)}\left\langle\sum_{j=1}^{N}\left[\int_0^1 d\eta(1-\eta)\sum_{i=1}^{N}(1-\delta_{ij})\frac{\boldsymbol{r}_{ij}}{r_{ij}}v'(r_{ij})\right]^2\right\rangle_{\Xi_c}\right\}, \quad (2.113)$$

where we have again used Dirac brackets $\langle\ldots\rangle_{\Xi_c}$ to express the average w.r.t. Ξ_c with

$$\Xi_c(\boldsymbol{R}) = \exp\left\{-\beta V(\boldsymbol{R})\right\}. \quad (2.114)$$

The integrals over η can be performed explicitly as there are now no paths

$$\int_0^1 d\eta(1-\eta) = \frac{1}{2}, \quad (2.115)$$
$$\int_0^1 d\eta(1-\eta)^2 = \frac{1}{3}. \quad (2.116)$$

The resulting semiclassical limit of the quantum kinetic energy estimator reads

$$E_{\text{kin}} = N\frac{3}{2}k_BT + \frac{\hbar^2\beta}{6m}\frac{1}{\mathcal{I}(\beta)}\left\langle\sum_{i,j=1}^{N}(1-\delta_{ij})v_{gg}(r_{ij})\right\rangle_{\Xi_c}$$
$$-\frac{\hbar^2\beta^2}{8m}\frac{1}{\mathcal{I}(\beta)}\left\langle\sum_{j=1}^{N}\left[\sum_{i=1}^{N}(1-\delta_{ij})\frac{\boldsymbol{r}_{ij}}{r_{ij}}v'(r_{ij})\right]^2\right\rangle_{\Xi_c}. \quad (2.117)$$

We recall our earlier definitions of E_2 and E_3 being the two- and three- body

contributions to the kinetic energy which now become

$$\begin{aligned} E_2 &= \frac{\hbar^2\beta}{6m}\frac{1}{\mathcal{I}(\beta)}\left\langle \sum_{i,j=1}^{N}(1-\delta_{ij})v_{gg}(r_{ij})\right\rangle_{\Xi_c}, \\ &= \frac{\hbar^2\beta}{6m}\frac{1}{\mathcal{I}(\beta)}\left\langle \nabla^2 V(\boldsymbol{R})\right\rangle_{\Xi_c}, \qquad (2.118) \\ E_3 &= -\frac{\hbar^2\beta^2}{8m}\frac{1}{\mathcal{I}(\beta)}\left\langle \sum_{j=1}^{N}\left[\sum_{i=1}^{N}(1-\delta_{ij})\frac{\boldsymbol{r}_{ij}}{r_{ij}}v'(r_{ij})\right]^2\right\rangle_{\Xi_c} \\ &= -\frac{\hbar^2\beta^2}{8m}\frac{1}{\mathcal{I}(\beta)}\left\langle [\nabla V(\boldsymbol{R})]^2\right\rangle_{\Xi_c}. \qquad (2.119) \end{aligned}$$

The quantities in Dirac brackets in Eqs. 2.118 and 2.119 are related to each other. Writing the Dirac brackets out in their integral form we see that

$$\begin{aligned} \int \left[\nabla^2 V(\boldsymbol{R})\right]\exp\left(-\beta V(\boldsymbol{R})\right)d\boldsymbol{R} &= -\int \left[\nabla V(\boldsymbol{R})\right]\nabla\left[\exp\left(-\beta V(\boldsymbol{R})\right)\right]d\boldsymbol{R} \\ &= +\beta\int \left[\nabla V(\boldsymbol{R})\right]^2\exp\left(-\beta V(\boldsymbol{R})\right)d\boldsymbol{R}. \end{aligned} \qquad (2.120)$$

Thus in the semiclassical limit we find that E_2 and E_3 are related to each other via,

$$E_3 = -\frac{\hbar^2\beta}{8m}\frac{1}{\mathcal{I}(\beta)}\left\langle \sum_{i,j=1}^{N}(1-\delta_{ij})v_{gg}(r_{ij})\right\rangle_{\Xi_c} = -\frac{3}{4}E_2. \qquad (2.121)$$

Gathering all terms together we can see that the simplest form for the kinetic energy in the semiclassical limit is

$$E_{\text{kin}} = N\frac{3}{2}k_BT + \frac{\hbar^2\beta}{24m}\frac{1}{\mathcal{I}(\beta)}\left\langle \sum_{i,j=1}^{N}(1-\delta_{ij})v_{gg}(r_{ij})\right\rangle_{\Xi_c}, \qquad (2.122)$$

where the second term can be viewed as a quantum correction to the kinetic energy of classical simulations. In our analysis of the quantum kinetic energy

we split the three-body contribution into two parts $E_3 = E_{3a} + E_{3b}$, where E_{3a} contained those three-body terms that could be expressed as two-body terms and E_{3b} contained those terms that were not reducible to two-body terms. Applying the semiclassical limit to E_{3a} and E_{3b} we find,

$$E_{3a} = -\frac{\hbar^2\beta^2}{8m}\left\langle \sum_{i,j=1}^{N}(1-\delta_{ij})\frac{\boldsymbol{r}_{ij}}{r_{ij}}[v'(r_{ij})]^2 \right\rangle_{\Xi_c} \tag{2.123}$$

$$E_{3b} = -\frac{\hbar^2\beta^2}{8m}\left\langle \sum_{i,j=1}^{N}(1-\delta_{ij})(1-\delta_{kj})(1-\delta_{ik})\frac{\boldsymbol{r}_{ij}}{r_{ij}}\frac{\boldsymbol{r}_{kj}}{r_{kj}}v'(r_{ij})v'(r_{kj}) \right\rangle_{\Xi_c} \tag{2.124}$$

It is interesting to note that in the semiclassical limit E_{3b} can be reduced to two-body terms only

$$E_{3b} = E_3 - E_{3a} = -\frac{3}{4}E_2 - E_{3a}. \tag{2.125}$$

This is a direct result of the averages being w.r.t. the classical Boltzmann distribution $e^{-\beta V(\boldsymbol{R})}$.

As with the FPIMC simulations a new configuration is chosen by moving particle k by means of

$$\boldsymbol{r}_k^{\text{new}} = \boldsymbol{r}_k^{\text{old}} + (\Delta_x, \Delta_y, \Delta_z)\delta_{\text{MC}}, \tag{2.126}$$

where δ_{MC} is the move size, and $\Delta_x, \Delta_y, \Delta_z$ are random numbers drawn from a uniform distribution on $-0.5 \leq \Delta \leq 0.5$. The use of random numbers in a computer simulation requires careful consideration, to ensure that such numbers are statistically random. A detailed discussion of the implementation of random number generators is given in Appendix C.

2.6 Simulation Procedures

Here we shall outline the general schematics for performing a simulation, be it classical Monte Carlo or FPIMC. We will make clear any differences between the two simulation procedures as they arise.

2.6.1 Simulation Overview

A new configuration is sampled from the perfect crystal using the procedures outlined in Sections 2.4 and 2.5. We define an attempt to successively move all particles once as a step and a block as 100 steps. To remove all traces of the initial perfect crystal we simulate for 100 blocks and discard all statistics generated during this time. For simulations of solids this should be sufficient but for simulations of liquids it is prudent to check for contributions to the transform of the one-body density for $\boldsymbol{K} \neq 0$, and simulate longer if required before gathering any statistics. The final step in any Monte Carlo simulation is to normalise all the calculated quantities by the relevant normalisation factor and multiply in any prefactors that have been omitted for simplicity.

It is usual to start a Monte Carlo simulation from a perfect crystal structure, although the initial configuration for a liquid simulation is irrelevant so long as all traces of the initial lattice have disappeared before any statistics are counted. A lattice is deemed to have melted if there is no contribution to the Fourier transform of the one-body density $\rho(\boldsymbol{K})$ except from $\boldsymbol{K} = 0$, since we recall that

from Eq. 2.44 $\rho(\boldsymbol{K} = 0)$ gives the bulk particle density. Simulations of solids are performed on a face-centred cubic lattice (FCC), the details of which follow. For the FPIMC we must also initialise the paths. This is done by setting all $\boldsymbol{a}_l$ to zero.

2.6.2 Discretised Potentials

To reduce computational load a discretised form of the potential and its derivatives is used. The potential is initially calculated for a grid of 2881 points between 0 and r_{limit}. Calculations of energy terms are performed only up to a cutoff distance r_{limit} which is the radius of the largest sphere that fits inside the simulation cell. This is required so that the potential between two particles is a function only of distance. A full derivation of r_{limit} is given in Appendix B. The potential for a general distance r lying between discrete points n and $n+1$ is given by

$$v(r) = v(n) + \left(\frac{v(n+1) - v(n)}{dr}\right)\Delta r \tag{2.127}$$

where $dr = r_{limit}/2880$, $n = int(r/dr) + 1$ and $\Delta r = r - ((n-1)dr)$. The same approach is used for both the first and second derivatives of the potential.

2.6.3 Maximum Move Size

The value of Δ_{move} strongly affects the rate at which the configuration space is sampled. Smaller values lead to moves being accepted more readily but the space is explored slowly. Conversely large values lead to low acceptance but successful

moves are of a greater distance. A naive compromise is to adjust Δ_{move} prior to gathering statistics such that the acceptance ratio tends to 50%. However it has been suggested [26] that a lower acceptance ratio be chosen in FPIMC simulations. We have found this to be the case especially for the melting of low temperature helium where after 100000 steps we still had traces of the initial lattice for $\Delta_{\text{move}} = 0.03$, whereas the lattice was completely melted after 20000 steps with $\Delta_{\text{move}} = 0.4$.

2.7 The Face-Centred Cubic Lattice

2.7.1 Defining the Lattice and Reciprocal Lattice

The basis vectors of the primitive cell of the FCC lattice are

$$\boldsymbol{a}_1 = \frac{a}{2}(1, -1, 0), \tag{2.128a}$$

$$\boldsymbol{a}_2 = \frac{a}{2}(1, 0, 1), \tag{2.128b}$$

$$\boldsymbol{a}_3 = \frac{a}{2}(0, -1, 1), \tag{2.128c}$$

and are shown in Fig. 2.2, where a^3 is the volume of the conventional cell and $a^3 = 4/\rho$, where ρ is the number density of the system being simulated. The Bravais lattice vectors $\boldsymbol{t}$ are therefore given by

$$\boldsymbol{t} = k_1\boldsymbol{a}_1 + k_2\boldsymbol{a}_2 + k_3\boldsymbol{a}_3, \tag{2.129}$$

$$= \frac{a}{2}(k_1 + k_2, -k_1 - k_3, k_2 + k_3), \qquad k_1, k_2, k_3 \in \mathbb{Z}_0. \tag{2.130}$$

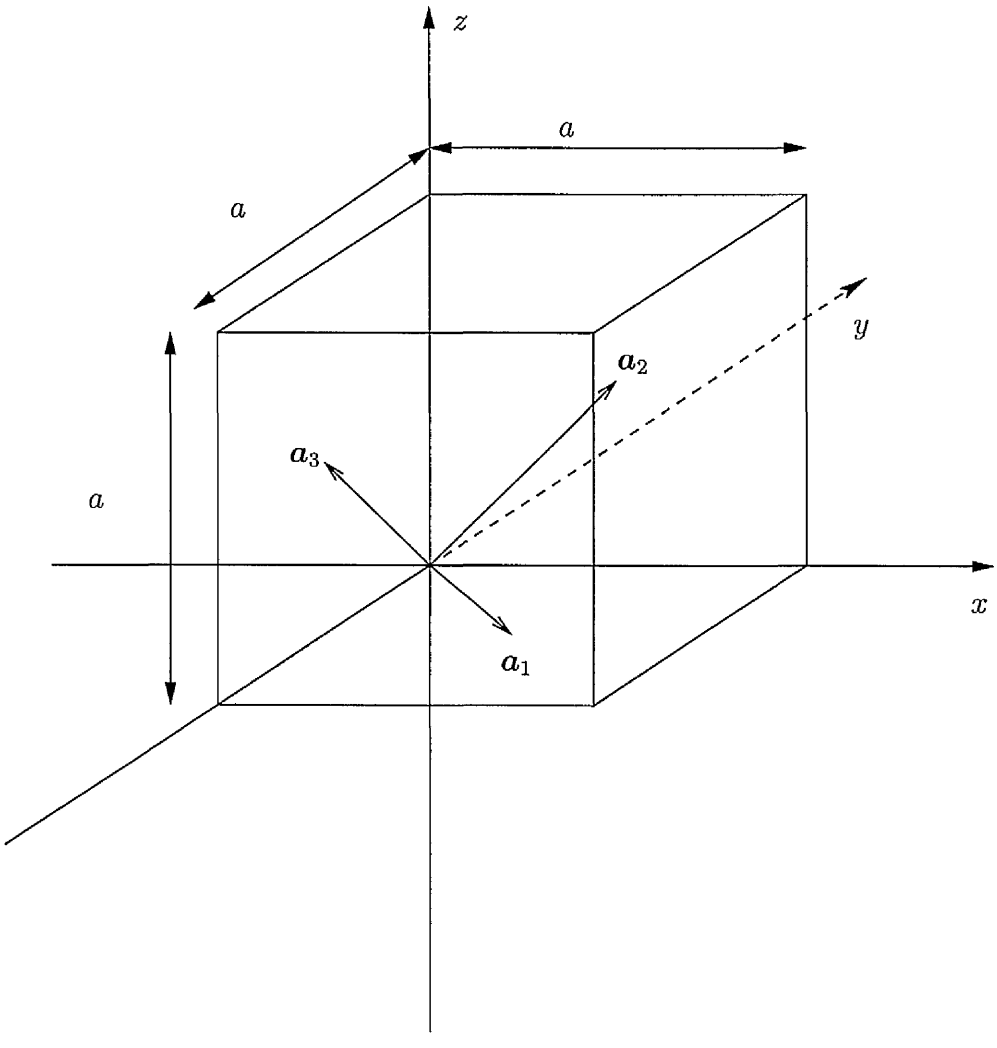

Figure 2.2: Basis vectors of FCC structure.

It is a requirement of the two-body density calculations that an inversion centre is present at the origin. To achieve this a particle is placed at the centre of the primitive cell which is repeated symmetrically about the origin. Thus the initial configuration $\boldsymbol{R}$ is written as

$$\boldsymbol{R} = \left(n_1 + \frac{1}{2}\right)\boldsymbol{a}_1 + \left(n_2 + \frac{1}{2}\right)\boldsymbol{a}_2 + \left(n_3 + \frac{1}{2}\right)\boldsymbol{a}_3, \tag{2.131}$$

where n_1, n_2, n_3 are integers and $-L \leq n_1, n_2, n_3 < L$. The total number of particles, N, is given by $N = (2L)^3$.

The basis vectors of the reciprocal lattice are given by

$$\boldsymbol{b}_1 = \frac{2\pi}{\Omega}\boldsymbol{a}_2 \times \boldsymbol{a}_3 = \frac{2\pi}{a^3/4}\frac{a^2}{4}(1,-1,-1) = \frac{2\pi}{a}(1,-1,-1), \tag{2.132a}$$

$$\boldsymbol{b}_2 = \frac{2\pi}{\Omega}\boldsymbol{a}_3 \times \boldsymbol{a}_1 = \frac{2\pi}{a^3/4}\frac{a^2}{4}(1,1,1) = \frac{2\pi}{a}(1,1,1), \tag{2.132b}$$

$$\boldsymbol{b}_3 = \frac{2\pi}{\Omega}\boldsymbol{a}_1 \times \boldsymbol{a}_2 = \frac{2\pi}{a^3/4}\frac{a^2}{4}(-1,-1,1) = \frac{2\pi}{a}(-1,-1,1). \tag{2.132c}$$

A general reciprocal lattice vector may therefore be expressed as

$$\boldsymbol{K} = k_1\boldsymbol{b}_1 + k_2\boldsymbol{b}_2 + k_3\boldsymbol{b}_3, \tag{2.133}$$

$$= \frac{2\pi}{a}(k_1 + k_2 - k_3, -k_1 + k_2 - k_3, -k_1 + k_2 + k_3), \tag{2.134}$$

$$= \frac{2\pi}{a}(j,k,l), \quad k_1, k_2, k_3 \in \mathbb{Z}_0, \tag{2.135}$$

where j, k, l, are integers given by

$$j = k_1 + k_2 - k_3, \tag{2.136a}$$

$$k = -k_1 + k_2 - k_3, \tag{2.136b}$$

$$l = -k_1 + k_2 + k_3, \tag{2.136c}$$

from which we can derive the following relations

$$j - k = 2k_1, \tag{2.137a}$$

$$j + l = 2k_2, \tag{2.137b}$$

$$l - k = 2k_3. \tag{2.137c}$$

2.7.2 Derivation of the Asymmetric Unit

The choice of asymmetric unit is not unique and the derivations of the one- and two-body densities in their symmeterized forms are not affected by the choice of asymmetric unit. We define the asymmetric unit within the bounds of the conventional unit cell as the volume in $\boldsymbol{K}$-space enclosed by three high-symmetry vectors, $\boldsymbol{K}_1, \boldsymbol{K}_2,$ and $\boldsymbol{K}_3$, with

$$\boldsymbol{K}_1 = \frac{2\pi}{a}(1, -1, 0), \tag{2.138a}$$

$$\boldsymbol{K}_2 = \frac{2\pi}{a}(1, -1, 1), \tag{2.138b}$$

$$\boldsymbol{K}_3 = \frac{2\pi}{a}(1, 0, 0). \tag{2.138c}$$

When cut off at $x = a/2$, the volume enclosed by the unit, V_{AS}, is given by

$$V_{\mathrm{AS}} = \int_0^{\frac{a}{2}} \int_{-x}^{0} \int_0^{-y} dz dy dx = \frac{a^3}{48} = \frac{V_{\mathrm{CS}}}{48}, \tag{2.139}$$

where V_{CS} is the volume of the conventional unit cell. The result of Eq. 2.139 confirms that the unit chosen has the correct volume, since there are 48 rotations in the FCC point group. In general a reciprocal vector, $\boldsymbol{K}(\mathrm{AS})$, in the asymmetric

unit is given by

$$\boldsymbol{K}(\mathrm{AS}) = \frac{2\pi}{a}(j,k,l), \qquad j \in \mathbb{N}_0 \tag{2.140}$$

subject to the following conditions

$$j-k, j+l, l-k \text{ all even} \qquad \text{and} \qquad -j \leq k \leq 0, 0 \leq l \leq -k.$$

We can also define three high-symmetry planes as being the planes spanned by combinations of the vectors $\boldsymbol{K}_{1-3}$,

$$\boldsymbol{K}_4 = \alpha\boldsymbol{K}_1 + \beta\boldsymbol{K}_2 = \frac{2\pi}{a}(j,-j,l), \tag{2.141a}$$

$$\boldsymbol{K}_5 = \alpha\boldsymbol{K}_1 + \beta\boldsymbol{K}_3 = \frac{2\pi}{a}(j,k,0), \tag{2.141b}$$

$$\boldsymbol{K}_6 = \alpha\boldsymbol{K}_2 + \beta\boldsymbol{K}_3 = \frac{2\pi}{a}(j,k,-k). \tag{2.141c}$$

The asymmetric unit is shown in Figure 2.3, in which the high-symmetry lines correspond to

$$\boldsymbol{K}_1 \rightarrow \Gamma M, \tag{2.142a}$$

$$\boldsymbol{K}_2 \rightarrow \Gamma R, \tag{2.142b}$$

$$\boldsymbol{K}_3 \rightarrow \Gamma X, \tag{2.142c}$$

and the high-symmetry planes

$$\boldsymbol{K}_4 \rightarrow \Gamma RM, \tag{2.143a}$$

$$\boldsymbol{K}_5 \rightarrow \Gamma XM, \tag{2.143b}$$

$$\boldsymbol{K}_6 \rightarrow \Gamma RX. \tag{2.143c}$$

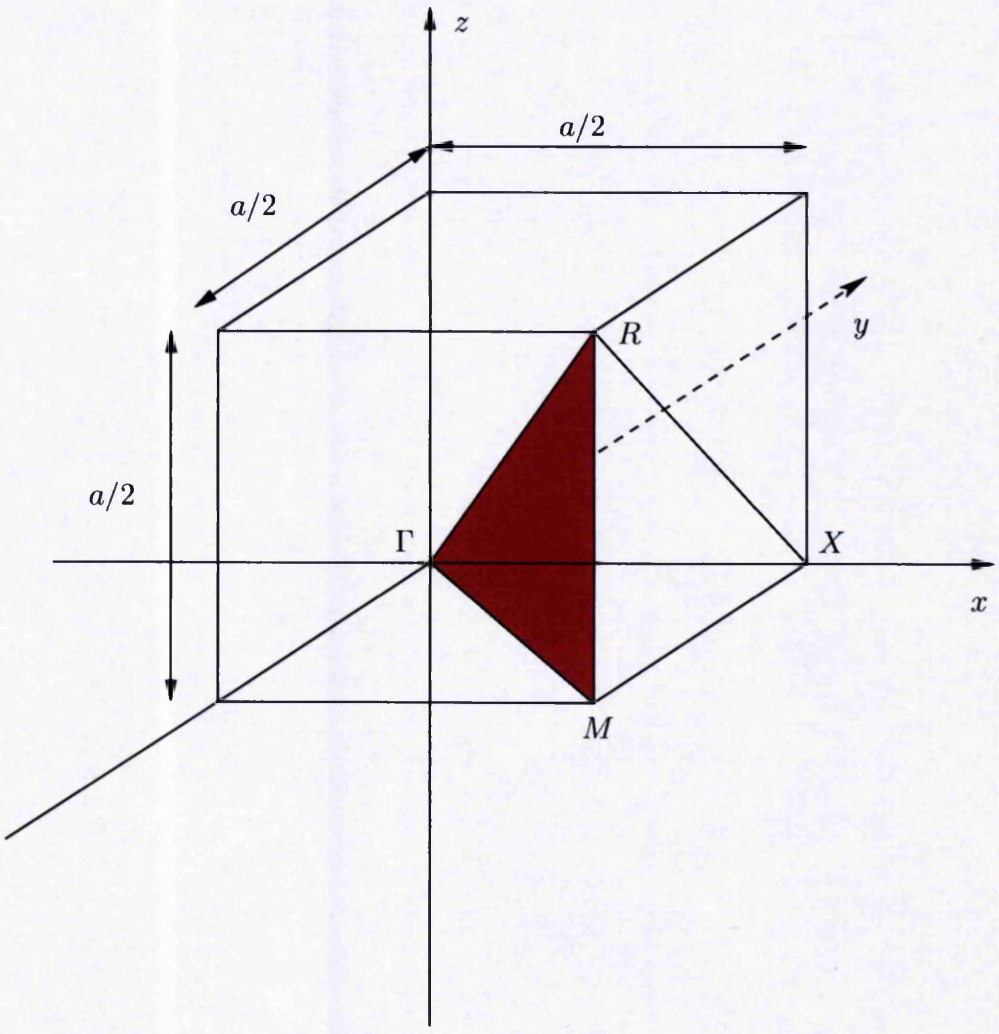

Figure 2.3: Asymmetric unit of primitive unit cell.

2.7.3 Periodic Boundary Conditions

Periodic boundary conditions are applied to all relative position vectors $\boldsymbol{r}_{ij}^{[c]}(\eta; \boldsymbol{A}_L)$. The simulation cell generated using the method outlined in Section 2.7.1 forms a parallelepiped and not a cube in our Cartesian reference frame. The implementation of periodic boundary conditions is therefore complicated by the need to rewrite our Cartesian representation of vectors in a cubic reference frame. This is required so that any changes in the vectors $\boldsymbol{r}_{ij}^{[c]}(\eta; \boldsymbol{A}_L)$ due to imposing the periodic boundary conditions occur parallel to the Bravais lattice basis vectors $\boldsymbol{a}_1, \boldsymbol{a}_2$ or $\boldsymbol{a}_3$.

A general vector in our Cartesian frame $\boldsymbol{X} = (x, y, z)$ can be written as

$$\boldsymbol{X} = x_c \frac{\boldsymbol{a}_1}{|\boldsymbol{a}_1|} + y_c \frac{\boldsymbol{a}_2}{|\boldsymbol{a}_2|} + z_c \frac{\boldsymbol{a}_3}{|\boldsymbol{a}_3|} \tag{2.144}$$

leading to

$$x = \frac{1}{\sqrt{2}} x_c + \frac{1}{\sqrt{2}} y_c \tag{2.145a}$$

$$y = -\frac{1}{\sqrt{2}} x_c - \frac{1}{\sqrt{2}} z_c \tag{2.145b}$$

$$z = \frac{1}{\sqrt{2}} y_c + \frac{1}{\sqrt{2}} z_c \tag{2.145c}$$

and

$$x_c = \frac{1}{\sqrt{2}}(x - y - z) \tag{2.146a}$$

$$y_c = \frac{1}{\sqrt{2}}(x + y + z) \tag{2.146b}$$

$$z_c = \frac{1}{\sqrt{2}}(-x - y + z) \tag{2.146c}$$

where the subscript c denotes the cubic reference frame. Periodic boundary conditions are imposed using the following replacement prescriptions

$$x_c \longrightarrow x_c - L'|\boldsymbol{a}_1| \text{ nint}\left(\frac{x_c}{L'|\boldsymbol{a}_1|}\right) \tag{2.147a}$$

$$y_c \longrightarrow y_c - L'|\boldsymbol{a}_2| \text{ nint}\left(\frac{y_c}{L'|\boldsymbol{a}_2|}\right) \tag{2.147b}$$

$$z_c \longrightarrow z_c - L'|\boldsymbol{a}_3| \text{ nint}\left(\frac{z_c}{L'|\boldsymbol{a}_3|}\right), \tag{2.147c}$$

where $L' = 2L$, and nint is the nearest integer function in the FORTRAN programming language. After imposing periodic boundary conditions we reconvert to the Cartesian coordinates to perform the calculations until further imposition of periodic boundary conditions is required.

2.8 Pair Potentials

The choice of pair potential, whilst affecting all calculated properties, is not critical for a number of physical properties, so long as the potential chosen is reasonably accurate. Our work presented here concentrates on Helium for which the most common [6] [12] [25] [20] choice of potential is one of the Aziz [2] [5] [3] HFD-B potentials. Other works have used the Lennard-Jones [31] potential or have devised their own *ab initio* potentials [9].

We have performed our Helium simulations using the HFD-B2 [4] potential given below in reduced form, Eqs. 2.148–2.150,

$$V(r) = \epsilon V^*(x), \tag{2.148}$$

A^*	1.9221529×10^5
α^*	10.73520708
C_6	1.34920045
C_8	0.41365922
C_{10}	0.17078164
β^*	-1.89296514
D	1.4135
(ϵ/k) [K]	10.94
r_m [nm]	0.2970

Table 2.3: Parameters for the HFD-B2 potential.

where

$$V^*(x) = A^* \exp(-\alpha^* x + \beta^* x^2) - F(x) \sum_{j=0}^{2} C_{2j+6}/x^{2j+6}, \tag{2.149}$$

with

$$F(x) = \begin{cases} \exp\left[-\left(\frac{D}{x} - 1\right)^2\right], & x \leq D, \\ 1, & x > D, \end{cases} \tag{2.150}$$

where $x = r/r_m$. Table 2.3 gives the values for the parameters. In addition to the pair potential we also need the first and second derivatives for the calculation of the kinetic energy components (cf. Eq. A.20). The first derivative is given by

$$v'(r) = \frac{\epsilon}{r_m} \frac{d}{dx} v^*(x) \tag{2.151}$$

where

$$\begin{aligned}\frac{dv^*(x)}{dx} =& A^*(-\alpha^* + 2\beta^* x)\exp\left\{-\alpha^* x + \beta^* x^2\right\} \\ & - F'(x)\left\{\frac{C_6}{x^6} + \frac{C_8}{x^8} + \frac{C_{10}}{x^{10}}\right\} \\ & + F(x)\left\{\frac{6C_6}{x^7} + \frac{8C_8}{x^9} + \frac{10C_{10}}{x^{11}}\right\} \end{aligned} \tag{2.152}$$

and

$$F'(x) = \begin{cases} \dfrac{2D}{x^2}\left(\dfrac{D}{x} - 1\right)\exp\left[-\left(\dfrac{D}{x} - 1\right)^2\right], & x \le D, \\ 0, & x > D. \end{cases} \tag{2.153}$$

Similarly the second derivative is given by

$$v''(r) = \frac{\epsilon}{r_m^2}\frac{d^2}{dx^2}v^*(x) \tag{2.154}$$

where

$$\begin{aligned}\frac{d^2v^*(x)}{dx^2} =& 2\beta^* A^* \exp\left\{-\alpha^* x + \beta^* x^2\right\} \\ & + A^*\left(-\alpha^* + 2\beta^* x\right)^2 \exp\left\{-\alpha^* x + \beta^* x^2\right\} \\ & - F''(x)\left\{\frac{C_6}{x^6} + \frac{C_8}{x^8} + \frac{C_{10}}{x^{10}}\right\} \\ & + 2F'(x)\left\{\frac{6C_6}{x^7} + \frac{8C_8}{x^9} + \frac{10C_{10}}{x^{11}}\right\} \\ & - F(x)\left\{\frac{42C_6}{x^8} + \frac{72C_8}{x^{10}} + \frac{110C_{10}}{x^{12}}\right\} \end{aligned} \tag{2.155}$$

and

$$F''(x) = \begin{cases} \left[\!\!\left[\begin{array}{l} \left(-\dfrac{6D^2}{x^4} + \dfrac{4D}{x^3}\right)\exp\left[-\left(\dfrac{D}{x} - 1\right)^2\right] \\ + \left[\dfrac{2D}{x^2}\left(\dfrac{D}{x} - 1\right)\right]^2 \exp\left[-\left(\dfrac{D}{x} - 1\right)^2\right] \end{array} \right]\!\!\right], & x \le D, \\ 0, & x > D. \end{cases} \tag{2.156}$$

Other potentials used in this work are the Lennard-Jones [16] (Argon) and the Tang-Toennies [32] (Krypton) potentials, the details for which are given in Appendix F. The Lennard-Jones potential is used because of its simplicity to program as well as the availability of other results [16] [17] to compare our data with. The Tang-Toennies potential allows one to compute the inter-atomic potential for all homogeneous and heterogeneous pairs of rare gas atoms. The advantage of such a potential is that one can compute properties for a range of rare gas systems by simply changing the parameters used by the potential. In addition it provides a possible route by which to calculate properties of mixed systems.

Chapter 3

Results

Whilst our derivations of the symmetry-adapted one- and two-body densities apply only to face-centred cubic structures, our work regarding the kinetic energy is independent of the structure being studied. As a consequence of this and to aid clarity our results will be presented in two sections. The first section will deal with our calculations of the one- and two-body densities using the methods set out in Section 2.2. Conversely the second section will deal with those results that are pertinent to our calculations of the kinetic energy in classical and quantum regimes. Finally in Section 3.3 we will discuss the numerical accuracy of the results presented in the preceding sections.

3.1 One- and Two-Body Densities

The results presented here are those of FCC Helium at a temperature of 300 K and at bulk particle density $\rho_0 = 0.1527\,\text{Å}^{-3}$. This thermodynamic point corresponds to one investigated experimentally by Mao *et. al.* [27] and theoretically by Gernoth [18]. The work of Mao *et. al.* [27] shows that Helium forms a hexagonal close-packed (HCP) crystal, and it is for this HCP structure that Gernoth's [18] studies are performed. However, it is well known that the FCC and HCP structures are energetically close [34] and it is with this in mind that we have performed our FCC simulations.

We have performed both classical and quantum simulations with 216 particles. In both cases 200 equilibration blocks were performed before simulating for a further 1000 blocks during which we gathered the relevant statistics. The quantum simulation was performed with 25 Fourier coefficients and 51 imaginary time steps, being the same values as used by Gernoth. We report in Table 3.1 results for the total energy, the potential energy and the total kinetic energy (all per particle) for our classical and quantum simulation as well as results given in Ref [18] for the same thermodynamic point but simulated for the HCP structure. We see that there is little difference in energy between our quantum FCC simulations and the quantum HCP simulations of Gernoth. This demonstrates the energetic closeness of the two structures. Our results, when compared with those of Gernoth [18], also confirm the findings of Mao *et. al.* [27] that the HCP struc-

	E_{tot} [K]	K_{tot} [K]	E_{pot} [K]
Classical (FCC)	2833.87 ± 0.50	601.69 ± 0.31	2232.18 ± 0.40
Quantum (FCC)	2949.15 ± 0.92	589.61 ± 0.51	2359.54 ± 0.77
Ref [18] (HCP)	2944.87 ± 0.41	592.28 ± 0.37	2352.59 ± 0.61

Table 3.1: Energies per particle for Helium at 300 K and $\rho_0 = 0.1527\,\text{Å}^{-3}$.

ture is slightly more stable than the FCC structure. Comparison of our classical FCC simulation with both quantum simulations reveals that the classical FCC structure is the most stable. However such conclusions have no physical meaning except to underline the necessity of including quantum effects.

3.1.1 One-Body Density

One of the consequences of our symmetrized representation of the one-body density is that the Fourier components for all symmetry-equivalent vectors must be identical. In Table 3.2 we show the real parts of the Fourier components for the three lowest-lying non-zero $\boldsymbol{K}$-vectors in the asymmetric unit and their symmetry-equivalent vectors, calculated in the quantum simulation. Errors are of the order 10^{-4}-10^{-5}. We see that there is slight variation in the values recorded and this can be attributed to the crystal structure being imperfect. The lack of any significant deviation confirms that the crystal possess the symmetries of the FCC space group. The results for the next seven lowest-lying $\boldsymbol{K}$-vectors in the

Vector type $\boldsymbol{K}_2$	Vector type $\boldsymbol{K}_3$	Vector type $\boldsymbol{K}_1$
$\rho(1,-1,1) = -0.1263$	$\rho(2,0,0) = 0.1185$	$\rho(2,-2,0) = 0.0923$
$\rho(-1,1,-1) = -0.1263$	$\rho(-2,0,0) = 0.1185$	$\rho(-2,2,0) = 0.0923$
$\rho(-1,-1,-1) = -0.1261$	$\rho(0,0,-2) = 0.1186$	$\rho(-2,-2,0) = 0.0924$
$\rho(1,1,1) = -0.1261$	$\rho(0,0,2) = 0.1186$	$\rho(2,2,0) = 0.0924$
$\rho(1,-1,-1) = -0.1262$	$\rho(0,2,0) = 0.1190$	$\rho(0,-2,-2) = 0.0921$
$\rho(-1,1,1) = -0.1262$	$\rho(0,-2,0) = 0.1190$	$\rho(0,2,2) = 0.0921$
$\rho(-1,-1,1) = -0.1265$		$\rho(0,-2,2) = 0.0927$
$\rho(1,1,-1) = -0.1265$		$\rho(0,2,-2) = 0.0927$
		$\rho(2,0,2) = 0.0918$
		$\rho(-2,0,-2) = 0.0918$
		$\rho(2,0,-2) = 0.0924$
		$\rho(-2,0,2) = 0.0924$

Table 3.2: Real part of the Fourier components of the one-body density for the three lowest-lying non-zero $\boldsymbol{K}$-vectors in the asymmetric unit and their symmetry-equivalent vectors. The $\boldsymbol{K}$-vectors are denoted using the integers j, k, l such that $\boldsymbol{K} = (2\pi/a)\,(j,k,l)$.

quantum case and all 10 lowest-lying non-zero $\boldsymbol{K}$-vectors in the classical case are in complete agreement with the expected findings.

We present in Figure 3.1 a plot of the quantal one-body density for the xy-plane, centred on the centre of the primitive unit cell. We also explicitly show the one-body density along the x-axis and along the $\boldsymbol{a}_1$-axis. The x- and y-axes have been labelled such that the particle lies at the origin of the plot as opposed to the centre of the primitive unit cell, $1/2(\mathbf{a}_1+\mathbf{a}_2+\mathbf{a}_3)$. The plot shows that the particle oscillates about a fixed point as one would expect for a quantum solid. Plots of the one-body density along the x-,y-, and z-axes are indistinguishable from each other, when plotted in one figure, confirming the C_4 symmetries about the x-, y-, and z-axes. Shown in Figure 3.2 is a contour plot for the classical one-body density showing the xy-plane again centred on the centre of the primitive cell, but showing surrounding lattice sites as well. The axes in Fig 3.2 have been shifted so that the origin lies at the centre of the primitive cell. Clearly visible in Fig 3.2 are four adjacent cube faces, arranged in a two-by-two grid, with particles at each of the corners and one at the centre of each face, thus confirming the FCC structure of our simulation. Figure 3.3 is the same plot as Fig. 3.2 but using data from the FPIMC simulation. Comparing Figs 3.2 and 3.3 we see that there is no difference in the positioning of the particles. However the classical particles are more localised as indicated by the higher density at the centre of the particle positions.

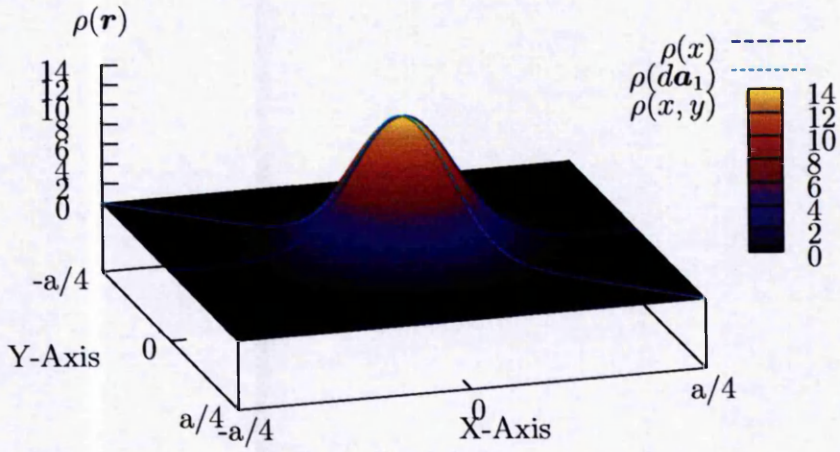

Figure 3.1: One-body density for solid FCC helium at 300 K and 0.1527 Å^{-3} from FPIMC simulation. For the coordinate system shown: $-0.5 \leq d \leq 0.5$.

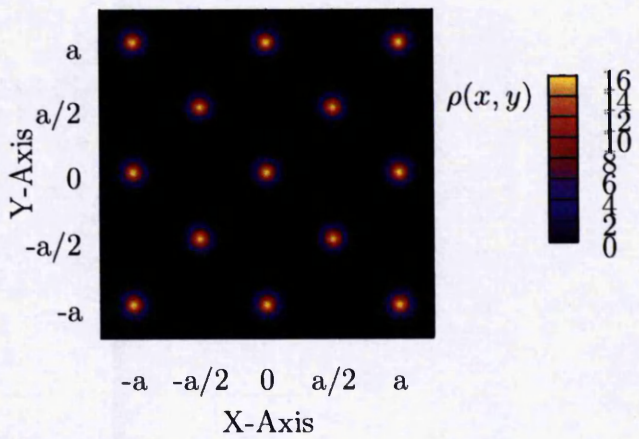

Figure 3.2: One-body density contour plot for solid FCC helium at 300 K and 0.1527 Å^{-3} from classical simulation.

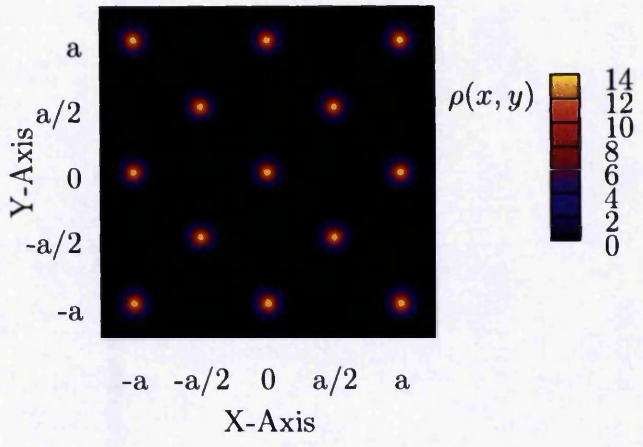

Figure 3.3: One-body density contour plot for solid FCC helium at 300 K and 0.1527 Å^{-3} from quantum simulation.

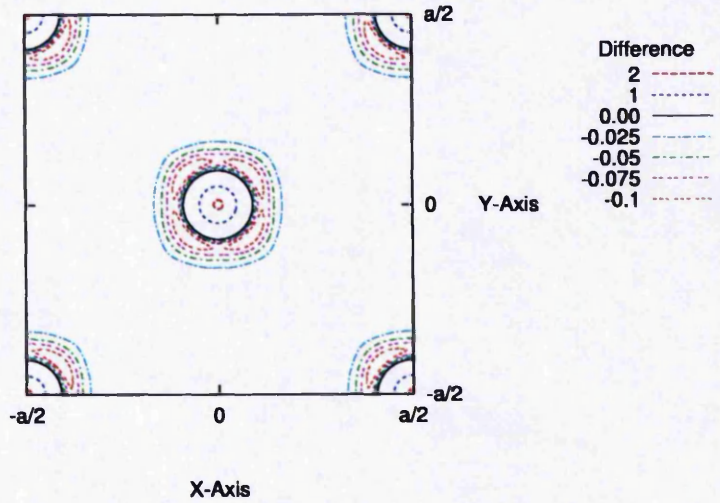

Figure 3.4: Contour plot of the difference of the classical and the FPIMC one-body density for solid FCC helium at 300 K and 0.1527 Å^{-3}.

In Fig 3.4 we show a contour plot of the difference of the one-body density from the classical simulation and the one-body density from the FPIMC simulation, in the xy-plane. The figure shows that classical one-body density is more localised, in agreement with the results for the energies. It illustrates the quantal nature of this thermodynamic point.

3.1.2 Two-Body Density

The goal of our calculations of the two-body density has been to check the application of our symmetrized approach to calculating the two-body density as opposed to calculating the two-body density in its entirety. To this end we have calculated for each one of the lowest-lying non-zero $\boldsymbol{K}$-vectors, in the six high-symmetry $\boldsymbol{K}$-vector classes, the component functions, $h_\gamma^{(\mathrm{rot})}$, of the Fourier transform of the two-body density for γ ranging from 0 to 15.

The symmetry calculations predict that for high-symmetry $\boldsymbol{K}$-vectors there will be no contribution to the Fourier transform functions, $u_{\mathrm{rot}}(\boldsymbol{r};\boldsymbol{K})$, given by Eq. 2.62 (reproduced below)

$$u_{\mathrm{rot}}(\boldsymbol{r}';\boldsymbol{K}) = \sum_{\gamma=-\infty}^{\infty} h_\gamma^{(\mathrm{rot})}(r,\theta;\boldsymbol{K})e^{i\gamma\phi}, \tag{2.62}$$

for particular values of γ. We remind the reader that the angles θ and ϕ are the polar and azimuthal angles in the rotated frame and thus the angles at which nearest neighbours are present are not necessarily the same for differing $\boldsymbol{K}$-vectors.

Considering Eq 2.66, shown below,

$$h_{\gamma}^{(\mathrm{rot})}(r, \pi - \theta; \boldsymbol{K}) e^{i\gamma\phi} = (-1)^{\gamma} h_{\gamma}^{(\mathrm{rot})}(r, \theta; \boldsymbol{K}) e^{i\gamma\phi}, \tag{2.66}$$

we see that $h_{\gamma}^{(\mathrm{rot})}(r, \theta; \boldsymbol{K})$ is anti-symmetric for γ odd and symmetric for γ even. Figures 3.5 and 3.6 show the functions $h_3^{(\mathrm{rot})}(r, \theta; \boldsymbol{K}_2)$ and $h_2^{(\mathrm{rot})}(r, \theta; \boldsymbol{K}_1)$ respectively. We see that in Fig 3.5 the plots for $\theta = 35°$ and $\theta = 180° - 35° = 145°$ are antisymmetric and in Fig 3.6 the plots for $\theta = 60°$ and $\theta = 180° - 60° = 120°$ are indistinguishable, as should be the case. These angles correspond to those angles at which nearest neighbours appear for the two $\boldsymbol{K}$-vector classes. It is interesting to note that for $\theta = 90°$ there is no contribution for γ odd. This is explained by Eq. 2.66, since it states that such $h_{\gamma}^{\mathrm{rot}}(r, \theta; \boldsymbol{K})$ are antisymmetric which is only possible if it is zero for all r, when $\theta = 90°$.

Presented in Figures 3.7- 3.14 are the real and, where appropriate, imaginary parts of the functions $h_{\gamma}^{(\mathrm{rot})}(r, \theta; \boldsymbol{K})$ for each of the six high-symmetry vector classes with γ chosen such that the predicted patterns (Table 2.2) can be seen without overly crowding the plots. Analysing all the component functions we find no contributions for those γ which are prohibited on symmetry grounds. In addition where contributions are found they are symmetric or antisymmetric according to Eq. 2.66. Comparison of the classical and quantum simulations shows that there is a lowering and broadening of the peak heights and widths in the quantum case which as with the one-body density is caused by the quantal delocalisation of the particles.

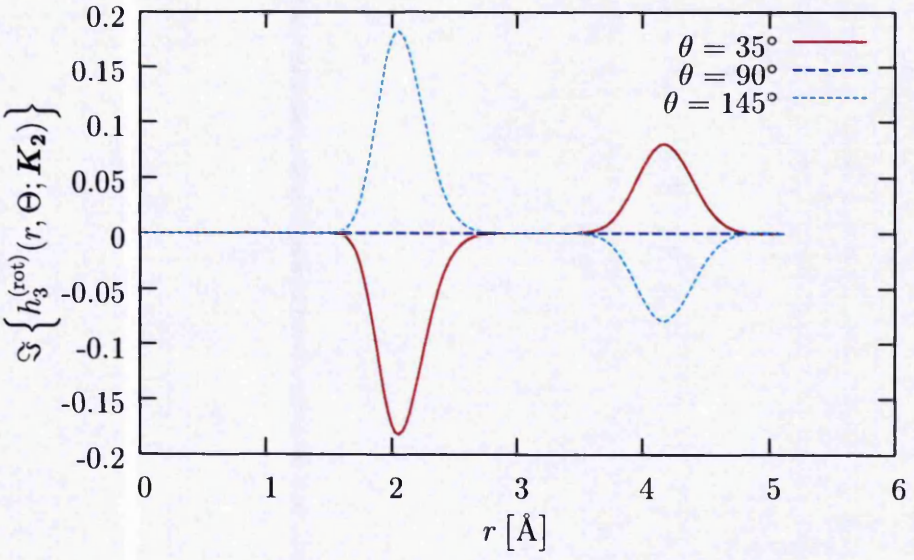

Figure 3.5: Imaginary part of component function $h_3^{(\mathrm{rot})}(r, \theta; \boldsymbol{K}_2)$ for solid FCC helium from FPIMC simulations at 300 K and 0.1527 Å^{-3}.

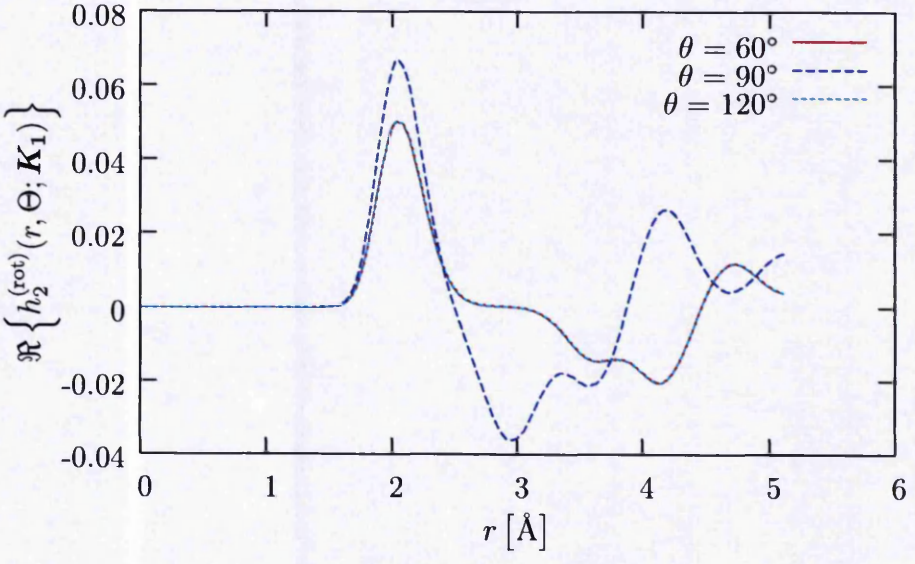

Figure 3.6: Real part of component function $h_2^{(\mathrm{rot})}(r, \theta; \boldsymbol{K}_1)$ for solid FCC helium from FPIMC simulations at 300 K and 0.1527 Å^{-3}.

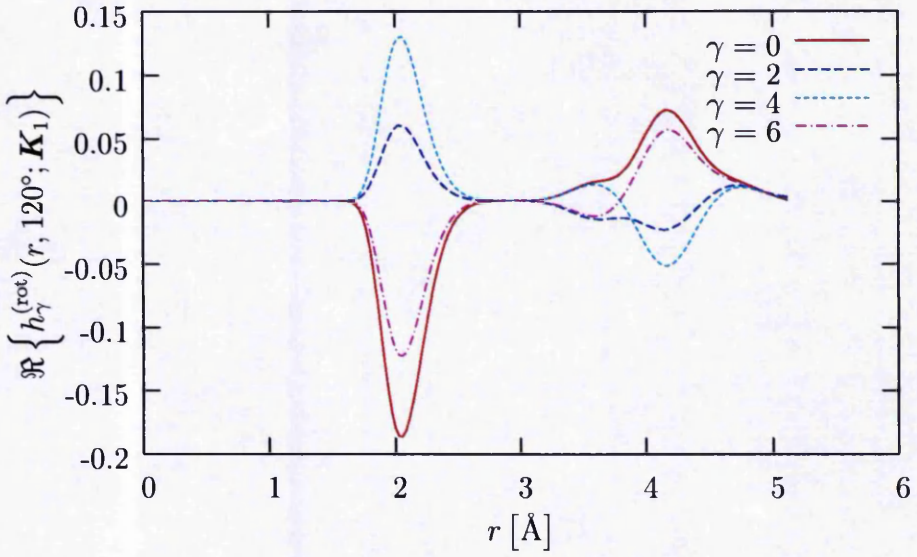

Figure 3.7: Real part of component function $h_\gamma^{(\mathrm{rot})}(r, 120°; \boldsymbol{K}_1)$ for solid FCC helium from classical simulations at 300 K and 0.1527 Å^{-3}.

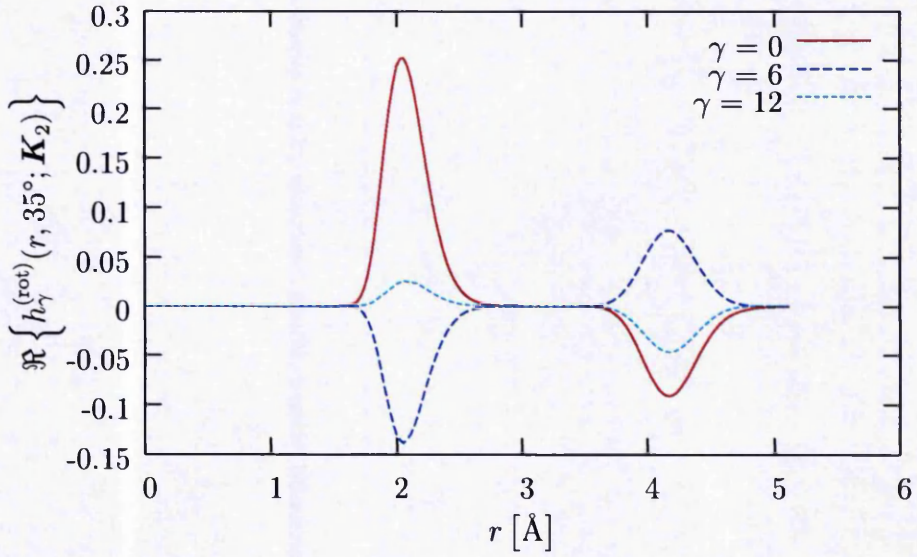

Figure 3.8: Real part of component function $h_\gamma^{(\mathrm{rot})}(r, 35°; \boldsymbol{K}_2)$ for solid FCC helium from classical simulations at 300 K and 0.1527 Å^{-3}.

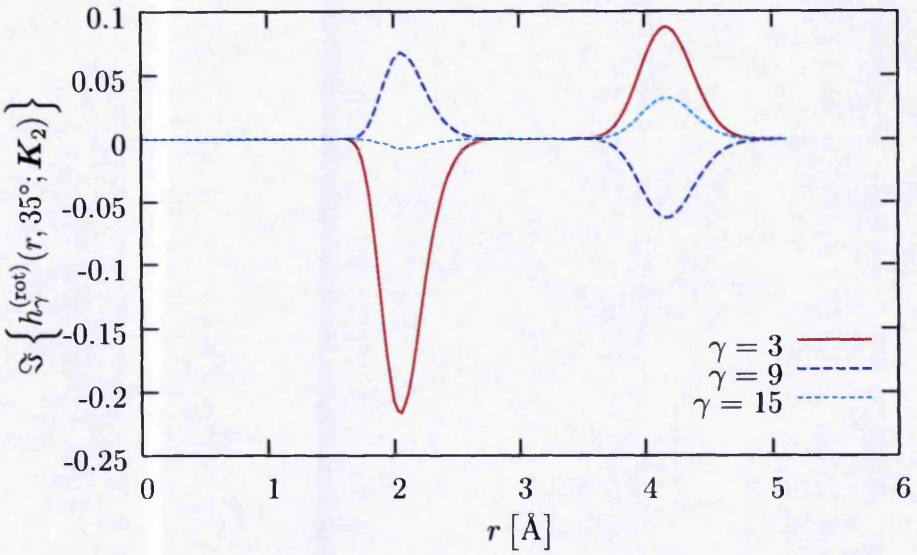

Figure 3.9: Imaginary part of component function $h_\gamma^{(\mathrm{rot})}(r, 35°; \boldsymbol{K}_2)$ for solid FCC helium from classical simulations at 300 K and 0.1527 Å^{-3}.

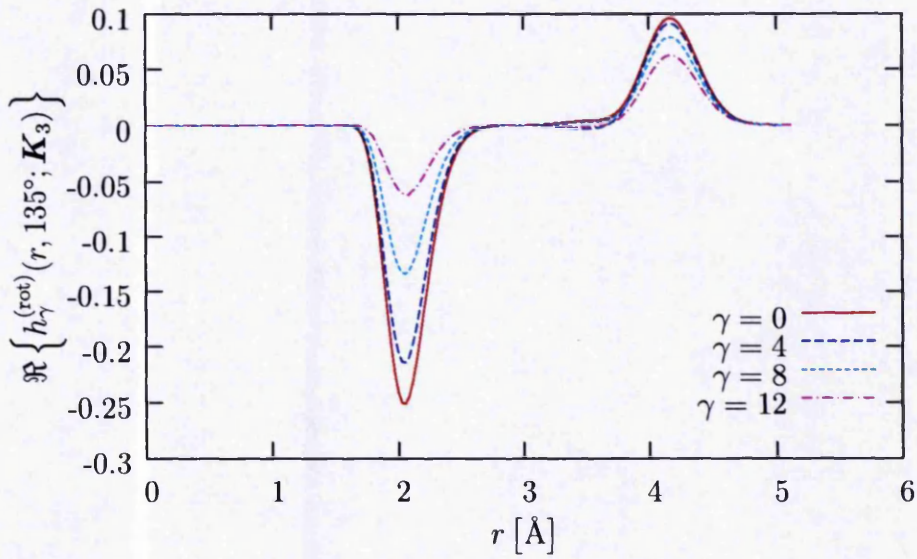

Figure 3.10: Real part of component function $h_\gamma^{(\mathrm{rot})}(r, 135°; \boldsymbol{K}_3)$ for solid FCC helium from classical simulations at 300 K and 0.1527 Å^{-3}.

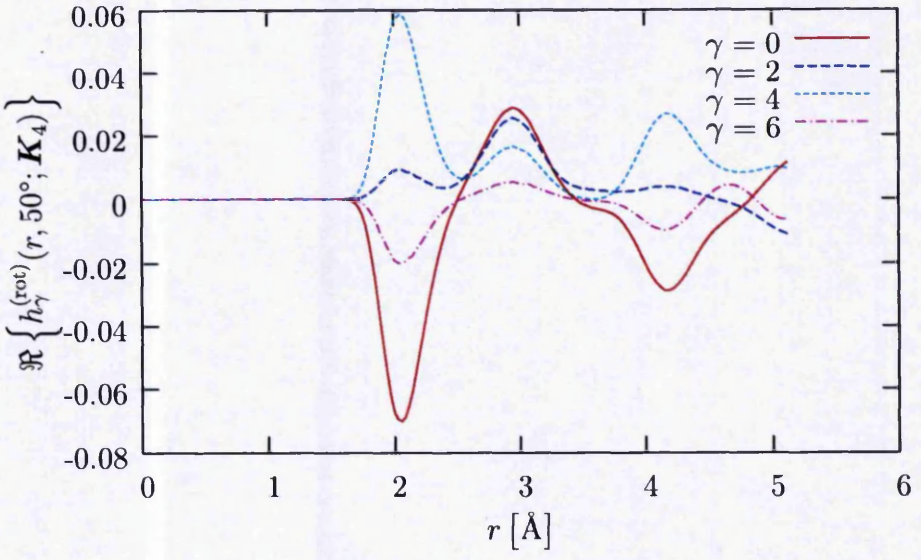

Figure 3.11: Real part of component function $h_\gamma^{(\mathrm{rot})}(r, 50°; \boldsymbol{K}_4)$ for solid FCC helium from classical simulations at 300 K and 0.1527 Å^{-3}.

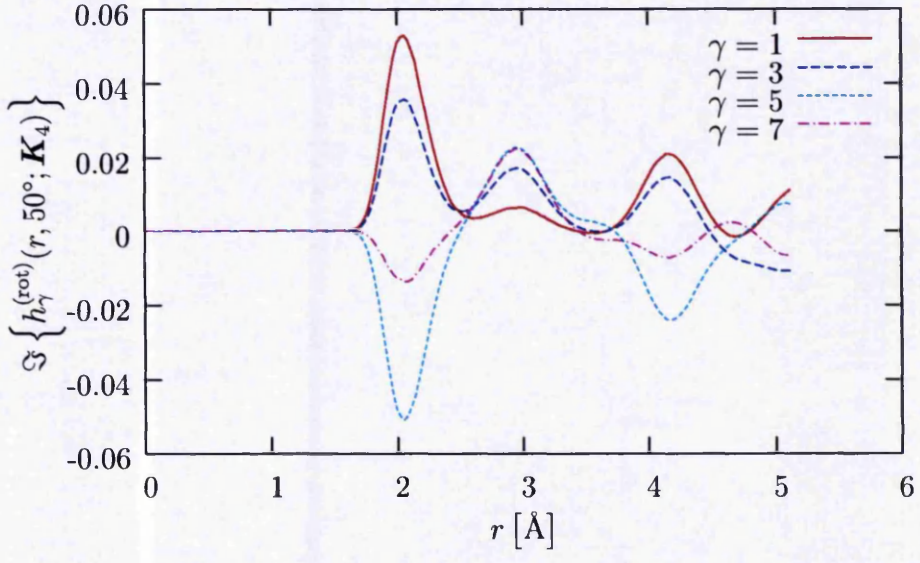

Figure 3.12: Imaginary part of component function $h_\gamma^{(\mathrm{rot})}(r, 50°; \boldsymbol{K}_4)$ for solid FCC helium from classical simulations at 300 K and 0.1527 Å^{-3}.

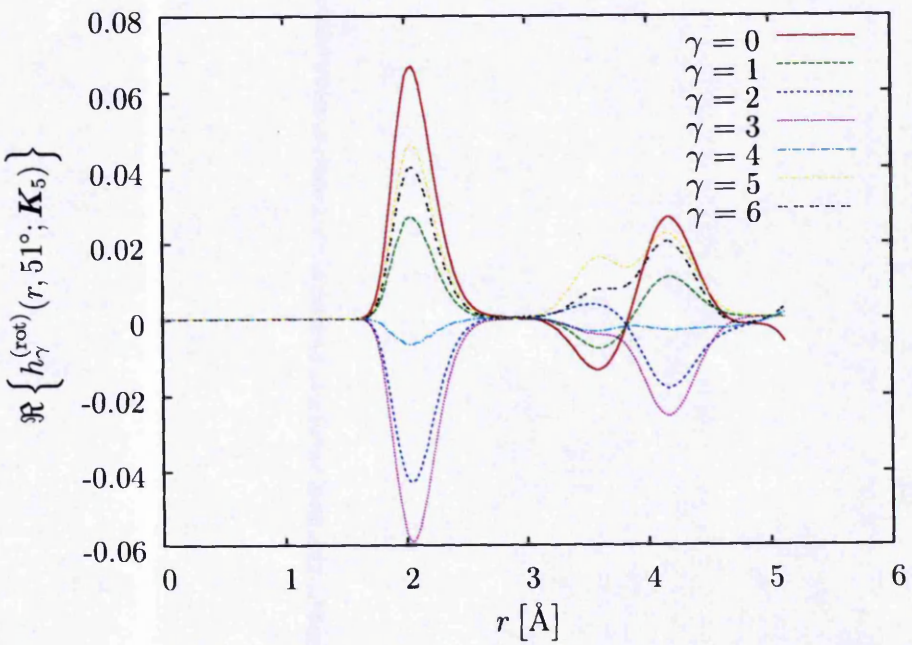

Figure 3.13: Real part of component function $h_\gamma^{(\mathrm{rot})}(r, 51°; \boldsymbol{K}_5)$ for solid FCC helium from classical simulations at 300 K and 0.1527 Å^{-3}.

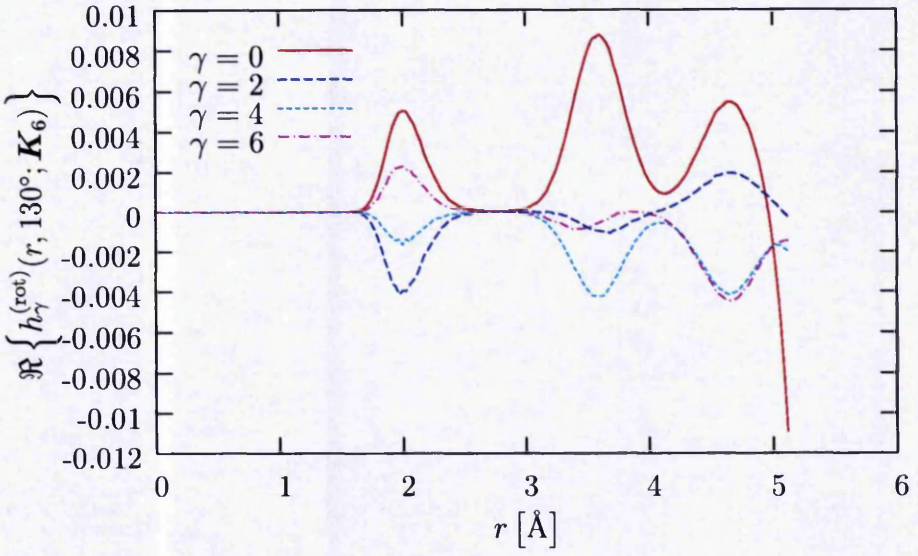

Figure 3.14: Real part of component function $h_\gamma^{(\mathrm{rot})}(r, 130°; \boldsymbol{K}_6)$ for solid FCC helium from classical simulations at 300 K and 0.1527 Å^{-3}.

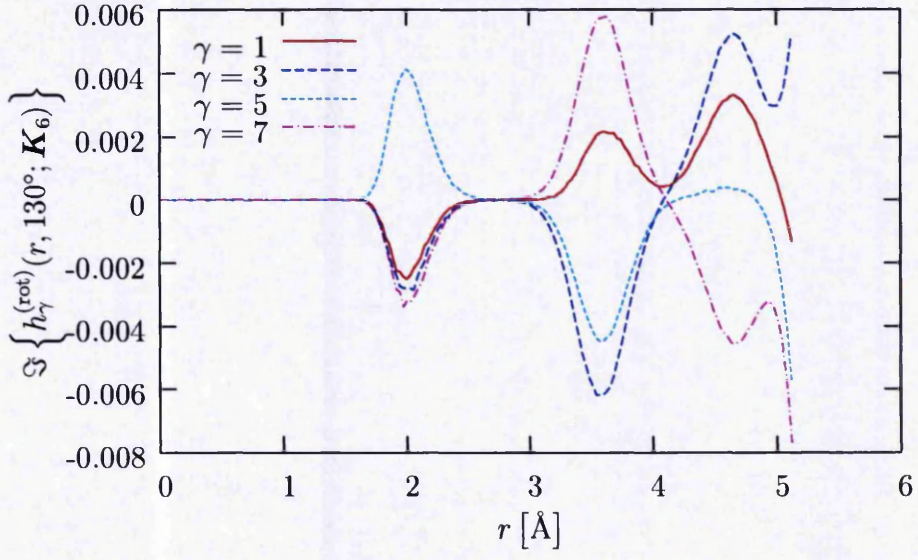

Figure 3.15: Imaginary part of component function $h_\gamma^{(\mathrm{rot})}(r, 130°; \boldsymbol{K}_6)$ for solid FCC helium from classical simulations at 300 K and 0.1527 Å^{-3}.

Lattice distance	Value for $\rho = 0.1527\,\text{Å}^{-3}$
$\sqrt{1/2}\,a$	2.10 Å
a	2.97 Å
$\sqrt{3/2}\,a$	3.64 Å
$\sqrt{2}\,a$	4.20 Å
$\sqrt{5/2}\,a$	4.70 Å

Table 3.3: Nearest-neighbour distances for an FCC crystal.

Calculations have also been made of the angle-averaged radial distribution function $g(r)$. This gives the probability density of finding two particles a distance r apart. For large r the function $g(r)$ tends to one. The nearest-neighbour distances for an FCC crystal are given in Table 3.3. Analysis of Fig 3.16 shows all nearest-neighbour peaks to be present with the exception of a peak at $\sqrt{2}\,a$. Checking the data file shows a local maximum for $r = 4.20$, suggesting that the peak is obscured by the neighbouring peaks.

3.2 Kinetic Energy as a Quantum Indicator

We have performed both classical MC and FPIMC simulations for liquid Helium for a range of temperatures with a fixed bulk particle number density ρ_0. The initial structure of the simulations is FCC. However, this structure is allowed to melt before any statistics are gathered. The initial thermodynamic point

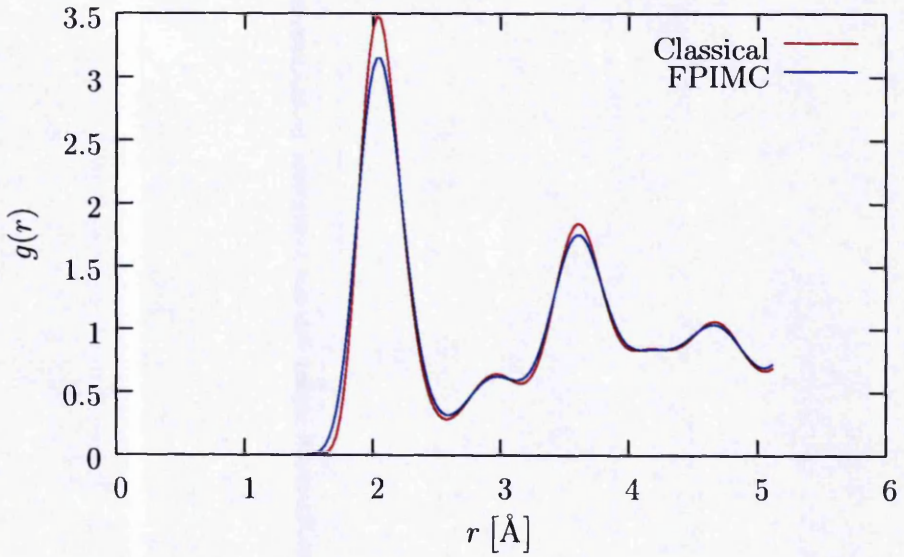

Figure 3.16: Radial distribution function $g(r)$ from classical and FPIMC simulations of solid FCC helium at 300 K and 0.1527 $Å^{-3}$.

studied was for a density $\rho_0 = 0.02185\,Å^{-3}$ and at a temperature $T = 12\,K$. The temperature is decreased in intervals of 2 K for successive simulations down to 4 K.

Simulations were performed for 216 particles and, for the FPIMC simulations, with 900 Fourier coefficients and 181 imaginary time steps. The results for the various energy components for the classical and FPIMC simulations are presented in Tables 3.4 and 3.5, respectively.

As discussed in Section 2.6.3 the melting of the FCC lattice for very low temperatures proceeded extremely slowly. All the results were simulated using the smaller move size of 0.03 Åwith the exception of the FPIMC simulations at

T [K]	12	10	8	6	4
E_{tot} [K]	7.84±0.15	7.31±0.24	12.04±0.34	26.65±0.40	66.21±0.54
E_{pot} [K]	$-29.17\pm1.9\times10^{-2}$	$-32.40\pm3.0\times10^{-2}$	$-40.05\pm3.2\times10^{-2}$	$-47.21\pm2.0\times10^{-2}$	$-55.53\pm1.1\times10^{-2}$
K_{tot} [K]	37.01±0.15	39.71±0.24	52.09±0.34	73.86±0.40	121.74±0.54
K_2 [K]	76.14±0.11	99.06±0.18	160.63±0.25	258.89±0.28	463.69±0.36
K_3 [K]	−57.12±0.10	−74.34±0.16	−120.53±0.22	−194.03±0.28	−347.96±0.40
K_{3a} [K]	−60.11±0.12	−78.97±0.18	−131.80±0.27	−219.36±0.37	−414.15±0.62
K_{3b} [K]	2.99±0.16	4.63±0.24	11.27±0.35	25.33±0.47	66.19±0.74

Table 3.4: Energy components for low-temperature liquid He at 0.02185 Å^{-3} (classical simulations).

T [K]	12	10	8	6†	4†
$E_{\rm tot}$ [K]	6.51±0.20	3.72±0.25	1.05±0.27	−1.50±0.34	−3.22±0.62
$E_{\rm pot}$ [K]	$-21.29\pm4.9\times10^{-2}$	$-21.42\pm5.3\times10^{-2}$	$-21.31\pm5.2\times10^{-2}$	$-21.48\pm4.3\times10^{-2}$	$-21.89\pm3.9\times10^{-2}$
$K_{\rm tot}$ [K]	27.80±0.19	25.14±0.24	22.36±0.27	19.98±0.34	18.67±0.62
K_2 [K]	78.10±0.11	89.51±0.13	105.81±0.13	130.96±0.15	184.60±0.23
K_3 [K]	−68.29±0.16	−79.36±0.20	−95.45±0.23	−119.97±0.30	−171.94±0.58
K_{3a} [K]	−72.76±0.18	−84.74±0.24	−101.53±0.26	−127.92±0.34	−183.99±0.63
K_{3b} [K]	4.47±0.24	5.38±0.31	6.08±0.35	7.95±0.45	12.06±0.86

Table 3.5: Energy components for low-temperature liquid He at 0.02185 Å^{-3} (quantum simulations).† see text.

6 K and 4 K which used the larger move size of 0.4 Å. Using the larger move size required 200 and 400 melting blocks for, respectively, 6 K and 4 K as opposed to 600 and 800 with the smaller move size.

As expected we see that the classical results do not give an accurate picture of the energies involved. Where the FPIMC potential energy appears to be almost constant as the temperature is decreased we see that the classical potential energy becomes more negative as the temperature is decreased. More surprising is that, whilst the total quantum kinetic energy decreases with temperature, the semiclassical kinetic energy increases with decreasing temperature, when the quantum correction is included. This implies that for highly quantum systems the quantum correction to the classical Boltzmann kinetic energy breaks down.

Since for classical simulations the ratio $K_3/K_2 = -0.75$ is constant we can use this ratio as a measure of how quantum a system is. The ratio K_3/K_2 for the FPIMC simulations is shown in Fig 3.17, in which we clearly see the increasing deviation from the semiclassical value of -0.75 as the temperature decreases. Further investigation of this ratio is required for temperatures outside the range presented here to establish the behaviour both as T approaches zero and as T approaches the quantum-to-classical boundary. The term boundary is used to denote the region where quantum effects become negligible as opposed to a quantum-to-classical phase transition. It is expected that the curve would asymptotically approach the semiclassical limit of -0.75 as T increases. This

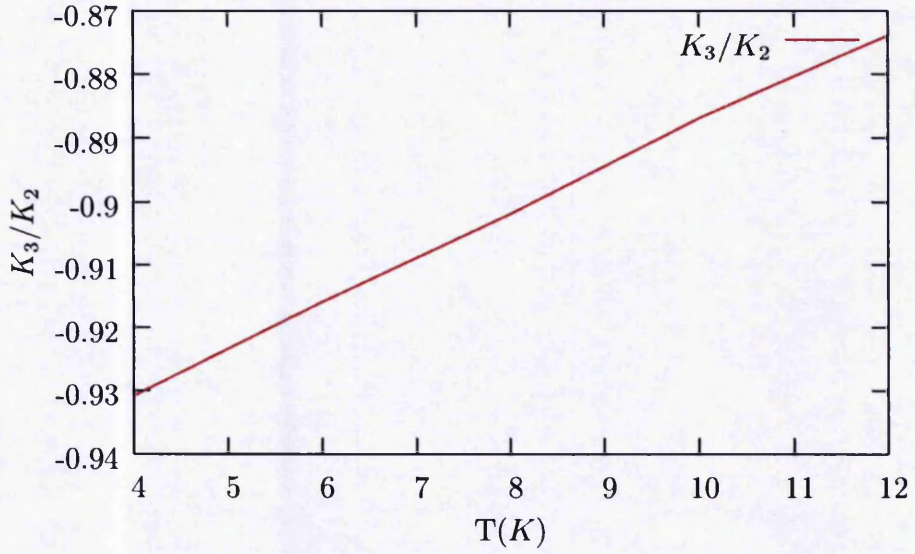

Figure 3.17: Ratio of K_3/K_2 from FPIMC simulations for liquid helium at 0.02185 Å^{-3}.

would imply that the curve in Fig 3.17 is not a straight line despite appearing to be so. Harder to predict is the behaviour as T tends to zero, since the only contribution to the kinetic energy at zero temperature is from quantum terms. It is expected that exchange effects will be present and become important at lower temperatures [8]. These will be especially important because of the low mass of Helium. Additionally the ratio appears to be approaching minus one for $T = 0$, which would mean that the two- and three-body terms would cancel each other.

Simulations have been also been performed for liquid Krypton at 118 K and a particle density of 0.01734 Å^{-3}, this thermodynamic point being one investigated by Wang *et al.* [36]. The simulations were performed using the Tang-Tonnies [32]

Simulation	FPIMC	Classical
E_{tot} [K]	-864.77 ± 0.14	-865.81 ± 0.13
E_{pot} [K]	-1043.90 ± 0.14	-1044.95 ± 0.13
K_{tot} [K]	$179.13 \pm 8.71 \times 10^{-3}$	$179.14 \pm 8.24 \times 10^{-3}$
K_2 [K]	$8.55 \pm 5.57 \times 10^{-3}$	$8.53 \pm 5.14 \times 10^{-3}$
K_3 [K]	$-6.42 \pm 6.69 \times 10^{-3}$	$-6.39 \pm 6.45 \times 10^{-3}$
K_{3a} [K]	$-7.16 \pm 1.01 \times 10^{-2}$	$-7.14 \pm 9.69 \times 10^{-3}$
K_{3b} [K]	$0.74 \pm 1.22 \times 10^{-2}$	$0.75 \pm 1.16 \times 10^{-3}$

Table 3.6: Energies for Krypton from FPIMC and classical MC simulations at 118 K and 0.01734 Å^{-3}.

potential as described in Appendix F.1. We present in Table 3.6 results from our FPIMC and classical MC simulations. Our results for the kinetic energy indicate that quantum effects at this thermodynamic point are minimal. The quantum correction to the classical Boltzmann kinetic energy is approximately 2 K and is a valid correction in this very mildly quantum state. The ratio of the quantum kinetic energy components $K_3/K_2 = -0.749$ indicates that we are in the semiclassical limit. Therefore simulations for the same density ρ_0 at $T \geq 118$ K need only be undertaken using the classical simulation techniques with the quantum correction term to the kinetic energy added. This will enable a larger number of detailed simulations to be undertaken, since the computation

time for a quantum simulation is proportional to the square of the number of particles multiplied by the number of imaginary time steps, whereas the classical simulation run time is proportional to the square of the number of particles only. Comparison of the radial distribution function $g(r)$ from both the classical and FPIMC simulations, shown in Figure 3.18, shows that they are indistinguishable on the scale of such a plot. Additionally, we find there is agreement with the results reported by Wang *et al.* [36] as to the location of the maxima and minima of $g(r)$. Our results appear to show a slightly higher first peak 3.1 as opposed to 2.8. The difference may be due to the differing simulation techniques used to calculate the radial distribution function. The data in Ref. [36] is from a Reverse Monte Carlo simulation which uses data gathered from extended x-ray absorption fine structure (EXAFS) experiments to calculate $g(r)$.

The final set of results to be presented are those from our simulations of solid FCC Argon at the triple point, $T = 83.806\,\mathrm{K}$ and $\rho_0 = 0.02445\,\mathrm{\AA}^{-3}$. The point is chosen so that comparison with results of Gernoth [16] [17] is possible. The simulations were undertaken for 216 Argon atoms starting in a perfect FCC crystal structure. As with other simulations 200 equilibration blocks were performed before gathering statistics for a further 1000 blocks. The FPIMC simulation used 10 imaginary time steps and 25 Fourier coefficients. Table 3.7 gives details of the various energy components as calculated in our classical and FPIMC simulations as well as results of Gernoth [16]. The results of Gernoth are from an FPIMC

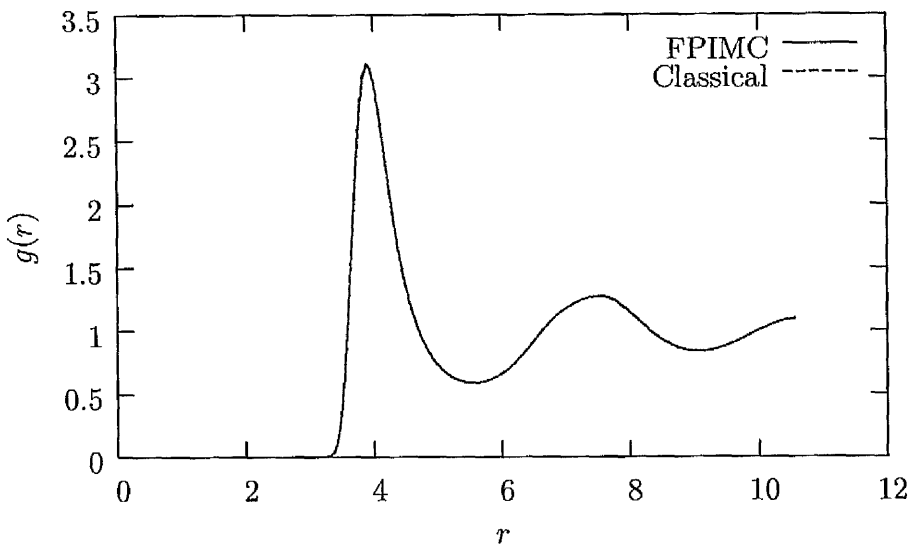

Figure 3.18: Radial distribution function for Krypton at 118 K and 0.01734 $Å^{-3}$.

simulation at the same thermodynamic point but performed with a hexagonal simulation cell. The data in Table 3.7 shows that the kinetic energies at the triple point of argon can be simulated using our classical simulation with the quantum correction. Comparing the potential energy we see that there is a difference of 4 K between the classical and FPIMC simulations suggesting that the quantum simulation should still be used. The difference between the two potential energies arises from the probability of accepting a particle move and not the potential energy estimator. We see that there is a good agreement between our FPIMC results and the results of Gernoth as should be the case. This agreement for identical thermodynamic points of simulations performed with differing codes (albeit using the same simulation techniques) allows us to have confidence that

Simulation	FPIMC	Classical	FPIMC Ref. [16]
E_{tot} [K]	-734.37 ± 0.15	$-738.47\pm8.64 \times 10^{-2}$	-735.474 ± 0.122
E_{pot} [K]	-866.15 ± 0.15	$-870.18\pm8.46 \times 10^{-2}$	-867.170 ± 0.23
K_{tot} [K]	$131.78\pm3.07 \times 10^{-2}$	$131.71\pm1.74 \times 10^{-2}$	131.695 ± 0.014
K_2 [K]	$24.31\pm1.39 \times 10^{-2}$	$23.86\pm8.30 \times 10^{-3}$	
K_3 [K]	$-18.24\pm2.74 \times 10^{-2}$	$-17.87\pm1.53 \times 10^{-2}$	
K_{3a} [K]	$-16.56\pm3.37 \times 10^{-2}$	$-16.25\pm1.97 \times 10^{-2}$	
K_{3b} [K]	$-1.68\pm4.34 \times 10^{-2}$	$-1.62\pm2.50 \times 10^{-2}$	

Table 3.7: Energies for Argon from FPIMC and classical MC simulations at 83.806 K and 0.02445 Å^{-3}.

there are no systematic errors in the programming of our code.

3.3 Numerical Accuracy and Systematic Errors

When performing numerical simulations it is important to understand the limitations of the techniques employed. All observables calculated in this work by means of either classical Monte Carlo or FPIMC simulations are written to a file after every 100 blocks. This enables one to check that convergence has been reached at the end of the simulation. We remind the reader that a block consists of 100 steps and a step is attempting to move successively all particles once. All results presented in this work show convergence to the values reported, within

the statistical errors reported.

Statistical errors $\Delta\epsilon$ for a quantity ϵ are calculated by

$$\Delta\epsilon = \frac{1}{N_{\text{blocks}}}\sqrt{\sum_{n=1}^{N_{\text{blocks}}}\left[\epsilon(n) - \langle\epsilon\rangle\right]^2}, \tag{3.1}$$

where $\epsilon(n)$ is the average value of the quantity ϵ during the n^{th} block and $\langle\epsilon\rangle$ is the average value of ϵ from all blocks.

Whilst the statistical errors can be reduced by simulating for a larger number of blocks there will always remain some systematic errors. One of the most important issues stems from so-called finite-size effects. Finite-size effects are a result of the simulation cell being too small causing the cut-off distance r_{limit} to truncate the pair potential before it becomes sufficiently small. Additionally, care must be taken to ensure that the number of imaginary time steps and the number of Fourier coefficients are large enough. In order to assess the effect of finite-size phenomena we have repeated a simulation for liquid Helium at 4 K and $0.02185\,\text{Å}^{-3}$. In this new simulation we have increased the number of particles from 216 to 512, the number of imaginary time steps from 181 to 201 and the number of Fourier coefficients from 900 to 1000. The simulation was performed using 200 equilibrium blocks followed by 200 simulation blocks. The number of simulation blocks was reduced from the normal 1000 as the simulation time is proportional to the number of imaginary time steps and to the square of the number of particles resulting in a largely increased run time. Table 3.8 shows various energy components as simulated for 216 and 512 particles. It is clear that

$N_{\text{Particles}}$	Total Energy	Potential Energy	Kinetic Energy
216	$-3.22\text{K}\pm0.62\text{K}$	$-21.89\text{K}\pm3.90\times10^{-2}\text{K}$	$18.67\text{K}\pm0.62\text{K}$
512	$-3.17\text{K}\pm0.96\text{K}$	$-21.42\text{K}\pm6.42\times10^{-2}\text{K}$	$18.14\text{K}\pm0.96\text{K}$

Table 3.8: Energies for liquid Helium at 4 K and 0.02185 Å^{-3} for differing numbers of particles from FPIMC simulations.

there is no significant change in values as a result of increasing the size of the simulation. Thus we have confidence that all results presented in this work are not affected to any significant degree by finite-size effects. Figure 3.19 shows the radial distribution function for Helium calculated with 216 and 512 particles. It is clear that the location and height of the peaks are identical, but that the data from the 512 particles are noisier. This is due to the reduction in the number of blocks for which the simulation was performed. It is also obvious that the increase in the number of particles has allowed the calculation of $g(r)$ to larger values of r.

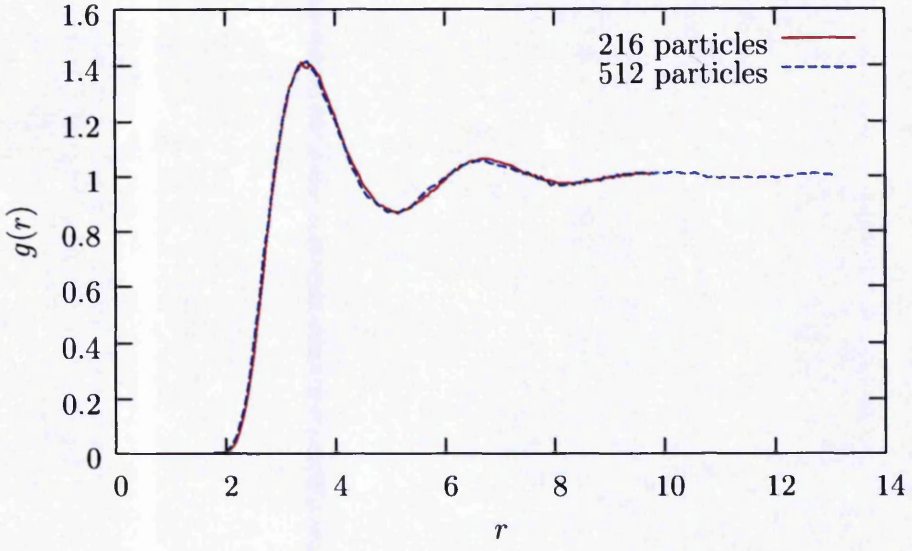

Figure 3.19: Radial distribution function for Helium at 4 K and 0.02185 $Å^{-3}$ with differing numbers of particles from FPIMC simulations.

Chapter 4

Discussion and Outlook

In this work we have presented a rigorous theoretical description of the symmetries of the one- and two- body densities for FCC structures. Additionally we have shown how the quantum kinetic energy can be written as the sum of the classical Boltzmann kinetic energy plus explicit two- and three-body terms. We have also shown that the semiclassical limit of this quantum kinetic energy can be used as a correction to the Boltzmann kinetic energy. The rest of this chapter is devoted to discussing areas of possible future work building on the work undertaken in this thesis.

4.1 Applications to Other Cubic Lattices

The theoretical concepts invoked in our calculations of the symmetries of the one- and two-body densities are an application of the work of Gernoth [16, 17, 18]. In

the same way that we have applied Gernoth's general formalism to FCC crystals it is possible to extend the methods herein outlined to other crystal structures. From a computational point of view our work would most readily be employed in calculations for simple cubic (SC) and body centred cubic (BCC) crystals. This is rather straightforward, because the only changes to the code are to the lattice basis vectors and associated reciprocal lattice vectors.

We present here the derivations of the $\boldsymbol{K}$-vectors for both the SC and BCC structures. Taking the SC crystal first and following the approach taken in Sec. 2.7.1 the basis vectors of the primitive cell of the SC lattice are

$$\boldsymbol{a}_1 = a\,(0,-1,0)\,, \tag{4.1a}$$

$$\boldsymbol{a}_2 = a\,(1,0,0)\,, \tag{4.1b}$$

$$\boldsymbol{a}_3 = a\,(0,0,1)\,, \tag{4.1c}$$

where again we have a^3 as the volume of the conventional cell and $a^3 = 1/\rho$. Similarly the basis vectors of the reciprocal lattice are

$$\boldsymbol{b}_1 = \frac{2\pi}{\Omega}\boldsymbol{a}_2 \times \boldsymbol{a}_3 = \frac{2\pi}{a}\,(0,-1,0)\,, \tag{4.2a}$$

$$\boldsymbol{b}_2 = \frac{2\pi}{\Omega}\boldsymbol{a}_3 \times \boldsymbol{a}_1 = \frac{2\pi}{a}\,(1,0,0)\,, \tag{4.2b}$$

$$\boldsymbol{b}_3 = \frac{2\pi}{\Omega}\boldsymbol{a}_1 \times \boldsymbol{a}_2 = \frac{2\pi}{a}\,(0,0,1)\,. \tag{4.2c}$$

A reciprocal lattice vector is therefore

$$\boldsymbol{K} = k_1\boldsymbol{b}_1 + k_2\boldsymbol{b}_2 + k_3\boldsymbol{b}_3, \tag{4.3a}$$

$$= \frac{2\pi}{a}(k_2, -k_1, k_3) \quad k_1, k_2, k_3 \in \mathbb{Z}_0, \tag{4.3b}$$

$$= \frac{2\pi}{a}(j, k, l), \quad j, k, l \in \mathbb{Z}_0. \tag{4.3c}$$

No further restrictions are placed on j, k, l for a simple cubic crystal.

The BCC crystal basis vectors are

$$\boldsymbol{a}_1 = \frac{a}{2}(1, -1, -1), \tag{4.4a}$$

$$\boldsymbol{a}_2 = \frac{a}{2}(1, 1, 1), \tag{4.4b}$$

$$\boldsymbol{a}_3 = \frac{a}{2}(-1, -1, 1), \tag{4.4c}$$

with $a^3 = 2/\rho$ since there are 2 particles per primitive unit cell. Likewise the reciprocal lattice vectors are

$$\boldsymbol{b}_1 = \frac{2\pi}{\Omega}\boldsymbol{a}_2 \times \boldsymbol{a}_3 = \frac{2\pi}{a}(1, -1, 0), \tag{4.5a}$$

$$\boldsymbol{b}_2 = \frac{2\pi}{\Omega}\boldsymbol{a}_3 \times \boldsymbol{a}_1 = \frac{2\pi}{a}(1, 0, 1), \tag{4.5b}$$

$$\boldsymbol{b}_3 = \frac{2\pi}{\Omega}\boldsymbol{a}_1 \times \boldsymbol{a}_2 = \frac{2\pi}{a}(0, -1, 1), \tag{4.5c}$$

from which a general reciprocal lattice vector can be expressed as

$$\boldsymbol{K} = k_1\boldsymbol{b}_1 + k_2\boldsymbol{b}_2 + k_3\boldsymbol{b}_3, \tag{4.6a}$$

$$= \frac{2\pi}{a}(k_1 + k_2, -k_1 - k_3, k_2 + k_3), \tag{4.6b}$$

$$= \frac{2\pi}{a}(j, k, l), \quad k_1, k_2, k_3 \in \mathbb{Z}_0. \tag{4.6c}$$

Using Eqs. 4.6b and 4.6c we derive the following

$$j + k + l = 2k_2, \tag{4.7a}$$

$$j + k - l = -2k_3, \tag{4.7b}$$

$$j - k - l = 2k_1. \tag{4.7c}$$

Thus the reciprocal lattice vectors $\boldsymbol{K} = \frac{2\pi}{a}(j, k, l)$ are subject to

$$\left.\begin{array}{l} j + k + l \\ j + k - l \\ j - k - l \end{array}\right\} \text{ even.} \tag{4.8}$$

It should be noted that the reciprocal lattice of the BCC crystal is an FCC crystal lattice, and the reciprocal lattice of an FCC crystal is a BCC crystal lattice.

The three crystals FCC, BCC and SC all exhibit the same symmetries. As a result the asymmetric unit has the same essential shape for all the crystals. However the different crystals have differing reciprocal lattices and therefore differing $\boldsymbol{K}$-vectors. For the SC crystal this yields as asymmetric unit

$$\boldsymbol{K}(\text{AS}) = \frac{2\pi}{a}(j, k, l), \tag{4.9}$$

subject to $j \geq 0, -j \leq k \leq 0, 0 \leq l \leq -k$. For the BCC crystal we have the same result subject to the extra condition that

$$j + k + l, j + k - l, j - k - l \qquad \text{all even.} \tag{4.10}$$

Additionally the six high-symmetry vector classes have the same form for all three crystal types, although the $\boldsymbol{K}$-vectors themselves differ between the lattice

types. This means that the symmetry patterns seen in the component functions $h_\gamma^{(\mathrm{rot})}(r, \theta; \boldsymbol{K})$ will be the same for the three crystal types for the same $\boldsymbol{K}$-vector class.

Likewise the symmetrized form of the one-body density is only affected in that the specific $\boldsymbol{K}$-vectors used in the simulations differ. The values of $g_0(\boldsymbol{K})$ for $\boldsymbol{K}$-vectors in one of the six high-symmetry vector classes are identical for the three crystals.

4.2 Quantum Kinetic Energy

The work presented here sets the foundations for a detailed analysis of the components of the kinetic energy to be performed. Of particular interest is the behaviour of the ratio of K_3/K_2 for quantum simulations for a temperature range starting in the classical regime and running down to $0\,K$. However since the number of imaginary time steps required for convergence increases as the temperature is lowered accurate, simulations as $T \to 0$ take ever longer to run.

Further extensions could include examining the effect of changing the density at which the simulations are performed. Care would need to be taken to check whether a physical phase transition from liquid to solid or vice versa occurs. Additionally, using the Tang-Toennies [32] potential, simulations for the same thermodynamic point could be performed for the differing rare gas elements. By using the Tang-Toennies potential differences in energies due to differing pair

potentials should be minimised.

Appendix A

Derivation of the Kinetic Energy Estimator

The kinetic energy estimator Eq. 2.9 and the normalised density matrix Eq. 2.89 are reproduced here for clarity,

$$E_{\text{kin}} = -\frac{\hbar^2}{2m}\sum_{i=1}^{N}\int[\nabla_i'^2 W(\boldsymbol{R},\boldsymbol{R}';\beta)](\boldsymbol{R}'=\boldsymbol{R})d\boldsymbol{R}, \tag{A.1}$$

$$\begin{aligned} W(\boldsymbol{R},\boldsymbol{R}';\beta) &= \frac{1}{\mathcal{I}(\beta)}\exp\left\{-\frac{m}{2\beta\hbar^2}(\boldsymbol{R}'-\boldsymbol{R})^2\right\} \\ &\quad\times\int\exp\left\{-\sum_{l=1}^{\infty}\left(\frac{\boldsymbol{a}_l}{\sqrt{2}\sigma_l}\right)^2-\beta\mathcal{V}(\boldsymbol{R},\boldsymbol{R}';\boldsymbol{A})\right\}\prod_{l=1}^{\infty}d\boldsymbol{a}_l. \end{aligned} \tag{A.2}$$

Consider

$$\begin{aligned} W^{\dagger}(\boldsymbol{R},\boldsymbol{R}';\beta) &= \frac{1}{\mathcal{I}(\beta)}\exp\left\{-\frac{m}{2\beta\hbar^2}(\boldsymbol{R}'-\boldsymbol{R})^2\right\} \\ &\quad\times\exp\left\{-\sum_{l=1}^{\infty}\left(\frac{\boldsymbol{a}_l}{\sqrt{2}\sigma_l}\right)^2-\beta\mathcal{V}(\boldsymbol{R},\boldsymbol{R}';\boldsymbol{A})\right\}. \end{aligned} \tag{A.3}$$

We can then apply the operator $\nabla_i'^2$ to this expression and obtain

$$\begin{aligned}\nabla_i' W^\dagger(\boldsymbol{R},\boldsymbol{R}';\beta) &= -\frac{m}{\beta\hbar^2}(\boldsymbol{R}'-\boldsymbol{R})W^\dagger(\boldsymbol{R},\boldsymbol{R}';\beta) \\ &\quad -\beta[\nabla'\mathcal{V}(\mathbf{R},\boldsymbol{R}';\boldsymbol{A})]W^\dagger(\boldsymbol{R},\boldsymbol{R}';\beta) \qquad \text{(A.4)}\end{aligned}$$

$$\begin{aligned}\nabla_i'^2 W^\dagger(\boldsymbol{R},\boldsymbol{R}';\beta) &= -\frac{m}{\beta\hbar^2}3NW^\dagger(\boldsymbol{R},\boldsymbol{R}';\beta) \\ &\quad +\left(\frac{m}{\beta\hbar^2}\right)^2(\boldsymbol{R}'-\boldsymbol{R})^2W^\dagger(\boldsymbol{R},\boldsymbol{R}';\beta) \\ &\quad +\frac{2m}{\hbar^2}(\boldsymbol{R}'-\boldsymbol{R})[\nabla'\mathcal{V}(\mathbf{R},\boldsymbol{R}';\boldsymbol{A})]W^\dagger(\boldsymbol{R},\boldsymbol{R}';\beta) \\ &\quad -\beta[\nabla'^2\mathcal{V}(\mathbf{R},\boldsymbol{R}';\boldsymbol{A})]W^\dagger(\boldsymbol{R},\boldsymbol{R}';\beta) \\ &\quad +\beta^2[\nabla'\mathcal{V}(\mathbf{R},\boldsymbol{R}';\boldsymbol{A})]^2W^\dagger(\boldsymbol{R},\boldsymbol{R}';\beta). \qquad \text{(A.5)}\end{aligned}$$

After setting $\boldsymbol{R}'=\boldsymbol{R}$ we are left with

$$\begin{aligned}&\nabla_i'^2 W^\dagger(\boldsymbol{R},\boldsymbol{R}';\beta)\,[\boldsymbol{R}'=\boldsymbol{R}] = \\ &\left\{-\frac{m}{\beta\hbar^2}3N-\beta[\nabla'^2\mathcal{V}(\mathbf{R},\boldsymbol{R}';\boldsymbol{A})](\boldsymbol{R}'=\boldsymbol{R})\right. \\ &\left.+\beta^2\left\{[\nabla'\mathcal{V}(\mathbf{R},\boldsymbol{R}';\boldsymbol{A})](\boldsymbol{R}'=\boldsymbol{R})\right\}^2\right\}\times\frac{1}{\mathcal{I}(\beta)}\exp\{-\beta\mathcal{V}(\boldsymbol{R},\boldsymbol{R};\boldsymbol{A})\}, \qquad \text{(A.6)}\end{aligned}$$

where

$$[\nabla'\mathcal{V}(\mathbf{R},\boldsymbol{R}';\boldsymbol{A})](\boldsymbol{R}'=\boldsymbol{R}) = \int_0^1 \eta\nabla_{\boldsymbol{R}_P^{[c]}(\eta;\boldsymbol{A}_L)}V\left(\boldsymbol{R}_P^{[c]}(\eta;\boldsymbol{A}_L)\right)d\eta \qquad \text{(A.7)}$$

and

$$[\nabla'^2\mathcal{V}(\mathbf{R},\boldsymbol{R}';\boldsymbol{A})](\boldsymbol{R}'=\boldsymbol{R}) = \int_0^1 \eta^2\nabla^2_{\boldsymbol{R}_P^{[c]}(\eta;\boldsymbol{A}_L)}V\left(\boldsymbol{R}_P^{[c]}(\eta;\boldsymbol{A}_L)\right)d\eta \qquad \text{(A.8)}$$

with

$$\boldsymbol{R}_P^{[c]}(\eta;\boldsymbol{A}_L) = \boldsymbol{R}+\sum_{l=1}^{\infty}\boldsymbol{a}_l\sin(l\pi\eta). \qquad \text{(A.9)}$$

Recalling Eq. 2.93 we introduce the notation

$$\langle \ldots \rangle_{\Xi} = \int \ldots \prod_{l=1}^{L} d\boldsymbol{a}_l d\boldsymbol{R}, \tag{A.10}$$

where we take the average w.r.t. to Ξ. Using this notation as well as the re-parametrisation $\eta \longrightarrow 1-\eta$ we obtain

$$\begin{aligned} E_{\text{kin}} &= N\frac{3}{2}k_B T + \frac{\beta\hbar^2}{2m}\frac{1}{\mathcal{I}(\beta)}\left\langle \int_0^1 (1-\eta)^2 \nabla^2_{\boldsymbol{R}_P^{[c]}(\eta;\boldsymbol{A}_L)} V\left(\boldsymbol{R}_P^{[c]}(\eta;\boldsymbol{A}_L)\right) d\eta \right\rangle_{\Xi} \\ &\quad -\frac{\beta^2\hbar^2}{2m}\frac{1}{\mathcal{I}(\beta)}\left\langle \left\{ \int_0^1 (1-\eta)\nabla_{\boldsymbol{R}_P^{[c]}(\eta;\boldsymbol{A}_L)} V\left(\boldsymbol{R}_P^{[c]}(\eta;\boldsymbol{A}_L)\right) d\eta \right\}^2 \right\rangle_{\Xi}. \end{aligned} \tag{A.11}$$

Rewriting Eq. 2.3 for the potential as

$$V(\boldsymbol{R}) = \sum_{i<j=1}^{N} v(r_{ij}) = \frac{1}{2}\sum_{i,j=1}^{N}(1-\delta_{ij})v(r_{ij}), \tag{A.12}$$

where r_{ij} has the usual meaning $r_{ij} = |\boldsymbol{r}_i - \boldsymbol{r}_j|$, allows us to cast the potential for the closed paths in the form

$$V\left(\boldsymbol{R}_P^{[c]}(\eta;\boldsymbol{A}_L)\right) = \frac{1}{2}\sum_{i,j=1}^{N}(1-\delta_{ij})v\left(|\boldsymbol{r}_{P,i}^{[c]}(\eta;\boldsymbol{A}_L) - \boldsymbol{r}_{P,j}^{[c]}(\eta;\boldsymbol{A}_L)|\right). \tag{A.13}$$

The $3N$-dimensional differentiations in Eq. A.11 are defined as

$$\nabla^2_{\boldsymbol{R}_P^{[c]}(\eta;\boldsymbol{A}_L)} = \sum_{k=1}^{N} \nabla^2_{\boldsymbol{r}_{P,k}^{[c]}(\eta;\boldsymbol{A}_L)}, \tag{A.14}$$

$$\begin{aligned} &\left\{ \int_0^1 (1-\eta)\nabla_{\boldsymbol{R}_P^{[c]}(\eta;\boldsymbol{A}_L)} V\left(\boldsymbol{R}_P^{[c]}(\eta;\boldsymbol{A}_L)\right) d\eta \right\}^2 = \\ &\quad \sum_{k=1}^{N} \left\{ \int_0^1 (1-\eta)\nabla_{\boldsymbol{r}_{P,k}^{[c]}(\eta;\boldsymbol{A}_L)} V\left(\boldsymbol{R}_P^{[c]}(\eta;\boldsymbol{A}_L)\right) d\eta \right\}^2. \end{aligned} \tag{A.15}$$

Taking each in turn we find that

$$\begin{aligned}
&\nabla^2_{\boldsymbol{R}_P^{[c]}(\eta;\boldsymbol{A}_L)} V\left(\boldsymbol{R}_P^{[c]}(\eta;\boldsymbol{A}_L)\right) \\
&= \frac{1}{2}\sum_{i=1}^{N}\sum_{j=1}^{N}(1-\delta_{ij})\sum_{k=1}^{N}\nabla^2_{\boldsymbol{r}_{P,k}^{[c]}(\eta;\boldsymbol{A}_L)} v\left(|\boldsymbol{r}_{P,i}^{[c]}(\eta;\boldsymbol{A}_L)-\boldsymbol{r}_{P,j}^{[c]}(\eta;\boldsymbol{A}_L)|\right) \\
&= \frac{1}{2}\sum_{i=1}^{N}\sum_{j=1}^{N}(1-\delta_{ij})\nabla^2_{\boldsymbol{r}_{P,i}^{[c]}(\eta;\boldsymbol{A}_L)} v\left(|\boldsymbol{r}_{P,i}^{[c]}(\eta;\boldsymbol{A}_L)-\boldsymbol{r}_{P,j}^{[c]}(\eta;\boldsymbol{A}_L)|\right) \\
&\quad +\frac{1}{2}\sum_{i=1}^{N}\sum_{j=1}^{N}(1-\delta_{ij})\nabla^2_{\boldsymbol{r}_{P,j}^{[c]}(\eta;\boldsymbol{A}_L)} v\left(|\boldsymbol{r}_{P,i}^{[c]}(\eta;\boldsymbol{A}_L)-\boldsymbol{r}_{P,j}^{[c]}(\eta;\boldsymbol{A}_L)|\right).
\end{aligned} \tag{A.16}$$

The derivatives with respect to particle labels i and j yield the same result

$$\begin{aligned}
\nabla_1^2 v\left(|\boldsymbol{r}_1-\boldsymbol{r}_2|\right) &= \nabla_1\left(\frac{\boldsymbol{r}_1-\boldsymbol{r}_2}{|\boldsymbol{r}_1-\boldsymbol{r}_2|}v'\left(|\boldsymbol{r}_1-\boldsymbol{r}_2|\right)\right) \\
&= v''\left(|\boldsymbol{r}_1-\boldsymbol{r}_2|\right)+v'\left(|\boldsymbol{r}_1-\boldsymbol{r}_2|\right)\left(\frac{3}{|\boldsymbol{r}_1-\boldsymbol{r}_2|}-\frac{(\boldsymbol{r}_1-\boldsymbol{r}_2)^2}{|\boldsymbol{r}_1-\boldsymbol{r}_2|^3}\right) \\
&= 2\frac{v'\left(|\boldsymbol{r}_1-\boldsymbol{r}_2|\right)}{|\boldsymbol{r}_1-\boldsymbol{r}_2|}+v''\left(|\boldsymbol{r}_1-\boldsymbol{r}_2|\right).
\end{aligned} \tag{A.17}$$

Returning to Eq. (A.15) we find

$$\begin{aligned}
&\nabla_{\boldsymbol{r}_{P,k}^{[c]}(\eta;\boldsymbol{A}_L)} V\left(\boldsymbol{R}_P^{[c]}(\eta;\boldsymbol{A}_L)\right) \\
&= \frac{1}{2}\sum_{i,j=1}^{N}(1-\delta_{ij})\nabla_{\boldsymbol{r}_{P,k}^{[c]}(\eta;\boldsymbol{A}_L)} v\left(|\boldsymbol{r}_{P,i}^{[c]}(\eta;\boldsymbol{A}_L)-\boldsymbol{r}_{P,j}^{[c]}(\eta;\boldsymbol{A}_L)|\right) \\
&= \frac{1}{2}\sum_{j=1}^{N}(1-\delta_{kj})\nabla_{\boldsymbol{r}_{P,k}^{[c]}(\eta;\boldsymbol{A}_L)} v\left(|\boldsymbol{r}_{P,k}^{[c]}(\eta;\boldsymbol{A}_L)-\boldsymbol{r}_{P,j}^{[c]}(\eta;\boldsymbol{A}_L)|\right) \\
&\quad +\frac{1}{2}\sum_{i=1}^{N}(1-\delta_{ik})\nabla_{\boldsymbol{r}_{P,k}^{[c]}(\eta;\boldsymbol{A}_L)} v\left(|\boldsymbol{r}_{P,i}^{[c]}(\eta;\boldsymbol{A}_L)-\boldsymbol{r}_{P,k}^{[c]}(\eta;\boldsymbol{A}_L)|\right) \\
&= \sum_{i=1}^{N}(1-\delta_{ik})\frac{\boldsymbol{r}_{P,k}^{[c]}(\eta;\boldsymbol{A}_L)-\boldsymbol{r}_{P,i}^{[c]}(\eta;\boldsymbol{A}_L)}{|\boldsymbol{r}_{P,i}^{[c]}(\eta;\boldsymbol{A}_L)-\boldsymbol{r}_{P,k}^{[c]}(\eta;\boldsymbol{A}_L)|}v'\left(|\boldsymbol{r}_{P,i}^{[c]}(\eta;\boldsymbol{A}_L)-\boldsymbol{r}_{P,k}^{[c]}(\eta;\boldsymbol{A}_L)|\right).
\end{aligned} \tag{A.18}$$

Inserting the results from Eqs. A.17 and A.18 into Eq. A.11 we obtain

$$
\begin{aligned}
E_{\text{kin}} =& N\frac{3}{2}k_BT + \frac{\beta\hbar^2}{2m}\frac{1}{\mathcal{I}(\beta)}\left\langle \sum_{i,j=1}^{N}(1-\delta_{ij})\int_0^1 (1-\eta)^2 v_{gg}\left(r_{P,ij}^{[c]}(\eta;\boldsymbol{A}_L)\right)d\eta \right\rangle_{\Xi} \\
& - \frac{\beta^2\hbar^2}{2m}\frac{1}{\mathcal{I}(\beta)} \\
& \times \left\langle \sum_{j=1}^{N}\left\{ \sum_{i=1}^{N}(1-\delta_{ij})\int_0^1 (1-\eta)\frac{\boldsymbol{r}_{P,ij}^{[c]}(\eta;\boldsymbol{A}_L)}{r_{P,ij}^{[c]}(\eta;\boldsymbol{A}_L)} v'\left(r_{P,ij}^{[c]}(\eta;\boldsymbol{A}_L)\right)\right\}^2 \right\rangle_{\Xi},
\end{aligned}
\tag{A.19}
$$

where in the second term we have introduced

$$
v_{gg}\left(r_{P,ij}^{[c]}(\eta;\boldsymbol{A}_L)\right) = 2\frac{v'\left(r_{P,ij}^{[c]}(\eta;\boldsymbol{A}_L)\right)}{r_{P,ij}^{[c]}(\eta;\boldsymbol{A}_L)} + v''\left(r_{P,ij}^{[c]}(\eta;\boldsymbol{A}_L)\right). \tag{A.20}
$$

We have also used the following notation for simplicity

$$
\boldsymbol{r}_{P,ij}^{[c]}(\eta;\boldsymbol{A}_L) = \boldsymbol{r}_{P,i}^{[c]}(\eta;\boldsymbol{A}_L) - \boldsymbol{r}_{P,j}^{[c]}(\eta;\boldsymbol{A}_L), \tag{A.21}
$$

$$
r_{P,ij}^{[c]}(\eta;\boldsymbol{A}_L) = |\boldsymbol{r}_{P,i}^{[c]}(\eta;\boldsymbol{A}_L) - \boldsymbol{r}_{P,j}^{[c]}(\eta;\boldsymbol{A}_L)|, \tag{A.22}
$$

$$
\boldsymbol{r}_{P,i}^{[c]}(\eta;\boldsymbol{A}_l) = \boldsymbol{r}_i + \sum_{l=1}^{L}\boldsymbol{a}_{l,i}\sin(l\pi\eta). \tag{A.23}
$$

Appendix B

Calculation of r_{limit}

The value of r_{limit} is given by the shortest vector from the origin to a boundary plane. It is obvious that this vector will be normal to the boundary plane of the simulation cell. Choosing the boundary plane as that spanned by $\boldsymbol{a}_1$ and $\boldsymbol{a}_2$ the normal $\boldsymbol{n}_{12}$ is given by,

$$\boldsymbol{n}_{12} = \frac{\boldsymbol{a}_1 \times \boldsymbol{a}_2}{|\boldsymbol{a}_1 \times \boldsymbol{a}_2|} = \frac{1}{\sqrt{3}} \begin{pmatrix} -1 \\ -1 \\ 1 \end{pmatrix} \tag{B.1}$$

and the boundary plane $\boldsymbol{r}_p$ by ,

$$\begin{aligned} \boldsymbol{r}_p &= \alpha L \boldsymbol{a}_1 + \beta L \boldsymbol{a}_2 + L(\boldsymbol{a}_1 + \boldsymbol{a}_2 + \boldsymbol{a}_3) \\ &= \frac{La}{2} \begin{pmatrix} 2+\alpha+\beta \\ -2-\alpha \\ 2+\beta \end{pmatrix}, \end{aligned} \tag{B.2}$$

where $2L$ is the number of primitive cells along each of the directions $\boldsymbol{a}_1$, $\boldsymbol{a}_2$ and $\boldsymbol{a}_3$. The vector $\boldsymbol{r}_{limit}$ can be written as $\gamma \boldsymbol{n}_{12}$. Setting this equal to Eq. B.2 we can solve for γ yielding

$$\frac{\gamma}{\sqrt{3}} \begin{pmatrix} -1 \\ -1 \\ 1 \end{pmatrix} = \frac{La}{2} \begin{pmatrix} 2+\alpha+\beta \\ -2-\alpha \\ 2+\beta \end{pmatrix}. \tag{B.3}$$

This leads to three simultaneous equations

$$-\frac{\gamma}{\sqrt{3}} = \frac{La}{2}(2+\alpha+\beta), \tag{B.4}$$

$$-\frac{\gamma}{\sqrt{3}} = \frac{La}{2}(-2-\alpha), \tag{B.5}$$

$$\frac{\gamma}{\sqrt{3}} = \frac{La}{2}(2+\beta). \tag{B.6}$$

Solving gives

$$\gamma = \frac{La}{\sqrt{3}} \tag{B.7}$$

from which we find

$$r_{limit} = |\boldsymbol{r}_{limit}| = \gamma |\boldsymbol{n}_{12}| = \frac{La}{3} \left| \begin{pmatrix} -1 \\ -1 \\ 1 \end{pmatrix} \right| = \frac{La}{\sqrt{3}}. \tag{B.8}$$

Appendix C

Random Number Generators

C.1 Background

Knuth [24] states that any discussion about random numbers invariably has to address what is meant by a random number. It is proposed that the definition of a random number is irrelevant since what we require is not a single random number but a sequence of independent numbers conforming to a given distribution that could have been generated by a chance process [24]. Any number in the sequence should be independent of all others, thus if we consider a uniform distribution of random digits the probability of a digit being a 1 is $\frac{1}{10}$, regardless of the values of the other digits in the sequence.

Early sequences of random numbers were often generated by picking balls out of a well stirred urn, or from dice rolls [24]. Various tables of random numbers were produced and a range of machines were built to generate sequences

using electrical noise [1]. These methods were not ideal for use with computers. Early computers had limited memory - so storing large tables of random numbers was prohibitive. The advantage of using tables was that a simulation could be repeated exactly with the same sequence of random numbers enabling accurate testing of simulations. The ability to repeat a sequence of random numbers in subsequent simulations was not possible for mechanically generated random numbers. Mechanical generators were often slow and could suffer from faults that were not easy to detect [24].

The problems of the above methods led to research into generating numbers from within a computer program [24]. The idea of using a deterministic algorithm to generate a sequence of random numbers may seem perverse. If a sequence is governed by a set of equations, however complex, it cannot be said to be random. The solution is to realise that what we want is not necessarily a random sequence but a sequence that when subjected to a range of tests appears to be random. Thus computer-based random number generators can be said to be pseudo-random number generators or prn generators.

C.2 Testing Generators

There is a variety of statistical tests that can be applied to a sequence of random numbers. The tests are not a definitive guide as to whether a prn generator is random or not, but a guide as to how a given sequence compares to a truly

random sequence. This rather vague definition will become clearer later.

The basis of several tests is the Chi-square test. Assume our prn generator gives numbers with a uniform distribution between zero and one. The probability, p_s, of a given number falling in a range characterised by x is given by $p_s = \delta$, where $i\delta \leq x < (i+1)\delta$, where i is an integer such that $0 \leq i < S$ and $\delta = 1/S$. Thus if we take N numbers from our sequence and sort them into S bins the expected number in each bin would be Np_s. We would be very surprised if when performing this test the number found in each bin, Y_s, were equal to the expected number, Np_s. To see how far our actual distribution is from a perfect normal distribution one could calculate the square of the differences between expected and actual numbers in each bin

$$V = \sum_{s=1}^{S} (Y_s - Np_s)^2. \tag{C.1}$$

To gain an understanding of what constitutes a good value of V the value can be compared with values for a Chi-square distribution with $S-1$ degrees of freedom. We use $S-1$ since if we know the number of trials and the number in all but one bins the number in the last bin is also known. Comparing our value of V with the Chi-square distribution will give us an approximate probability for obtaining a value less than or equal to V. We may deem the results suspect if the value of V lies in either the lowest or highest 5% of the distribution. It is wise to perform the test several times on different parts of the sequence so as to gain an idea of whether the generator consistently gives overly large or small values of V.

This is very important as any local or short-range fluctuations in the distribution will potentially be smoothed out for large numbers of trials. The Chi-square distribution is not exact but holds in the limit of large N. Knuth states that as a rule of thumb one should aim for the expected number in a bin to be ≥ 5.

The above method can be extended to look for correlations between neighbouring pairs, triplets and higher order groups. Considering the case for pairs we can imagine that the two numbers q, r, represent a coordinate in an x, y plane. As before the numbers lie in the range $0 \leq q, r < 1$. Dividing each axis into S bins we find that we now have S^2 possible outcomes and a Chi-square test can be run for a system of $S^2 - 1$ degrees of freedom. It is simple to see how this example can be extended to triplets and high-order terms.

Another test that can be applied to generators is the run-up/down test. In this we look for sequences of continually ascending or descending numbers.

C.3 Results for Generator used in Simulations

In this work we have used the intrinsic Fortran function *Random_Number* to generate our sequence of random numbers, which has a stated period in excess of 2^{123} [29]. We have applied a range of tests to the random number generator. The first test we applied was the Chi-square test for a uniform distribution. The test was performed using 100 bins and a range of N. Each test was performed 10 times. In Table C.1 we present the values of the Chi-square distribution for

Percentage Points	$S-1=99$	$S-1=9999$	$S-1=999999$
1%	69.167	9672.457	996706.837
5%	77.050	9768.207	997680.817
25%	89.152	9903.323	999045.457
50%	98.333	9998.333	999998.333
75%	108.120	10093.949	1000951.816
95%	123.203	10232.046	1002319.435
99%	134.739	10331.448	1003297.069

Table C.1: Values of the Chi-square distribution.

various degrees of freedom and for a range of percentage points. Table C.2 gives the results of the tests.

We see that none of our results lie in the top or bottom 1% and that only two results are in the top 5% and one in the bottom 5%. Tables C.3 and C.4 show results for pairs and triplets of numbers with 9999 and 999999 degrees of freedom, respectively. We again find that there is no reason for concern from these results.

$N = 10^3$	$N = 10^4$	$N = 10^5$	$N = 10^6$	$N = 10^7$
117.698	119.190	90.645	97.524	79.027
108.518	123.012	106.611	110.621	88.467
77.109	99.812	91.657	87.206	88.768
110.677	124.770	95.007	104.225	88.293
86.911	121.132	92.383	101.865	117.830
119.887	77.192	126.559	99.897	108.786
115.320	104.488	72.081	97.424	87.531
87.315	101.410	112.977	86.902	104.747
85.287	105.890	113.609	81.571	116.048
78.085	97.951	102.067	83.313	81.996

Table C.2: Results for equidistribution test, $S = 100$.

$N = 10^5$	$N = 10^6$	$N = 10^7$	$N = 10^8$
10086.200	9780.468	10060.129	10263.660
10221.520	10159.768	9913.288	9971.971
9992.560	10028.084	9823.239	9774.752
10166.760	9738.988	10004.241	10039.389
9858.880	10067.624	9792.770	9883.390
10032.560	10151.454	10078.918	9854.100
9893.700	10014.748	9911.363	10002.004
9917.680	10277.980	10006.192	9865.168
10046.860	10130.630	9968.404	10017.355
10099.540	10160.420	9794.902	10081.850

Table C.3: Results for pair test, $S = 100$.

$N = 10^7$	$N = 10^8$	$N = 10^9$	$N = 10^{10}$
998677.400	1000751.360	1000382.466	999830.357
1000065.200	1002248.260	1001454.060	1002062.636
998884.400	998845.720	1000186.832	999451.892
999306.000	999974.440	999011.770	1000821.573
999055.200	999975.220	1000462.778	1001114.548
1000741.800	1000314.960	998836.722	999144.409
999852.800	999853.980	1001937.772	1001235.220
1001161.000	1000066.520	999226.056	999762.387
1002605.200	10001470900	998165.354	1001258.969
1000345.800	998874.920	1000182.846	1000418.725

Table C.4: Results for triplet test, $S = 100$.

Appendix D

O_h Point Group Symmetry Operators

In this section we shall list all the relevant point group rotation matrices for the FCC point group as well as give details of the Laue classes for the six classes of high-symmetry vectors discussed in Section 2.7.2.

An important consideration is the orientation of our reference frame. It is the standard in crystallography to define a right-handed coordinate frame with x out of the page towards the viewer, y pointing to the right and z in the vertical direction, as shown in Fig. D.1(a). We employ a physics frame which again is right-handed but now x points to the right, y out of the page away from the viewer and z again in the vertical direction, Fig. D.1(b). The two sets of axis are

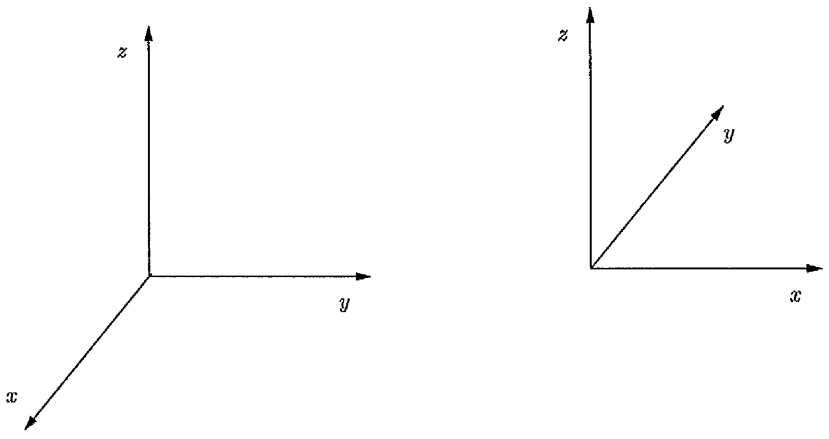

(a) Crystallographic (b) Physics

Figure D.1: Coordinate reference frames.

related thus,

$$(x, y, z) = (y_c, -x_c, z_c) \tag{D.1}$$

where c denotes the crystallographic frame. For a general vector we have the relation

$$\boldsymbol{r} = \begin{pmatrix} 0 & 1 & 0 \\ -1 & 0 & 0 \\ 0 & 0 & 1 \end{pmatrix} \boldsymbol{r}_c = R_0^T \boldsymbol{r}_c. \tag{D.2}$$

The importance of the above relation is that it enables us to express a crystallo-

graphic rotation R_c, in our reference frame

$$\boldsymbol{r}'_c = R_c \boldsymbol{r}_c \tag{D.3}$$

$$R_0 \boldsymbol{r}' = R_c R_0 \boldsymbol{r} \tag{D.4}$$

$$\boldsymbol{r}' = R_0^T R_c R_0 \boldsymbol{r} = R\boldsymbol{r}. \tag{D.5}$$

Equation D.5 gives us a prescription by which we can generate the rotation matrices for the FCC point group in our reference frame from the same rotation matrices but given in the crystallographic reference frame and more importantly given in the standard tables [7].

Table D.1 lists all the rotations of the FCC point group in our reference frame. It is useful to note that the matrix for all even rotations R_n is minus the matrix of the previous rotation $-R_{n-1}$ (for the order listed here).

In Tables D.2 to D.7 we give the multiplicity, $M(\boldsymbol{K})$, and the degeneracy, $g_0(\boldsymbol{K})$, of each of the high-symmetry $\boldsymbol{K}$-vectors and the subsets of symmetry-equivalent representatives containing those rotations that produce identical vectors. The effect of applying a single rotation from each subset to the high-symmetry $\boldsymbol{K}$-vector is to reproduce all symmetry-equivalent $\boldsymbol{K}$-vectors of that type.

Index	Direction	Schoenflies symbol	Rotation matrix	Comments
1	$(0,0,0)$	E	$\begin{pmatrix} 1 & 0 & 0 \\ 0 & 1 & 0 \\ 0 & 0 & 1 \end{pmatrix}$	Identity
2	$(0,0,0)$	I	$\begin{pmatrix} -1 & 0 & 0 \\ 0 & -1 & 0 \\ 0 & 0 & -1 \end{pmatrix}$	Inversion
3	$(0,-1,0)$	C_{2y}	$\begin{pmatrix} -1 & 0 & 0 \\ 0 & 1 & 0 \\ 0 & 0 & -1 \end{pmatrix}$	180° about $(0,1,0)$

Continued on next page

Index	Direction	Schoenflies symbol	Rotation matrix	Comments
4	$(0,-1,0)$	σ_y	$\begin{pmatrix} 1 & 0 & 0 \\ 0 & -1 & 0 \\ 0 & 0 & 1 \end{pmatrix}$	Reflection across xz plane
5	$(0,-1,0)$	C_{4y}^{-}	$\begin{pmatrix} 0 & 0 & 1 \\ 0 & 1 & 0 \\ -1 & 0 & 0 \end{pmatrix}$	$-90°$ about $(0,1,0)$
6	$(0,-1,0)$	$S_{4y}^{+} = IC_{4y}^{-}$	$\begin{pmatrix} 0 & 0 & -1 \\ 0 & -1 & 0 \\ 1 & 0 & 0 \end{pmatrix}$	$-90°$ about $(0,1,0)$ then inversion

Continued on next page

Index	Direction	Schoenflies symbol	Rotation matrix	Comments
7	$(0,-1,0)$	C_{4y}^{+}	$\begin{pmatrix} 0 & 0 & -1 \\ 0 & 1 & 0 \\ 1 & 0 & 0 \end{pmatrix}$	90° about $(0,1,0)$
8	$(0,-1,0)$	$S_{4y}^{-} = IC_{4y}^{+}$	$\begin{pmatrix} 0 & 0 & 1 \\ 0 & -1 & 0 \\ -1 & 0 & 0 \end{pmatrix}$	90° about $(0,1,0)$ then inversion
9	$(1,0,0)$	C_{2x}	$\begin{pmatrix} 1 & 0 & 0 \\ 0 & -1 & 0 \\ 0 & 0 & -1 \end{pmatrix}$	180° about $(1,0,0)$

Continued on next page

Index	Direction	Schoenflies symbol	Rotation matrix	Comments
10	$(1,0,0)$	σ_x	$\begin{pmatrix} -1 & 0 & 0 \\ 0 & 1 & 0 \\ 0 & 0 & 1 \end{pmatrix}$	Reflection across yz plane
11	$(1,0,0)$	C_{4x}^{+}	$\begin{pmatrix} 1 & 0 & 0 \\ 0 & 0 & 1 \\ 0 & -1 & 0 \end{pmatrix}$	90° about $(1,0,0)$
12	$(1,0,0)$	$S_{4x}^{-} = IC_{4x}^{+}$	$\begin{pmatrix} -1 & 0 & 0 \\ 0 & 0 & -1 \\ 0 & 1 & 0 \end{pmatrix}$	90° about $(1,0,0)$ then inversion

Continued on next page

Index	Direction	Schoenflies symbol	Rotation matrix	Comments
13	$(1,0,0)$	C_{4x}^{-}	$\begin{pmatrix} 1 & 0 & 0 \\ 0 & 0 & -1 \\ 0 & 1 & 0 \end{pmatrix}$	$-90°$ about $(1,0,0)$
14	$(1,0,0)$	$S_{4x}^{+} = IC_{4x}^{-}$	$\begin{pmatrix} -1 & 0 & 0 \\ 0 & 0 & 1 \\ 0 & -1 & 0 \end{pmatrix}$	$-90°$ about $(1,0,0)$ then inversion
15	$(0,0,1)$	C_{2z}	$\begin{pmatrix} -1 & 0 & 0 \\ 0 & -1 & 0 \\ 0 & & 1 \end{pmatrix}$	$180°$ about $(0,0,1)$

Continued on next page

Index	Direction	Schoenflies symbol	Rotation matrix	Comments
16	$(0,0,1)$	σ_z	$\begin{pmatrix} 1 & 0 & 0 \\ 0 & 1 & 0 \\ 0 & 0 & -1 \end{pmatrix}$	Reflection across xy plane
17	$(0,0,1)$	C_{4z}^{+}	$\begin{pmatrix} 0 & -1 & 0 \\ 1 & 0 & 0 \\ 0 & 0 & 1 \end{pmatrix}$	90° about $(0,0,1)$
18	$(0,0,1)$	$S_{4z}^{-} = IC_{4z}^{+}$	$\begin{pmatrix} 0 & 1 & 0 \\ -1 & 0 & 0 \\ 0 & 0 & -1 \end{pmatrix}$	90° about $(0,0,1)$ then inversion

Continued on next page

Index	Direction	Schoenflies symbol	Rotation matrix	Comments
19	$(0,0,1)$	C_{4z}^{-}	$\begin{pmatrix} 0 & 1 & 0 \\ -1 & 0 & 0 \\ 0 & 0 & 1 \end{pmatrix}$	$-90°$ about $(0,0,1)$
20	$(0,0,1)$	$S_{4z}^{+} = IC_{4z}^{-}$	$\begin{pmatrix} 0 & -1 & 0 \\ 1 & 0 & 0 \\ 0 & 0 & -1 \end{pmatrix}$	$-90°$ about $(0,0,1)$ then inversion
21	$(1,-1,0)$	C_{2b}'	$\begin{pmatrix} 0 & -1 & 0 \\ -1 & 0 & 0 \\ 0 & 0 & -1 \end{pmatrix}$	$180°$ about $(-1,1,0)$

Continued on next page

Index	Direction	Schoenflies symbol	Rotation matrix	Comments
22	$(1,-1,0)$	σ_{d2}	$\begin{pmatrix} 0 & 1 & 0 \\ 1 & 0 & 0 \\ 0 & 0 & 1 \end{pmatrix}$	Reflection across plane $\perp (-1,1,0)$
23	$(0,-1,1)$	C'_{2f}	$\begin{pmatrix} -1 & 0 & 0 \\ 0 & 0 & -1 \\ 0 & -1 & 0 \end{pmatrix}$	180° about $(0,-1,1)$
24	$(0,-1,1)$	σ_{d6}	$\begin{pmatrix} 1 & 0 & 0 \\ 0 & 0 & 1 \\ 0 & 1 & 0 \end{pmatrix}$	Reflection across plane $\perp (0,-1,1)$

Continued on next page

Index	Direction	Schoenflies symbol	Rotation matrix	Comments
25	$(1,0,1)$	C'_{2c}	$\begin{pmatrix} 0 & 0 & 1 \\ 0 & -1 & 0 \\ 1 & 0 & 0 \end{pmatrix}$	180° about $(1,0,1)$
26	$(1,0,1)$	σ_{d3}	$\begin{pmatrix} 0 & 0 & -1 \\ 0 & 1 & 0 \\ -1 & 0 & 0 \end{pmatrix}$	Reflection across plane $\perp (1,0,1)$
27	$(-1,-1,0)$	C'_{2a}	$\begin{pmatrix} 0 & 1 & 0 \\ 1 & 0 & 0 \\ 0 & 0 & -1 \end{pmatrix}$	180° about $(1,1,0)$

Continued on next page

Index	Direction	Schoenflies symbol	Rotation matrix	Comments
28	$(-1,-1,0)$	σ_{d1}	$\begin{pmatrix} 0 & -1 & 0 \\ -1 & 0 & 0 \\ 0 & 0 & 1 \end{pmatrix}$	Reflection across plane $\perp (1,1,0)$
29	$(0,1,1)$	C'_{2d}	$\begin{pmatrix} -1 & 0 & 0 \\ 0 & 0 & 1 \\ 0 & 1 & 0 \end{pmatrix}$	180° about $(0,-1,-1)$
30	$(0,1,1)$	σ_{d4}	$\begin{pmatrix} 1 & 0 & 0 \\ 0 & 0 & -1 \\ 0 & -1 & 0 \end{pmatrix}$	Reflection across plane $\perp (0,-1,-1)$

Continued on next page

Index	Direction	Schoenflies symbol	Rotation matrix	Comments
31	$(1,0,-1)$	C'_{2e}	$\begin{pmatrix} 0 & 0 & -1 \\ 0 & -1 & 0 \\ -1 & 0 & 0 \end{pmatrix}$	180° about $(1,0,-1)$
32	$(1,0,-1)$	σ_{d5}	$\begin{pmatrix} 0 & 0 & 1 \\ 0 & 1 & 0 \\ 1 & 0 & 0 \end{pmatrix}$	Reflection across plane $\perp (1,0,-1)$
33	$(1,-1,-1)$	C_{34}^{-}	$\begin{pmatrix} 0 & -1 & 0 \\ 0 & 0 & -1 \\ 1 & 0 & 0 \end{pmatrix}$	$-120°$ about $(-1,1,-1)$

Continued on next page

Index	Direction	Schoenflies symbol	Rotation matrix	Comments
34	$(1,-1,-1)$	$S_{64}^{+} = IC_{34}^{-}$	$\begin{pmatrix} 0 & 1 & 0 \\ 0 & 0 & 1 \\ -1 & 0 & 0 \end{pmatrix}$	$-120°$ about $(-1,1,-1)$ then inversion
35	$(1,0,-1)$	C_{34}^{+}	$\begin{pmatrix} 0 & 0 & 1 \\ -1 & 0 & 0 \\ 0 & -1 & 0 \end{pmatrix}$	$120°$ about $(-1,1,-1)$
36	$(1,0,-1)$	$S_{64}^{-} = IC_{34}^{+}$	$\begin{pmatrix} 0 & 0 & -1 \\ 1 & 0 & 0 \\ 0 & 1 & 0 \end{pmatrix}$	$120°$ about $(-1,1,-1)$ then inversion

Continued on next page

Index	Direction	Schoenflies symbol	Rotation matrix	Comments
37	$(1,1,1)$	C_{31}^{+}	$\begin{pmatrix} 0 & 0 & 1 \\ 1 & 0 & 0 \\ 0 & 1 & 0 \end{pmatrix}$	120° about $(1,1,1)$
38	$(1,1,1)$	$S_{61}^{-} = IC_{31}^{+}$	$\begin{pmatrix} 0 & 0 & -1 \\ -1 & 0 & 0 \\ 0 & -1 & 0 \end{pmatrix}$	120° about $(1,1,1)$ then inversion
39	$(1,0,-1)$	C_{31}^{-}	$\begin{pmatrix} 0 & 1 & 0 \\ 0 & 0 & 1 \\ 1 & 0 & 0 \end{pmatrix}$	$-120°$ about $(1,1,1)$

Continued on next page

Index	Direction	Schoenflies symbol	Rotation matrix	Comments
40	$(1,0,-1)$	$S_{61}^{+} = IC_{31}^{-}$	$\begin{pmatrix} 0 & -1 & 0 \\ 0 & 0 & -1 \\ -1 & 0 & 0 \end{pmatrix}$	$-120°$ about $(1,1,1)$ then inversion
41	$(-1,-1,1)$	C_{32}^{+}	$\begin{pmatrix} 0 & 0 & -1 \\ 1 & 0 & 0 \\ 0 & -1 & 0 \end{pmatrix}$	$120°$ about $(-1,-1,1)$
42	$(-1,-1,1)$	$S_{62}^{-} = IC_{32}^{+}$	$\begin{pmatrix} 0 & 0 & 1 \\ -1 & 0 & 0 \\ 0 & 1 & 0 \end{pmatrix}$	$120°$ about $(-1,-1,1)$ then inversion

Continued on next page

Index	Direction	Schoenflies symbol	Rotation matrix	Comments
43	$(1,0,-1)$	C_{32}^{-}	$\begin{pmatrix} 0 & 1 & 0 \\ 0 & 0 & -1 \\ -1 & 0 & 0 \end{pmatrix}$	$-120°$ about $(-1,-1,1)$
44	$(1,0,-1)$	$S_{62}^{+} = IC_{32}^{-}$	$\begin{pmatrix} 0 & -1 & 0 \\ 0 & 0 & 1 \\ 1 & 0 & 0 \end{pmatrix}$	$-120°$ about $(-1,-1,1)$ then inversion
45	$(1,-1,-1)$	C_{33}^{+}	$\begin{pmatrix} 0 & 0 & -1 \\ -1 & 0 & 0 \\ 0 & 1 & 0 \end{pmatrix}$	$120°$ about $(1,-1,-1)$

Continued on next page

Index	Direction	Schoenflies symbol	Rotation matrix	Comments
46	$(1,-1,-1)$	$S_{63}^{-} = IC_{33}^{+}$	$\begin{pmatrix} 0 & 0 & 1 \\ 1 & 0 & 0 \\ 0 & -1 & 0 \end{pmatrix}$	120° about $(1,-1,-1)$ then inversion
47	$(1,-1,-1)$	C_{33}^{-}	$\begin{pmatrix} 0 & -1 & 0 \\ 0 & 0 & 1 \\ -1 & 0 & 0 \end{pmatrix}$	$-120°$ about $(1,-1,-1)$
48	$(1,-1,-1)$	$S_{63}^{+} = IC_{33}^{-}$	$\begin{pmatrix} 0 & 1 & 0 \\ 0 & 0 & -1 \\ 1 & 0 & 0 \end{pmatrix}$	$-120°$ about $(1,-1,-1)$ then inversion

Table D.1: The rotations of the FCC point group.

$\boldsymbol{K}_1$, $M(\boldsymbol{K}) = 12, g_0(\boldsymbol{k}) = 4$	
$\{1, 16, 21, 28\}$	$\{2, 15, 22, 27\}$
$\{3, 10, 18, 19\}$	$\{4, 9, 17, 20\}$
$\{5, 26, 42, 45\}$	$\{6, 25, 41, 46\}$
$\{7, 32, 35, 38\}$	$\{8, 31, 36, 37\}$
$\{11, 30, 33, 44\}$	$\{12, 29, 34, 43\}$
$\{13, 24, 40, 47\}$	$\{14, 23, 39, 48\}$

Table D.2: Symmetry-equivalent representatives for $\boldsymbol{K}_1$-vectors.

$\boldsymbol{K}_2$, $M(\boldsymbol{K}) = 8, g_0(\boldsymbol{K}) = 6$	
$\{1, 28, 30, 32, 33, 35\}$	$\{2, 27, 29, 31, 34, 36\}$
$\{3, 12, 18, 26, 43, 45\}$	$\{4, 11, 17, 25, 44, 46\}$
$\{5, 13, 16, 21, 40, 42\}$	$\{6, 14, 15, 22, 39, 41\}$
$\{7, 10, 19, 23, 38, 48\}$	$\{8, 9, 20, 24, 37, 47\}$

Table D.3: Symmetry-equivalent representatives for $\boldsymbol{K}_2$-vectors.

$\boldsymbol{K}_3$, $M(\boldsymbol{K}) = 6, g_0(\boldsymbol{K}) = 8$	
$\{1, 4, 9, 11, 13, 16, 24, 30\}$	$\{2, 3, 10, 12, 14, 15, 23, 29\}$
$\{5, 8, 26, 31, 34, 40, 43, 47\}$	$\{6, 7, 25, 32, 33, 39, 44, 48\}$
$\{17, 20, 22, 27, 36, 37, 41, 46\}$	$\{18, 19, 21, 28, 35, 38, 42, 45\}$

Table D.4: Symmetry-equivalent representatives for $\boldsymbol{K}_3$-vectors.

$\boldsymbol{K}_4$, $M(\boldsymbol{K}) = 24, g_0(\boldsymbol{K}) = 2$	
$\{1, 28\}$	$\{2, 27\}$
$\{3, 18\}$	$\{4, 17\}$
$\{5, 42\}$	$\{6, 41\}$
$\{7, 38\}$	$\{8, 37\}$
$\{9, 20\}$	$\{10, 19\}$
$\{11, 44\}$	$\{12, 43\}$
$\{13, 40\}$	$\{14, 39\}$
$\{15, 22\}$	$\{16, 21\}$
$\{23, 48\}$	$\{24, 47\}$
$\{25, 46\}$	$\{26, 45\}$
$\{29, 34\}$	$\{30, 33\}$
$\{31, 36\}$	$\{32, 35\}$

Table D.5: Symmetry-equivalent representatives for $\boldsymbol{K}_4$-vectors.

$\boldsymbol{K}_5$, $M(\boldsymbol{K}) = 24, g_0(\boldsymbol{K}) = 2$	
$\{1, 16\}$	$\{2, 15\}$
$\{3, 10\}$	$\{4, 9\}$
$\{5, 26\}$	$\{6, 25\}$
$\{7, 32\}$	$\{8, 31\}$
$\{11, 30\}$	$\{12, 29\}$
$\{13, 24\}$	$\{14, 23\}$
$\{17, 20\}$	$\{18, 19\}$
$\{21, 28\}$	$\{22, 27\}$
$\{33, 44\}$	$\{34, 43\}$
$\{35, 38\}$	$\{36, 37\}$
$\{39, 48\}$	$\{40, 47\}$
$\{41, 46\}$	$\{42, 45\}$

Table D.6: Symmetry-equivalent representatives for $\boldsymbol{K}_5$-vectors.

$\boldsymbol{K}_6$, $M(\boldsymbol{K}) = 24, g_0(\boldsymbol{K}) = 2$	
$\{1, 30\}$	$\{2, 29\}$
$\{3, 12\}$	$\{4, 11\}$
$\{5, 40\}$	$\{6, 39\}$
$\{7, 48\}$	$\{8, 47\}$
$\{9, 24\}$	$\{10, 23\}$
$\{13, 16\}$	$\{14, 15\}$
$\{17, 46\}$	$\{18, 45\}$
$\{19, 38\}$	$\{20, 37\}$
$\{21, 42\}$	$\{22, 41\}$
$\{25, 44\}$	$\{26, 43\}$
$\{27, 36\}$	$\{28, 35\}$
$\{31, 34\}$	$\{32, 33\}$

Table D.7: Symmetry-equivalent representatives for $\boldsymbol{K}_6$-vectors.

Appendix E

Component Function h_γ Selection Rules

We present here the calculation of the contributing components to the series for the Fourier components of the two-body density as given by Eq. 2.62, reproduced here for clarity

$$u_{\rm rot}(\boldsymbol{r}';\boldsymbol{K}) = \sum_{\gamma=-\infty}^{\infty} h_\gamma^{(\rm rot)}(r,\Theta;\boldsymbol{K})e^{i\gamma\phi}. \tag{2.62}$$

A summary table can be found in the main body of this work (Section 2.2.4, Table 2.2). The pertinent symmetry rotations for each type of $\boldsymbol{K}$-vector are those of the Laue class of the $\boldsymbol{K}$-vector. The Laue classes for the unprimed frames are formed by combining the rotations that leave $\boldsymbol{K}$ invariant with the rotations produced by multiplying this latter set with the inversion I. The Laue classes can be constructed from Tables D.2 to D.7.

Rotation	$\boldsymbol{n}$	$\boldsymbol{n}'$
E, I	$(0,0,0)$	$(0,0,0)$
σ_{d1}, C'_{2a}	$(1,1,0)$	$(1,0,0)$
σ_{d4}, C'_{2d}	$(0,-1,-1)$	$(-\frac{1}{\sqrt{3}},-1,0)$
σ_{d5}, C'_{2e}	$(1,0,-1)$	$(\frac{1}{\sqrt{3}},-1,0)$
$C^{\pm}_{34}, S^{\pm}_{64}$	$(-1,1,-1)$	$(0,0,-1)$

Table E.1: Laue class for $\boldsymbol{K}_2$-vectors with directions in unprimed and primed frames.

E.1 $\boldsymbol{K}_2$-Vector Class

The rotations that must be considered for vectors of type $\boldsymbol{K}_2$ are listed in Table E.1 with their directions in both the unprimed and primed reference frames. The labelling of the rotations in the equations that follow is that of the unprimed frame, however they are applied in the primed frame as indicated by $\boldsymbol{n}'$ in Table E.1. The effects upon the angles ϕ and θ from applying the rotations to the component functions h_γ are listed in Table E.2. Summing all the rotated component functions we find

$$\mathcal{P}^{(\mathrm{rot})}\left[h_\gamma^{(\mathrm{rot})}(r,\theta;\boldsymbol{K}_2)e^{i\gamma\phi}\right] = \frac{2}{12}\left(e^{i\gamma\phi}+(-1)^\gamma e^{-i\gamma\phi}\right)\left(1+2\cos\left(\gamma\frac{2\pi}{3}\right)\right) \times h_\gamma^{(\mathrm{rot})}(r,\theta;\boldsymbol{K}_2). \tag{E.1}$$

Rot	$\boldsymbol{n}'$	ϕ	θ	h_γ
E	$(0,0,0)$	ϕ	θ	$h_\gamma(r,\theta;\boldsymbol{K}_2)e^{i\gamma\phi}$
I	$(0,0,0)$	$\phi+\pi$	$\pi-\theta$	$h_\gamma(r,\theta;\boldsymbol{K}_2)e^{i\gamma\phi}$
σ_{d1}	$(1,0,0)$	$\pi-\phi$	θ	$(-1)^\gamma h_\gamma(r,\theta;\boldsymbol{K}_2)e^{-i\gamma\phi}$
C'_{2a}	$(1,0,0)$	$-\phi$	$\pi-\theta$	$(-1)^\gamma h_\gamma(r,\theta;\boldsymbol{K}_2)e^{-i\gamma\phi}$
σ_{d4}	$(-\frac{1}{\sqrt{3}},-1,0)$	$-(\phi+\frac{\pi}{3})$	θ	$e^{i\gamma\frac{2\pi}{3}}(-1)^\gamma h_\gamma(r,\theta;\boldsymbol{K}_2)e^{-i\gamma\phi}$
σ_{d5}	$(\frac{1}{\sqrt{3}},-1,0)$	$\frac{\pi}{3}-\phi$	θ	$e^{-i\gamma\frac{2\pi}{3}}(-1)^\gamma h_\gamma(r,\theta;\boldsymbol{K}_2)e^{-i\gamma\phi}$
C'_{2d}	$(-\frac{1}{\sqrt{3}},-1,0)$	$\frac{2\pi}{3}-\phi$	$\pi-\theta$	$e^{i\gamma\frac{2\pi}{3}}(-1)^\gamma h_\gamma(r,\theta;\boldsymbol{K}_2)e^{-i\gamma\phi}$
C'_{2e}	$(\frac{1}{\sqrt{3}},-1,0)$	$\frac{4\pi}{3}-\phi$	$\pi-\theta$	$e^{-i\gamma\frac{2\pi}{3}}(-1)^\gamma h_\gamma(r,\theta;\boldsymbol{K}_2)e^{-i\gamma\phi}$
C_{34}^-	$(0,0,-1)$	$\phi+\frac{2\pi}{3}$	θ	$e^{i\gamma\frac{2\pi}{3}}h_\gamma(r,\theta;\boldsymbol{K}_2)e^{i\gamma\phi}$
C_{34}^+	$(0,0,-1)$	$\phi-\frac{2\pi}{3}$	θ	$e^{-i\gamma\frac{2\pi}{3}}h_\gamma(r,\theta;\boldsymbol{K}_2)e^{i\gamma\phi}$
S_{64}^-	$(0,0,-1)$	$\phi+\frac{\pi}{3}$	$\pi-\theta$	$e^{-i\gamma\frac{2\pi}{3}}h_\gamma(r,\theta;\boldsymbol{K}_2)e^{i\gamma\phi}$
S_{64}^+	$(0,0,-1)$	$\phi+\frac{5\pi}{3}$	$\pi-\theta$	$e^{i\gamma\frac{2\pi}{3}}h_\gamma(r,\theta;\boldsymbol{K}_2)e^{i\gamma\phi}$

Table E.2: Effect of $\boldsymbol{K}_2$-rotations on component functions.

We find that there are three sets of values for γ;

$$\gamma = 3\gamma' \qquad \gamma' \in \mathbb{Z}_0, \tag{E.2a}$$

$$\gamma = 3\gamma' + 1 \qquad \gamma' \in \mathbb{Z}_0, \tag{E.2b}$$

$$\gamma = 3\gamma' + 2 \qquad \gamma' \in \mathbb{Z}_0. \tag{E.2c}$$

Taking each in turn we find:

- $\gamma = 3\gamma' \rightarrow \cos\left(\gamma\frac{2\pi}{3}\right) = 1$, leading to the following contributions to the Fourier transform, $u_{\text{rot}}(\boldsymbol{r}; \boldsymbol{K}_2)$, (neglecting normalisation factors).

$$h_{6n}^{(\text{rot})}(r, \theta; \boldsymbol{K}_2) \cos(6n\phi) \tag{E.3a}$$

$$ih_{6n+3}^{(\text{rot})}(r, \theta; \boldsymbol{K}_2) \sin([6n+3]\phi) \tag{E.3b}$$

- $\gamma = 3\gamma' + 1 \rightarrow \cos\left(\gamma\frac{2\pi}{3}\right) = -\frac{1}{2}$ and hence $1 + 2\cos\left(\gamma\frac{2\pi}{3}\right) = 0$, resulting in no contribution to the Fourier transform $u_{\text{rot}}(\boldsymbol{r}; \boldsymbol{K}_2)$.

- $\gamma = 3\gamma' + 2 \rightarrow \cos\left(\gamma\frac{2\pi}{3}\right) = -\frac{1}{2}$ which, similarly to the previous case, leads to no contribution to the Fourier transform $u_{\text{rot}}(\boldsymbol{r}; \boldsymbol{K}_2)$.

Gathering all contributions together the series representation of the Fourier transform of the two body density can be expressed as

$$u_{\rm rot}(\boldsymbol{r};\boldsymbol{K}_2) = \sum_{\gamma=-\infty}^{\infty} h_\gamma^{(\rm rot)}(r,\theta;\boldsymbol{K}_2)e^{i\gamma\phi} \tag{E.4}$$

$$\begin{aligned}
=&h_0^{(\rm rot)}(r,\theta;\boldsymbol{K}_2) \\
&+\sum_{n=1}^{\infty}\left\{h_{6n}^{(\rm rot)}(r,\theta;\boldsymbol{K}_2)+h_{6n}^{\star(\rm rot)}(r,\theta;\boldsymbol{K}_2)\right\}\cos(6n\phi) \\
&+i\sum_{n=0}^{\infty}h_{6n+3}^{(\rm rot)}(r,\theta;\boldsymbol{K}_2)\sin([6n+3]\phi) \\
&+i\sum_{n=1}^{\infty}h_{-6n+3}^{(\rm rot)}(r,\theta;\boldsymbol{K}_2)\sin([-6n+3]\phi).
\end{aligned} \tag{E.5}$$

Rewriting the last term as $i\sum_{n=0}^{\infty}h_{-6n-3}^{(\rm rot)}(r,\theta;\boldsymbol{K}_2)\sin(-[6n+3]\phi)$ yields

$$\begin{aligned}
u_{\rm rot}(\boldsymbol{r};\boldsymbol{K}_2) =&h_0^{(\rm rot)}(r,\theta;\boldsymbol{K}_2) \\
&+\sum_{n=1}^{\infty}\left\{h_{6n}^{(\rm rot)}(r,\theta;\boldsymbol{K}_2)+h_{6n}^{\star(\rm rot)}(r,\theta;\boldsymbol{K}_2)\right\}\cos(6n\phi) \\
&+i\sum_{n=0}^{\infty}\left\{h_{6n+3}^{(\rm rot)}(r,\theta;\boldsymbol{K}_2)-h_{6n+3}^{\star(\rm rot)}(r,\theta;\boldsymbol{K}_2)\right\}\sin([6n+3]\phi)
\end{aligned} \tag{E.6}$$

$$\begin{aligned}
=&\Re\left\{h_0^{(\rm rot)}(r,\theta,\boldsymbol{K}_2)\right\} \\
&+2\sum_{n=1}^{\infty}\Re\left\{h_{6n}^{(\rm rot)}(r,\theta;\boldsymbol{K}_2)\right\}\cos(6n\phi) \\
&-2\sum_{n=0}^{\infty}\Im\left\{h_{6n+3}^{(\rm rot)}(r,\theta;\boldsymbol{K}_2)\right\}\sin([6n+3]\phi).
\end{aligned} \tag{E.7}$$

Equation E.7 states that for $\gamma \neq 3n, n \in \mathbb{Z}_0$, there should be no contribution to the component functions h_γ and that for $\gamma = 6n, n \in \mathbb{Z}_0$, and $\gamma = 6n+3, n \in \mathbb{Z}_0$, there should be no imaginary or real contributions, respectively. In obtaining the final result we have made use of the reality of $u_{\rm rot}(\boldsymbol{r};\boldsymbol{K}_2)$ to extract the relevant

real and imaginary parts of the component functions.

E.2 K_3-Vector Class

We present in Table E.3 the effect of each rotation on the angles ϕ and θ. In the same manner as for vectors of type $\boldsymbol{K}_2$ we sum the effects of all rotations on the component functions h_γ,

$$\begin{aligned}\mathcal{P}^{(\mathrm{rot})}\left[h_\gamma^{(\mathrm{rot})}(r,\theta;\boldsymbol{K}_3)e^{i\gamma\phi}\right] =& \frac{1}{16}\Big\{2\left[1+(-1)^\gamma\right]h_\gamma^{(\mathrm{rot})}(r,\theta;\boldsymbol{K}_3)\left[e^{i\gamma\phi}+e^{-i\gamma\phi}\right] \\ & 2\left[i^\gamma+(-i)^\gamma\right]h_\gamma^{(\mathrm{rot})}(r,\theta;\boldsymbol{K}_3)\left[e^{i\gamma\phi}+e^{-i\gamma\phi}\right]\Big\} \quad \text{(E.8)} \\ =& \frac{1}{4}\left[1+i^\gamma\right]\left[1+(-1)^\gamma\right]h_\gamma^{(\mathrm{rot})}(r,\theta;\boldsymbol{K}_3)\cos(\gamma\phi) \quad \text{(E.9)}\end{aligned}$$

The expression E.9 has four possible results:

- $\gamma = 4\gamma' + 1 \rightarrow \left[1+i^\gamma\right]\left[1+(-1)^\gamma\right] = 0,$
- $\gamma = 4\gamma' + 2 \rightarrow \left[1+i^\gamma\right]\left[1+(-1)^\gamma\right] = 0,$
- $\gamma = 4\gamma' + 3 \rightarrow \left[1+i^\gamma\right]\left[1+(-1)^\gamma\right] = 0,$
- $\gamma = 4\gamma' \rightarrow \left[1+i^\gamma\right]\left[1+(-1)^\gamma\right] = 4,$

Rot	$\boldsymbol{n}'$	ϕ	θ	h_γ
E	$(0,0,0)$	ϕ	θ	$h_\gamma(r,\theta;\boldsymbol{K}_3)e^{i\gamma\phi}$
I	$(0,0,0)$	$\phi+\pi$	$\pi-\theta$	$h_\gamma(r,\theta;\boldsymbol{K}_3)e^{i\gamma\phi}$
σ_y	$(1,0,0)$	$\pi-\phi$	θ	$(-1)^\gamma h_\gamma(r,\theta;\boldsymbol{K}_3)e^{-i\gamma\phi}$
C_{2y}	$(1,0,0)$	$-\phi$	$\pi-\theta$	$(-1)^\gamma h_\gamma(r,\theta;\boldsymbol{K}_3)e^{-i\gamma\phi}$
C_{2x}	$(0,0,1)$	$\pi+\phi$	θ	$(-1)^\gamma h_\gamma(r,\theta;\boldsymbol{K}_3)e^{i\gamma\phi}$
σ_x	$(0,0,1)$	ϕ	$\pi-\theta$	$(-1)^\gamma h_\gamma(r,\theta;\boldsymbol{K}_3)e^{i\gamma\phi}$
C_{4x}^-	$(0,0,1)$	$\frac{\pi}{2}+\phi$	θ	$i^\gamma h_\gamma(r,\theta;\boldsymbol{K}_3)e^{i\gamma\phi}$
S_{4x}^-	$(0,0,1)$	$\frac{\pi}{2}+\phi$	$\pi-\theta$	$(-i)^\gamma h_\gamma(r,\theta;\boldsymbol{K}_3)e^{i\gamma\phi}$
σ_z	$(0,1,0)$	$-\phi$	θ	$h_\gamma(r,\theta;\boldsymbol{K}_3)e^{-i\gamma\phi}$
C_{2z}	$(0,1,0)$	$\pi-\phi$	$\pi-\theta$	$h_\gamma(r,\theta;\boldsymbol{K}_3)e^{-i\gamma\phi}$
σ_{d6}	$(-1,1,0)$	$\frac{\pi}{2}-\phi$	θ	$i^\gamma h_\gamma(r,\theta;\boldsymbol{K}_3)e^{-i\gamma\phi}$
C_{2f}''	$(-1,1,0)$	$-\frac{\pi}{2}-\phi$	$\pi-\theta$	$i^\gamma h_\gamma(r,\theta;\boldsymbol{K}_3)e^{-i\gamma\phi}$
σ_{d4}	$(1,1,0)$	$-\frac{\pi}{2}-\phi$	θ	$(-i)^\gamma h_\gamma(r,\theta;\boldsymbol{K}_3)e^{-i\gamma\phi}$
C_{2d}''	$(1,1,0)$	$\frac{\pi}{2}-\phi$	$\pi-\theta$	$(-i)^\gamma h_\gamma(r,\theta;\boldsymbol{K}_3)e^{-i\gamma\phi}$
C_{4x}^+	$(0,0,1)$	$\phi-\frac{\pi}{2}$	θ	$(-i)^\gamma h_\gamma(r,\theta;\boldsymbol{K}_3)e^{i\gamma\phi}$
S_{4x}^+	$(0,0,1)$	$\phi-\frac{\pi}{2}$	$\pi-\theta$	$i^\gamma h_\gamma(r,\theta;\boldsymbol{K}_3)e^{i\gamma\phi}$

Table E.3: Effect of $\boldsymbol{K}_3$-rotations on component functions.

Rot	$\boldsymbol{n}'$	ϕ	θ	h_γ
E	$(0,0,0)$	ϕ	θ	$h_\gamma(r,\theta;\boldsymbol{K}_4)e^{i\gamma\phi}$
I	$(0,0,0)$	$\phi+\pi$	$\pi-\theta$	$h_\gamma(r,\theta;\boldsymbol{K}_4)e^{i\gamma\phi}$
σ_{d1}	$(1,0,0)$	$\pi-\phi$	θ	$(-1)^\gamma h_\gamma(r,\theta;\boldsymbol{K}_4)e^{-i\gamma\phi}$
C'_{2a}	$(1,0,0)$	$-\phi$	$\pi-\theta$	$(-1)^\gamma h_\gamma(r,\theta;\boldsymbol{K}_4)e^{-i\gamma\phi}$

Table E.4: Effect of $\boldsymbol{K}_4$-rotations on component functions.

where for all cases we have $\gamma' \in \mathbb{N}_0$. The expression for the Fourier transform can now be written as

$$\begin{aligned} u_{\text{rot}}(\boldsymbol{r};\boldsymbol{K}_3) =& h_0^{(\text{rot})}(r,\theta;\boldsymbol{K}_3) \\ &+ \sum_{n=1}^{\infty} h_{4n}^{(\text{rot})}(r,\theta;\boldsymbol{K}_3)\cos(4n\phi) \\ &+ \sum_{n=1}^{\infty} h_{4n}^{\star(\text{rot})}(r,\theta;\boldsymbol{K}_3)\cos(4n\phi) \\ =& \Re\left\{h_0^{(\text{rot})}(r,\theta;\boldsymbol{K}_3)\right\} + 2\sum_{n=1}^{\infty}\Re\left\{h_{4n}^{(\text{rot})}(r,\theta;\boldsymbol{K}_3)\cos(4n\phi)\right\}. \end{aligned} \tag{E.10}$$

E.3 K_4-Vector Class

Table E.4 lists the effects on the angles ϕ and θ. Following the process previously employed we find,

$$\mathcal{P}^{(\text{rot})}\left[h_\gamma^{(\text{rot})}(r,\theta;\boldsymbol{K}_4)e^{i\gamma\phi}\right] = \frac{1}{2}h_\gamma^{(\text{rot})}(r,\theta;\boldsymbol{K}_4)\left(e^{i\gamma\phi}+(-1)^\gamma e^{-i\gamma\phi}\right). \tag{E.11}$$

The Fourier transform is then written as

$$
\begin{aligned}
u_{\mathrm{rot}}(\boldsymbol{r};\boldsymbol{K}_4) =& h_0^{(\mathrm{rot})}(r,\theta;\boldsymbol{K}_4) \\
&+ \sum_{n=1}^{\infty}\left\{h_{2n}^{(\mathrm{rot})}(r,\theta;\boldsymbol{K}_4) + h_{2n}^{\star(\mathrm{rot})}(r,\theta;\boldsymbol{K}_4)\right\}\cos(2n\phi) \\
&+ i\sum_{n=0}^{\infty} h_{2n+1}^{(\mathrm{rot})}(r,\theta;\boldsymbol{K}_4)\sin([2n+1]\phi) \\
&+ i\sum_{n=0}^{\infty} h_{-2n-1}^{(\mathrm{rot})}(r,\theta;\boldsymbol{K}_4)\sin(-[2n+1]\phi) \qquad \text{(E.12)} \\
=& h_0^{(\mathrm{rot})}(r,\theta;\boldsymbol{K}_4) \\
&+ \sum_{n=1}^{\infty}\left\{h_{2n}^{(\mathrm{rot})}(r,\theta;\boldsymbol{K}_4) + h_{2n}^{\star(\mathrm{rot})}(r,\theta;\boldsymbol{K}_4)\right\}\cos(2n\phi) \\
&+ i\sum_{n=0}^{\infty} h_{2n+1}^{(\mathrm{rot})}(r,\theta;\boldsymbol{K}_4)\sin([2n+1]\phi) \\
&+ i\sum_{n=0}^{\infty} h_{2n+1}^{\star(\mathrm{rot})}(r,\theta;\boldsymbol{K}_4)\sin([2n+1]\phi) \qquad \text{(E.13)} \\
=& \Re\left\{h_0^{(\mathrm{rot})}(r,\theta;\boldsymbol{K}_4)\right\} \\
&+ 2\sum_{n=1}^{\infty}\Re\left\{h_{2n}^{(\mathrm{rot})}(r,\theta;\boldsymbol{K}_4)\right\}\cos(2n\phi) \\
&- 2\sum_{n=0}^{\infty}\Im\left\{h_{2n+1}^{(\mathrm{rot})}(r,\theta;\boldsymbol{K}_4)\right\}\sin([2n+1]\phi) \qquad \text{(E.14)}
\end{aligned}
$$

E.4 $\boldsymbol{K}_5$-Vector Class

The relevant rotations and their effects on the angles ϕ and θ are presented in Table E.5. Summing the rotations we find

$$
\mathcal{P}^{(\mathrm{rot})}\left[h_\gamma^{(\mathrm{rot})}(r,\theta;\boldsymbol{K}_5)e^{i\gamma\phi}\right] = h_\gamma^{(\mathrm{rot})}(r,\theta;\boldsymbol{K}_5)\cos(\gamma\phi), \qquad \text{(E.15)}
$$

Rot	$\boldsymbol{n}'$	ϕ	θ	h_γ
E	$(0,0,0)$	ϕ	θ	$h_\gamma(r,\theta;\boldsymbol{K}_5)e^{i\gamma\phi}$
I	$(0,0,0)$	$\phi+\pi$	$\pi-\theta$	$h_\gamma(r,\theta;\boldsymbol{K}_5)e^{i\gamma\phi}$
σ_z	$(0,1,0)$	$-\phi$	θ	$h_\gamma(r,\theta;\boldsymbol{K}_5)e^{-i\gamma\phi}$
C_{2z}	$(0,1,0)$	$\pi-\phi$	$\pi-\theta$	$h_\gamma(r,\theta;\boldsymbol{K}_5)e^{-i\gamma\phi}$

Table E.5: Effect of $\boldsymbol{K}_5$-rotations on component functions.

and the Fourier transform becomes

$$u_{\text{rot}}(\boldsymbol{r};\boldsymbol{K}_5) = \Re\left\{h_0^{(\text{rot})}(r,\theta;\boldsymbol{K}_5)\right\} + 2\sum_{n=1}^{\infty}\Re\left\{h_n^{(\text{rot})}(r,\theta;\boldsymbol{K}_5)\right\}\cos(n\phi) \qquad \text{(E.16)}$$

Appendix F

Other Potentials

We present here the relevant details to calculate the Tang-Toennies and the Lennard-Jones potentials, their first and second derivatives and the tail corrections as defined in Eq. 2.94.

F.1 Tang-Toennies Potential

The Tang-Toennies potential [32] is formed from the sum of two potentials, the first being a repulsive short-range potential and the second a long-range attractive potential,

$$V(r) = V_{\text{rep}}(r) + V_{\text{att}}(r) = A\exp(-br) - \sum_{n=3}^{N} f_{2n}(br)\frac{C_{2n}}{r^{2n}} \tag{F.1}$$

with

$$f_{2n}(x) = 1 - \exp(-x)\sum_{k=0}^{2n}\frac{x^k}{k!}. \tag{F.2}$$

Parameter	Value (reduced units)
A	26285083
b	3.524339
C_6	898647.3
C_8	8129980
C_{10}	84551104

Table F.1: Krypton parameters for Tang-Toennies Potential.

The sum in Eq. F.1 should include enough terms such that convergence is reached. Tang and Toennies [32] state that $N = 5$ is sufficient even though convergence is not reached as corrections from higher-order terms are compensated by the choice of parameters A and b. The parameters for Krypton are given in Table F.1. The first and second derivatives as required for computation of the kinetic energy are given below,

$$\frac{dV(r)}{dr} = -Ab\exp(-br) + \sum_{n=3}^{5} \frac{C_{2n}}{r^{2n}} \left(\left(\frac{2n}{r} + b \right) f_{2n}(br) - b f_{2n-1}(br) \right), \quad \text{(F.3)}$$

$$\begin{aligned} \frac{d^2V(r)}{dr^2} =& Ab^2\exp(-br) + \sum_{n=3}^{5} \frac{C_{2n}}{r^{2n}} \left(-\frac{(2n)(2n+1)}{r^2} f_{2n}(br) \right. \\ & - \frac{4nb}{r}\big(f_{2n}(br) - f_{2n-1}(br)\big) \\ & \left. + b^2\big(f_{2n}(br) - 2f_{2n-1}(br) + f_{2n-2}(br)\big) \right). \end{aligned} \quad \text{(F.4)}$$

Parameter	Value
ϵ	119.8 K
σ	3.405 Å

Table F.2: Argon parameters for Lennard-Jones Potential.

The tail correction is calculated using Eq. 2.94 and turns out to be

$$\frac{E_{\text{tail}}}{N} = 2\pi\rho_0 \int_{r_{\text{limit}}}^{\infty} r^2 v(r) dr \tag{2.94}$$

$$\begin{aligned} =& 2\pi\rho_0 \left[A\exp(-br) \left(\frac{b^2 r_{\text{limit}}^2 + 2br_{\text{limit}} + 2}{b^3} \right) \right. \\ &+ (f_3(br_{\text{limit}}) - 1) \left(\frac{2C_6 b^3}{6!} + \frac{3! \cdot C_8 b^5}{8! \cdot 5} + \frac{3! \cdot C_{10} b^7}{10! \cdot 7} \right) \\ &- \frac{C_6}{3r_{\text{limit}}^3} (f_6(br_{\text{limit}})) - \frac{C_8}{5r_{\text{limit}}^5} (f_8(br_{\text{limit}})) \\ &\left. - \frac{C_{10}}{7r_{\text{limit}}^7} (f_{10}(br_{\text{limit}})) \right]. \end{aligned} \tag{F.5}$$

F.2 Lennard-Jones Potential

The Lennard Jones 12-6 potential is one of the most common potentials used due to its simple form,

$$V(r) = 4\epsilon \left[\left(\frac{\sigma}{r} \right)^{12} - \left(\frac{\sigma}{r} \right)^{6} \right]. \tag{F.6}$$

We present in Table F.2 the values of ϵ and σ used for simulating Argon. The first derivative is given by

$$\frac{dV(r)}{dr} = 4\epsilon \left[\left(-\frac{12\sigma^{12}}{r^{13}} \right) + \left(\frac{6\sigma^6}{r^7} \right) \right], \tag{F.7}$$

and the second derivative by

$$\frac{d^2V(r)}{dr^2} = 4\epsilon\left[\left(\frac{156\sigma^{12}}{r^{14}}\right) - \left(\frac{42\sigma^6}{r^8}\right)\right], \tag{F.8}$$

with the tail correction being given by

$$E_{\text{tail}} = \frac{8\pi\rho_0}{3r_{\text{limit}}^3}\epsilon\sigma^6\left(\frac{1}{3}\left(\frac{\sigma}{r_{\text{limit}}}\right)^6 - 1\right). \tag{F.9}$$

Bibliography

[1] M. P. Allen and D. J. Tildesley. *Computer Simulation of Liquids.* Oxford University Press, 1987.

[2] R. A. Aziz, A. R. Janzen, and M. R. Moldover. Ab Initio Calculations for Helium: A Standard for Transport Property Measurements. *Phys. Rev. Lett.*, 74(9):1586, February 1995.

[3] R. A. Aziz, V. P. S. Nain, J. S. Carley, W. L. Taylor, and G. T. McConville. An Accurate Intermolecular Potential for Helium. *J. Chem. Phys.*, 70(9):4330, May 1979.

[4] R. A. Aziz and M. J. Slaman. An Analysis of the ITS-90 Relations for the Non-Ideality of 3He and 4He: Recommended Relations Based on a New Interatomic Potential for Helium. *Metrologia*, 27(4):211, 1990.

[5] R. A. Aziz, M.J. Slaman, A. Koide, A.R. Allnatt, and W. Meath. Exchange-Coulomb Potential Energy Curves for He-He, and Related Physical Properties. *Mol. Phys.*, 77(2):321, October 1992.

[6] M. Boninsegni, C. Pierleoni, and D. M. Ceperley. Isotopic Shift of Helium Melting Pressure: Path Integral Monte Carlo Study. *Phys. Rev. Lett.*, 72(12):1854, March 1994.

[7] G. Burns and A. M. Glazer. *Space Groups for Solid State Scientists.* Academic Press, 1978.

[8] D. M. Ceperley. Path Integrals in the Theory of Condensed Helium. *Rev. Mod. Phys.*, 67(2):279, April 1995.

[9] S. Y. Chang and M. Boninsegni. *Ab Initio* Potentials and the Equation of State of Condensed Helium at High Pressure. *J. Chem. Phys.*, 115(6):2629, August 2001.

[10] J. F. Cornwell. *Group Theory in Physics*, volume 1. Academic Press, 1984.

[11] A. Cuccoli, A. Macchi, V. Tongnetti, and R. Vaia. Monte Carlo Computations of the Quantum Kinetic Energy of Rare-Gas Solids. *Phys. Rev. B*, 47(22):923, June 1993.

[12] E. W. Draeger and D. M. Ceperley. Debye-Waller Factor in Solid ^{3}He and ^{4}He. *Phys. Rev. B*, 61(18):12094, May 2000.

[13] B. Errandonea, D. Schwager and Boehler R. Crystal Structure Transformations of Rare-Gas Solids Under Pressure. *High Pressure Res.*, 22(2):375, 2002.

[14] D. Errandonea, B. Schwager, R. Boehler, and M. Ross. Phase Behavior of Krypton and Xenon to 50GPa. *Phys. Rev. B*, 65(21):4110, June 2002.

[15] R. P. Feynman and A. R. Hibbs. *Quantum Mechanics and Path Integrals.* McGraw-Hill, 1965.

[16] K. A. Gernoth. Explorations of the Microstructure of Crystalline Quantum Many-Body systems. *Ann. Phys.*, 285(1):61, October 2000.

[17] K. A. Gernoth. Analytical and Numerical (Monte Carlo) Studies of Point and Space Group Symmetry-Breaking in the Liquid-Solid Phase Transition. *Ann. Phys.*, 291(2):202, August 2001.

[18] K. A. Gernoth. Crystallographic Point and Space Group Symmetries in the One- and Two-Body Density of Crystals and Generalized Patterson Functions: Fourier Path Integral Monte Carlo Case Studies of Novel High-Temperature/High-Pressure ^{4}He Quantum Crystals. *Z. Kristallogr.*, 218:651, October 2003.

[19] C. P. Herrero. Isotopic Effect in the Lattice Parameter of Rare-Gas Solids. *J. Phys. Condens. Matter*, 15:475, January 2003.

[20] C. P. Herrero. Solid Helium at High Pressure: A Path-Integral Monte Carlo Simulation. *J. Phys. Condens. Matter*, 18(13):3469, March 2006.

[21] C. P. Herrero and R. Ramírez. Rare-Gas Solids Under Pressure: A Path Integral Monte Carlo Simulation. *Phys. Rev. B*, 71(17):4111, May 2005.

[22] K. W. Herwig, P. E. Sokol, T. R. Sosnick, W. M. Snow, and R. C. Blasdell. Density Dependence of the Momentum Distribution in Normal Liquid ^{4}He. *Phys. Rev. B*, 41(1):103, January 1990.

[23] M. L. Klien and J. A. Venables. *Rare Gas Solids*, volume 1. Academic Press, 1976.

[24] D. E. Knuth. *The Art of Computer Programming*, volume 2. Addison-Wesley, 1998.

[25] L. Koči, R. Belonoshko A. B. Ahuja, and B. Johansson. Study of the High-Pressure Helium Phase Diagram Using Molecular Dynamics. *J. Phys. Condens. Matter*, 19(1):016206, 2007.

[26] A. Malijevsky and A. Malijevsky. Monte Carlo Simulations of Thermodynamic Properties of Argon, Krypton, and Xenon in Liquid and Gas State Using New *Ab Initio* Pair Potentials. *Molecular Physics*, 101(22):3335, November 2003.

[27] H. K. Mao, R. J. Hemley, Y. Wu, A. P. Jephcoat, L. W. Finger, C. S. Zha, and W. A. Bassett. High-Pressure Phase Diagram and Equation of State of Solid Helium from Single-Crystal X-Ray Diffraction to 23.3 GPa. *Phys. Rev. Lett.*, 60(25):2649, June 1988.

[28] N. Metropolis, A. W. Rosenbluth, M. N. Rosenbluth, A. H. Teller, and E. Teller. Equation of State Calculations by Fast Computing Machines. *J. Chem. Phys.*, 21(6):1087, June 1953.

[29] GCC Online Document. http://gcc.gnu.org/onlinedocs/gfortran/random_005fnumber.html.

[30] E. L. Pollock and D. M. Ceperley. Simulation of Quantum Many-Body Systems by Path-Integral Methods. *Phys. Rev. B*, 30(5):2555, September 1984.

[31] K. Singer and W. Smith. Path Integral Simulations of Condensed Phase Lennard-Jones Systems. *Mol. Phys.*, 64(6):1215, August 1988.

[32] K. T. Tang and J. P. Toennies. The van der Waals Potentials between all the Rare Ggas Atoms from He to Rn. *J. Chem. Phys.*, 118(11):4976, March 2003.

[33] D. N. Timms, A. C. Evans, M. Boninsegni, D. M. Ceperley, and J. Mayers. Direct Measurements and Path Integral Monte Carlo Calculations of Kinetic Energies of Solid Neon. *J. Phys. Condens. Matter*, 8:6665, May 1996.

[34] S. A. Vitiello. Relative Stability of HCP and FCC Crystalline Structures of ^{4}He. *Phys. Rev. B*, 65(21):214516, June 2002.

[35] S. A. Vitiello, K. J. Runge, G. V. Chester, and M. H. Kalos. Shadow Wave-Function Variational Calculations of Crystaline and Liquid Phases of ^{4}He. *Phys. Rev. B*, 42(1):228, July 1990.

[36] Q. Wang, C. Li, X. Niu, R. Shen, K. Lu, S. Wei, Z. Wu, T. Liu, Y. Xie, and T. Hu. Structure of Liquid Krypton Under Atmospheric Pressure: An EXAFS and Reverse Monte Carlo Study. *Phys. Rev. B*, 72(9):092202, 2005.